# DIRECT LASER WRITING OF OPTICAL WAVEGUIDES IN TRANSPARENT MATERIALS USING A HIGH REPETITION RATE FEMTOSECOND LASER

**NG KOK BIN** 

FACULTY OF SCIENCE UNIVERSITI MALAYA KUALA LUMPUR

## DIRECT LASER WRITING OF OPTICAL WAVEGUIDES IN TRANSPARENT MATERIALS USING A HIGH REPETITION RATE FEMTOSECOND LASER

#### **NG KOK BIN**

## THESIS SUBMITTED IN FULFILMENT OF THE REQUIREMENTS FOR THE DEGREE OF DOCTOR OF PHILOSOPHY

DEPARTMENT OF PHYSICS FACULTY OF SCIENCE UNIVERSITI MALAYA KUALA LUMPUR

# UNIVERSITI MALAYA ORIGINAL LITERARY WORK DECLARATION

Name of Candidate: NG KOK BIN Matric No: 17058617/2 Name of Degree: **DOCTOR OF PHILOSOPHY** Title of Thesis ("this Work"): DIRECT LASER WRITING OF OPTICAL WAVEGUIDES IN TRANSPARENT MATERIALS USING A HIGH REPETITION RATE FEMTOSECOND LASER Field of Study: **EXPERIMENTAL PHYSICS** I do solemnly and sincerely declare that: (1) I am the sole author/writer of this Work; (2) This Work is original; (3) Any use of any work in which copyright exists was done by way of fair dealing and for permitted purposes and any excerpt or extract from, or reference to or reproduction of any copyright work has been disclosed expressly and sufficiently and the title of the Work and its authorship have been acknowledged in this Work; (4) I do not have any actual knowledge nor do I ought reasonably to know that the making of this work constitutes an infringement of any copyright work; (5) I hereby assign all and every rights in the copyright to this Work to the University of Malaya ("UM"), who henceforth shall be owner of the copyright in this Work and that any reproduction or use in any form or by any means whatsoever is prohibited without the written consent of UM having been first had and obtained; (6) I am fully aware that if in the course of making this Work I have infringed any copyright whether intentionally or otherwise, I may be subject to legal action or any other action as may be determined by UM. Candidate's Signature Date: Subscribed and solemnly declared before, Witness's Signature Date:

Name:

Designation:

# DIRECT LASER WRITING OF OPTICAL WAVEGUIDES IN TRANSPARENT MATERIALS USING A HIGH REPETITION RATE FEMTOSECOND LASER

#### **ABSTRACT**

Direct laser writing (DLW) is an advanced nanofabrication technology where high-power laser is tightly focused into a transparent material to induce modifications. Arbitrary structure can be produced by moving the sample across the laser focal spot in the 3-D space. During the fabrication process, several laser writing parameters are manipulated depending on the material properties, desired structure, dimensions, and applications. Among the many types of lasers, high repetition rate femtosecond laser (>100 kHz) has attracted much attention due to its unique interactions with the transparent material. DLW with high repetition rate laser typically gives rise to the heat accumulation effect. The pulse energy is deposited to the material faster than the thermal energy can dissipate between the arrival of successive pulses. This causes thermal energy to build up at the laser focal spot, leading to intense heat accumulation effect. In this work, the interaction between the heat accumulation effect with different transparent materials is investigated. The first study involves the waveguide fabrication in soda lime glass with a 100 kHz femtosecond laser at 515 nm. The waveguide produced has a core index of 4.7 x 10<sup>-3</sup>, among the highest recorded value compared with the waveguide written in borosilicate glass and fused silica glass. However, the fabricated waveguide exhibits high propagation loss of 2.5 dB/cm and coupling loss of 2.8 dB due to the non-uniformity of the core refractive index and the ellipticity mismatch, respectively. Further work is necessary to improve the performance of the waveguide. The second study involves laser ablation of CR-39 using 80 MHz femtosecond laser at 800 nm. The result shows that continuous modification is impossible when the laser is focused inside the material due to the inherent characteristics of thermoset plastics. However, straight trenches were successfully ablated when the laser is focused on the surface of the CR-39. The study highlights that the surface ablation efficiency is influenced by the dynamic interplay between the plasma

shielding effects and beam profile distortion at the laser focal spot. The third study

involves the laser-induced polymerization in SU-8 for optical waveguide fabrication.

Straight channel waveguide was first fabricated in the SU-8 film using an 80 MHz

femtosecond laser operating at 780 nm. The processing window for complete

polymerization is obtained in terms of the laser fluence, which is in the range of 1.8 - 10

kJ/cm<sup>2</sup>. Thermal damage observed during the suspended waveguide writing suggesting

that beam truncation effect is involves during the fabrication of 3D waveguide, where the

variation of the voxel dimension at different focal position changes the local intensity of

the laser. This study demonstrates the potential of SU-8 in the creation of 3D optical

waveguide for future photonics integrated circuit applications. As a conclusion, the

experimental works included in this dissertation provide valuable insights of the

interaction between high repetition rate femtosecond laser with various transparent

materials, which in turns benefit future research not only in the field of direct laser writing,

but also applications in the diverse field of femtosecond laser interactions with materials.

Keywords: Direct laser writing, high repetition rate, optical waveguide, soda lime glass,

CR-39, SU-8

iv

# PENULISAN LASER LANGSUNG PANDUAN GELOMBANG OPTIK DALAM BAHAN TELUS MENGGUNAKAN LASER FEMTOSECOND KADAR PENGULANG TINGGI

#### **ABSTRAK**

Penulisan laser langsung ialah teknologi nanofabrikasi termaju di mana laser berkuasa tinggi difokuskan dengan ketat ke dalam bahan telus untuk mendorong pengubahsuaian. Struktur sewenang-wenang boleh dihasilkan dengan menggerakkan sampel merentasi titik fokus laser dalam ruang 3-D. Semasa proses fabrikasi, beberapa parameter penulisan laser dimanipulasi bergantung pada sifat bahan, struktur yang dikehendaki, dimensi dan aplikasi. Di antara banyak jenis laser, laser femtosaat kadar ulangan yang tinggi (>100 kHz) telah menarik banyak perhatian kerana interaksi uniknya dengan bahan telus. Penulisan laser langsung dengan laser kadar pengulangan yang tinggi biasanya menimbulkan kesan pengumpulan haba. Tenaga nadi didepositkan ke bahan lebih cepat daripada tenaga haba boleh hilang antara kedatangan denyutan berturut-turut. Ini menyebabkan tenaga haba terkumpul di tempat fokus laser, yang membawa kepada kesan pengumpulan haba yang sengit. Dalam kerja ini, interaksi antara kesan pengumpulan haba dengan bahan telus yang berbeza disiasat. Kajian pertama melibatkan fabrikasi pandu gelombang dalam kaca kapur soda dengan laser femtosaat 100 kHz pada 515 nm. Pandu gelombang yang dihasilkan mempunyai indeks teras 4.7 x 10<sup>-3</sup>, antara nilai rekod tertinggi berbanding dengan pandu gelombang yang ditulis dalam kaca borosilikat dan kaca silika bercantum. Walau bagaimanapun, pandu gelombang yang direka mempamerkan kehilangan perambatan yang tinggi sebanyak 2.5 dB/cm dan kehilangan gandingan sebanyak 2.8 dB disebabkan oleh ketidakseragaman indeks biasan teras dan ketidakpadanan eliptik. Kerja lanjut adalah perlu untuk meningkatkan prestasi pandu gelombang. Kajian kedua melibatkan ablasi laser CR-39 menggunakan laser femtosecond 80 MHz pada 800 nm. Hasilnya menunjukkan bahawa pengubahsuaian berterusan adalah mustahil apabila laser difokuskan di dalam bahan kerana ciri-ciri yang wujud pada plastik termoset. Walau bagaimanapun, parit lurus berjaya dihilangkan apabila laser difokuskan

pada permukaan CR-39. Kajian ini menyerlahkan bahawa kecekapan ablasi permukaan

dipengaruhi oleh interaksi dinamik antara kesan perisai plasma dan herotan profil rasuk

di tempat fokus laser. Kajian ketiga melibatkan pempolimeran akibat laser dalam SU-8

untuk fabrikasi pandu gelombang optik. Pandu gelombang saluran lurus pertama kali

dibuat dalam filem SU-8 menggunakan laser femtosaat 80 MHz yang beroperasi pada

780 nm. Tingkap pemprosesan untuk pempolimeran lengkap diperoleh dari segi

kelancaran laser, iaitu dalam julat  $1.8 - 10 \text{ kJ/cm}^2$ . Kerosakan terma yang diperhatikan

semasa penulisan pandu gelombang yang digantung menunjukkan bahawa kesan

pemangkasan rasuk melibatkan semasa fabrikasi pandu gelombang 3D, di mana variasi

dimensi voxel pada kedudukan fokus yang berbeza mengubah keamatan tempatan laser.

Kajian ini menunjukkan potensi SU-8 dalam penciptaan pandu gelombang optik 3D

untuk aplikasi litar bersepadu fotonik masa depan. Sebagai kesimpulan, kerja eksperimen

yang disertakan dalam disertasi ini memberikan pandangan berharga tentang interaksi

antara laser femtosecond kadar pengulangan tinggi dengan pelbagai bahan telus, yang

seterusnya memberi manfaat kepada penyelidikan masa depan bukan sahaja dalam bidang

penulisan laser langsung, tetapi juga aplikasi dalam pelbagai bidang.

Kata kunci: Tulisan laser langsung, kadar pengulangan tinggi, pandu gelombang optik,

kaca kapur soda, CR-39, SU-8

vi

#### ACKNOWLEDGMENT

First and foremost, I would like to express my gratitude to my first supervisor Datuk Professor Ulung Dr. Harith Ahmad to whom I owe a debt of gratitude for his provision of top-tier facilities at the Photonics Research Centre, University of Malaya (PRCUM), which had enabled me to conduct my studies and ultimately complete my PhD program.

In addition, I wish to extend my heartfelt appreciation to my second supervisor Associate Professor Dr. Chong Wu Yi for his innovative insights and constructive feedback. I am particularly grateful for his selfless support and assistance after the fire accident in setting up a new research system for me to complete my PhD. His resilience and dedication in research had inspired me to overcome the challenges and strive for excellence in my work.

Furthermore, I owe a gratitude to my third supervisor Professor Dr. Sithi Vinayakam Muniandy for his guidance in theoretical knowledge for my research. His experience in presentation skills has aided me in crafting my manuscript and thesis and preparing effective presentation slides. Without his generous assistance and expertise in the diverse fields, the completion of this thesis would not have been achievable.

I am grateful to Dr. Lim Chin Seong from Nottingham University in providing support for SEM imaging and EDX analysis. Furthermore, I thank my lab mates Chew Jing Wen, Gan Soon Xin, and Chong Wen Sin for their assistance and discussions. I appreciate the financial support from Malaysia's Ministry of Education through the MyBrainSc scholarship. To my parents and siblings, I extend my deepest appreciation for their unwavering understanding for me to achieve my childhood dream. Lastly, I would like to convey my profound gratitude and love to my girlfriend, Ang Wan Yi. Her presence has been a source of comfort and inspiration whenever I am having a hard time, and I am truly fortunate to have her by my side.

## **Table of Contents**

ABSTRACT	iii
ABSTRAK	v
ACKNOWLEDGEMENTS	vii
TABLE OF CONTENTS	viii
LIST OF FIGURES AND TABLES	xii
LIST OF SYMBOLS AND ABBREVIATIONS	xvii
CHAPTER 1: INTRODUCTION	1
1.1 Overview.	1
1.2 Research Motivations	1
1.3 Research Objectives.	2
1.4 Thesis Outline	3
CHAPTER 2: LITERATURE REVIEW AND BACKGROUND CONCEPTS	5
2.1 Introduction	
2.2 Direct Laser Writing with Ultrafast Femtosecond Laser	7
2.3 Physics of Direct Laser Writing	9
2.3.1 Optical Absorption	10
2.3.2 Multiphoton Absorption and Ionization	11
2.3.3 Avalanche Ionization	13
2.3.4 Laser Induced Optical Breakdown	14
2.4 Two Photons Polymerization	15
2.4.1 Positive Photoresist	16
2.4.2 Negative Photoresist	16
2.4.3 Photopolymerization Induced by Two Photon Absorption	17
2.5 High Repetition Rate Femtosecond Laser for Direct Laser Writing	19
2.6 Direct Laser Writing in Glass	19
2.6.1 Nonlinear Absorption in Glass	21
2.6.2 Coefficient of Thermal Expansion and Direct Laser Writing	23
2.6.3 Soda Lime Glass for Direct Laser Writing	24

2.7 Laser Ablation in Hard Polymer	25
2.7.1 CR-39 for Direct Laser Writing	27
2.8 Microfabrication in SU-8.	28
2.8.1 2D/3D Fabrication with SU-8	29
2.9 Physics of Voxel	31
2.9.1 Focus Lens	33
2.9.2 Continuous Wave Laser and Pulsed Laser	35
2.10 Depth Dependent Laser Interaction	39
2.11 Laser Induced Damage Threshold	41
2.11.1 Wavelength	41
2.11.2 Pulse Duration.	43
2.11.3 Spherical Aberrations.	44
2.12 Conclusion.	45
CHAPTER 3: EXPERIMENTAL METHOD	47
3.1 Introduction.	47
3.2 Ultrafast Femtosecond Laser System	47
3.2.1 Ti:Sapphire Tsunami Femtosecond laser	47
3.2.2 NKT OneFive Origami XP.	48
3.3 Sample Alignment	49
3.4 UV-Vis Spectroscopy.	51
3.5 Soda Lime Glass Waveguide Writing	52
3.5.1 Experimental Setup.	53
3.6 Femtosecond laser ablation on CR-39.	55
3.6.1 Experimental setup.	56
3.7 Waveguide Fabrication.	58
3.7.1 Experimental setup	59
3.8 Sample preparation	61
3.8.1 Soda Lime Glass	62
3.8.2 CR-39	63
3.8.3 SU-8	64
3.9 Waveguide Characterization Techniques	67

3.9.1 Optical Microscope	67
3.9.2 FESEM	69
3.9.3 Surface Profilometer	70
3.9.4 Insertion Loss.	70
3.9.5 Coupling Loss	73
3.9.6 Propagation Loss	76
3.9.7 Mode Field Diameter Measurement	77
3.9.8 Numerical Aperture Approximation	78
3.10 Conclusion.	79
CHAPTER 4: FEMTOSECOND LASER WRITTEN SODA LIME SILICATE GLASS WAVEGUIDE	81
4.1 Introduction.	81
4.2 Waveguide Fabrication	81
4.3 Waveguide Cross-Section Analysis	82
4.4 Waveguide Mode Analysis	87
4.5 Mode Field Diameter and Refractive Index Contrast	89
4.6 Propagation Loss Measurements	91
4.7 Conclusion.	96
CHAPTER 5: SURFACE ABLATION OF CR-39 POLYMER USING HIGH REPETITION RATE FEMTOSECOND	
LASER	98
5.1 Introduction	98
5.2 Determination of the Orders of Nonlinear Absorption	98
5.3 Effect of Focusing Depth to Ablation	100
5.4 Ablation Depth and Ablation Rate	106
5.5 Nitrogen Purging	110
5.6 Conclusion.	113
CHAPTER 6: SINGLE-MODE SU-8 WAVEGUIDE FABRICATION WITH ULTRAFAST DIRECT LASER WRITING	114
6.1 Introduction	114
6.2 Straight Channel Waveguide	114

	6.2.1 Effects of Fluence.	116
	6.2.2 Waveguide Loss.	118
	6.2.3 Double Scan Waveguide Writing	119
6.3	Directional Couplers	121
	6.3.1 S-Bend Simulation.	121
	6.3.2 Directional Coupler Simulation.	124
	6.3.3 Directional Coupler Fabrication.	126
6.4	3D Standing Waveguide	127
	6.4.1 3D Standing Waveguide Design.	128
	6.4.2 Fabrication.	129
	6.4.3 Characterization and Analysis	130
	6.4.4 Optical Characteristics of Suspended Waveguide	136
6.5	Conclusion.	137
СН	IAPTER 7: CONCLUSION AND FUTURE WORKS	139
7.1	Conclusion	139
7.2	Future works	144
RE	FERENCES	146
1 10	ST OF PURI ICATIONS	165

# **List of Figures and Tables**

Figure 2.1	:	Schematic diagram of electron excitation from valence band to conduction band in (a) one-photon absorption and (b) two-photon absorption	10
Figure 2.2	:	Schematic diagram of the photoionization of an electron in an atomic potential for different values of the Keldysh parameter	12
Figure 2.3	:	Schematic diagram of avalanche ionization	13
Table 2.1	:	Nonlinear absorption coefficient of borosilicate glass, fused silica glass, and soda-lime glass	22
Figure 2.4	:	Schematic diagram of the (a) voxel, and (b) overlapping voxels in DLW	32
Figure 2.5	:	Voxel formed by (a) low NA lens, and (b) high NA lens	33
Figure 2.6	:	Schematic diagram showing the enlargement of voxel size with the increase of pulse repetition rate, laser power, and the exposure time	37
Figure 2.7	:	A sketch map of laser focusing across a plane interface from air into the sample.	39
Figure 2.8	:	Schematic diagram showing the focusing depth into the material by (a) low NA, and (b) high NA objective lens. Objective lens with higher NA has larger focusing angle than the low NA objective lens, therefore the maximum focusing depth of high NA objective lens is closer to the sample surface.	40
Figure 3.1		Laser beam path in a Spectra-Physics Tsunami Ti:Sapphire mode-locked laser system	48
Figure 3.2	:	Picture of the NKT OneFive Origami XP high energy femtosecond laser	49
Figure 3.3	:	Beam profile image captured by a CCD camera when the laser focus position is (a) on the sample surface, and (b) away from the sample surface with a 40x (0.65 NA) objective lens	50
Figure 3.4	:	Schematic diagram of the main components in a UV-Vis spectrophotometer	51

Figure 3.5	:	Schematic diagram of the glass writing system. ST: Shutter; L1&L2: Spherical lens 1 and 2	54
Figure 3.6	:	Laser pulse energy calibration. Set energy is the pulse energy coming out from the laser head, whereas the pulse energy on the sample was measured in the position between the objective lens and the glass sample.	55
Figure 3.7	:	Schematic diagram of the surface ablation system. HWP: Half-wave plate; PBS: Polarizing beam splitter; BD: Beam dump; L1&L2: Plano-convex lens 1 and 2; Stage 1: XZ micrometer stage; Stage 2: LTS300 translational stage	57
Figure 3.8	:	Sketch of the experimental setup for SU-8 waveguide writing	59
Figure 3.9	:	a) SU-8 stored in a glass container, (b) spin-coated SU-8 with edge beading effect	65
Figure 3.10	:	(a) Top view of a SU-8 directional coupler captured under the optical microscope with a 10x objective lens. (b) Inset: same directional coupler captured with a 100x objective lens	68
Figure 3.11	:	Cross-sectional image of soda lime glass waveguide captured under 10x objective lens using (a) top illumination, and (b) bottom illumination.	68
Figure 3.12	:	Example of FESEM images for (a) CR-39 surface ablation, and (b) SU-8 waveguide	69
Figure 3.13	:	SU-8 waveguide heigh measurement using Dektak 150	70
Figure 3.14	:	(a) Calibration of the measurement setup and (b) waveguide insertion loss measurement	71
Figure 3.15	:	Optical loss measurement setup	72
Figure 3.16	:	Illustration of the near field MFD measurement technique. Distance d <sub>1</sub> and d <sub>2</sub> were kept constant during the measurement period. The objective lens and IR camera remained static during the measurement, whereas the optical fiber was translating back and forth to obtain the calibration factor and as a light source for the waveguide loss measurements.	78
Figure 4.1	:	Comparison of (a) incomplete polishing, and (b) complete polishing. Scale bar is 30 µm	82
Figure 4.2	:	Cross-sectional view of the laser written waveguide under 10x optical microscope bottom illumination with (a) open, and (b) close aperture. The scale bar is 30 µm	83

Figure 4.3	:	Soda-lime glass waveguide fabricated using (a) 1 µJ, (b) 2 µJ, (c) 3 µJ, and (d) 4 µJ pulse energy, with a scan speed of 0.1 mm/s. Arrow indicates the laser direction. The scale bar is 30 µm.	84
Figure 4.4	:	Width and height of the transparent region plotted against the sample scanning speed for pulse energies from 1 $\mu J$ to 5 $\mu J$ .	85
Figure 4.5	:	Microscope cross-sectional image (left hand side) and near field image (right hand side) of the 515nm femtosecond laser induced waveguide at (a) 1 $\mu$ J, (b) 2 $\mu$ J, and (c) 3 $\mu$ J respectively. Scale bar is 30 $\mu$ m.	88
Figure 4.6	:	Near field profile of the waveguide (a) 1 $\mu$ J, (b) 2 $\mu$ J, and (c) 3 $\mu$ J	89
Figure 4.7	:	Insertion loss measurement of the waveguide fabricated at 2 $\mu J$ and 0.1 mm/s	92
Table 4.1	:	Summary of laser written glass waveguide characteristics	93
Figure 4.8	:	Intensity mode profile for single mode soda-lime glass waveguide fabricated at 2 µJ	95
Figure 5.1	:	UV-VIS spectrum of CR-39. Inset shows the measurement of CR-39 optical bandgap via Tauc plot method	99
Figure 5.2	:	Bulk modification of CR-39 at 100 µm focusing depth: (a) cross-section; (b) top view. Scale bar is 100 µm. White arrow indicates the direction of the incident laser, and red arrow showing the direction of the laser writing	101
Figure 5.3		(a) Top view for line-scan at 50 mm/s, and (b) cross-sectional view of the line-scanned structure at various speed, from right (5 mm/s) to left (50 mm/s) in a step of 5 mm/s. Scale bar is 100 $\mu$ m.	103
Figure 5.4	:	(a) Cross-sectional view and (b) top view of microscope image showing the structural variations as the laser focusing depth near the surface. The focus depth was varied with 100 $\mu$ m for (a) and 10 $\mu$ m for (b). The scale bar is 50 $\mu$ m	104
Table 5.1	:	List of sample travel speeds with the corresponding number of pulses. Number of pulses have rounded to the nearest whole number	107
Fig. 5.5	:	Comparison of laser ablation depth (a), and ablation rate (b) with and without nitrogen purging. Solid symbol indicates ablation with $N_2$ purging, while hollow symbol indicates	

		ablation without N <sub>2</sub> purging. Solid lines serve to guide the eyes	109
Fig. 5.6	:	SEM images of (a) original PADC (before ablation), and laser ablation on PADC with 5 nJ pulse energy at varying number of pulses: (b) - (h) 1 x 10 <sup>5</sup> to 8 x 10 <sup>5</sup> pulses respectively	112
Figure 6.1	:	2PP SU-8 waveguide width variation at different laser writing power and scanning speed.	115
Figure 6.2	:	Bar chart showing the effect of laser fluence to the SU-8 modification state. Grey, blue, and red bar each indicate the state of SU-8 polymerization: incomplete polymerization, complete polymerization, and thermal damage	117
Figure 6.3	:	Microscope image of 2PP SU-8 waveguides produced using single-scan (a) top view, (b) side view, and (c) the respective near field image coupled with UHNA at 1550nm	118
Figure 6.4	:	Double scan waveguide with center-to-center spacing of (a) 0.4, (b) 2.2, and (c) 2.6 $\mu$ m. The scale bar is 2 $\mu$ m	119
Figure 6.5	:	Double scanned waveguide with a center-to-center spacing of 0.8 µm. (a) Top view, (b) cross-section, and (c) the near field images near field image obtained when coupled with UHNA at 1550nm.	120
Figure 6.6	:	S-bend	122
Figure 6.7	:	Bending loss simulation with Rsoft at $R=200~\mu m$ and $\vartheta=28.95^{\circ}$ . The monitoring graph on the right showing the S-bend exhibits a 50% bending loss	123
Figure 6.8	:	Simulation results showing the effects of bending radius to the bending loss of the S-bend. Waveguide width and height were 1.6 µm and 1.7 µm respectively	123
Figure 6.9	:	Variation of coupling length with the separation between two waveguides of a 50:50 directional coupler	124
Figure 6.10	:	Simulation results for a 50:50 directional coupler. Coupling length: 2.6 mm, waveguide separation distance: 2.8 μm; waveguide width: 1.9 μm, waveguide height: 1.7 μm	125
Table 6.1	:	Directional coupler design parameters	126
Figure 6.11	:	Schematic diagram of the design of the directional coupler, and the microscopic image of the direct laser written directional coupler. Symbol $L$ , $d$ , and $h$ indicate the coupling length, waveguide gap distance, and the center to branching distance.	

		In the experiment, $L$ , $d$ , and $h$ are set to 2600 $\mu$ m, 2.8 $\mu$ m, and 50 $\mu$ m respectively	127
Figure 6.12	:	Schematic diagram for the standing waveguide design	128
Figure 6.13	:	Top view of the fabricated suspended waveguide: (a) The suspended waveguide collapses due to the absence of the supporting pillars, (b) the waveguide is nicely suspended between the S-bend with the help of supporting pillars	129
Figure 6.14	:	Laser induced-damage during suspended waveguide writing	131
Figure 6.15	:	Schematic diagram of the voxel shape and size variation when focusing on (a) surface of the silicon wafer, and (b) in the SU-8 film	132
Figure 6.16	:	SEM images of the air-suspended waveguide (a) overview, and (b) close-up image of the area indicated by the red square in (a). The scale bar is 50 µm.	135

#### LIST OF SYMBOLS AND ABBREVIATIONS

A : absorbance

 $\alpha_0$ : absorption coefficient

η : Avalanche ionization rate

 $P_{avg}$  : average pulse

 $E_{\rm g}$  : bandgap energy

 $\theta$  : bending angle

L : bending loss

r : bending radius

Ca : Calcium

d : center-to-center distance

cm : centimeter

 $\lambda_{couple} \hspace{1.5cm} : \hspace{.5cm} coupling \hspace{.1cm} laser \hspace{.1cm} wavelength \hspace{.1cm}$ 

 $\tau_c$  : material cooling time

dB : decibels

 $\lambda_{write}$ : direct writing laser wavelength

me : Effective electron mass

F<sub>eff</sub> : effective fluence

N<sub>e</sub> : Electron density

eV : Electron volts

fs : femtosecond

 $a_1$ : fiber core diameter

e : Fundamental electron charge

Hz : hertz

 $\alpha$  : input angle

I : intensity

P(I) : Intensity dependent absorption rate

γ : Keldysh parameter

K : Kelvin

kHz : kilohertz

kJ : kilo-joules

 $\omega$  : Laser angular frequency

f : Laser frequency

 $L_1$ : Lens 1

 $L_2$ : Lens 2

n<sub>0</sub> : material refractive index

 $\theta_{max}$  : maximum input angle

MHz : megahertz

μJ : micro-joules

mJ : mili-joules

mm : milimeter

σ<sub>n</sub> : Multiphoton absorption coefficient

nJ : nano-joules

nm : nanometer

ns : nanosecond

n : Number of photons

N : number of pulses per irradiation spot

P<sub>3</sub> : Optical power at cross port

P<sub>2</sub> : Optical power at through port

P<sub>out</sub> : optical power measured with waveguide

P<sub>in</sub> : optical power measured without waveguide

 $\varepsilon_0$  : Permittivity of free space

ps : picosecond

h : Plank's constant

k : portion of the truncated focus spot

K : potassium

 $Pr_1$ : Prism 1

 $Pr_2$ : Prism 2

F<sub>pulse</sub> : pulse fluence

R : pulse repetition rate

dN<sub>e</sub>/dt : Rate of change of electron density

Δn : Refractive index changed

t : sample thickness

s : seconds

separation distance between input and output

h

: waveguide

SiO<sub>2</sub> : silica

Na : sodium

v : speed

c : speed of light

D : spot diameter

 $\omega_0$  : spot radius

τ : temporal pulse duration

 $\alpha_3$ : third-order absorption coefficient

F<sub>total</sub> : total fluence

2PA : Two photon absorption

2D : two-dimension

V : V-number

W : Watt

n<sub>2</sub> : waveguide cladding refractive index

a<sub>2</sub> : waveguide core diameter

a : waveguide core radius

n<sub>1</sub> : waveguide core refractive index

 $\lambda$  : wavelength

AOM : Acoustic Optic Modulator

DLW : Direct laser writing

BD : beam dump

CCD : charged-coupled device

CPA : Chirped pulse amplifier

CTE : Coefficient of thermal expansion

CR-39 : Columbia Resin - 39

CW : Continuous wave

CR : coupling ratio

DC : directional coupler

FESEM : Field emission scanning electron microscopy

FWHM : full width at half maximum

HWP : half wave plate

IR : infrared

PI\* : intermediate state of the PI after absorbing photons

IPA : isopropyl alcohol

LA : Laser ablation

LIDT : laser induced damage threshold

LTS : Linear translational stage

MFD : mode field diameter

M : monomer

R• : monomer radicals

MPA : Multiphoton absorption

MPI : Multiphoton ionization

NA : numerical aperture

OTDR : optical time domain reflectometer

PAG : Photoacid generator

PI : photoinitiator

PBS : polarizing beam splitter

PADC : poly allyl diglycol carbonate

PMMA : Polymethylmethacrylate

PTFE : Polytetrafluoroethylene

PEB : post exposure bake

SMF : single mode fiber

SA : spherical aberrations

3PA : Three photon absorption

3D : Three-dimension

Ti:Sapphire : Titanium-Sapphire

TI : Tunneling ionization

2PP : Two photon polymerizations

UHNA : ultra-hight numerical aperture

UV : ultraviolet

UV-vis : Ultraviolet-Visible

#### **CHAPTER 1**

#### INTRODUCTION

#### 1.1 Overview

Direct laser writing (DLW) is an advanced additive manufacturing technology that induces localized modification in material utilizing high intensity femtosecond laser. Here, the laser functions as a pen, emitting a focused beam of light to create arbitrary patterns on the canvas material. The canvas, on the other hand, represents the substrate or material upon which the laser creates pattern on it. The dynamic interplay between the pen (laser) and paper (material) allows for the creation of detailed and complex structures, hence the process is termed as "laser writing".

Direct laser writing often involves the focusing of high intensity laser beams into an optical material with a focusing lens. As a result, the material absorbs the laser energy, either linearly or nonlinearly, leading to localized changes of refractive index in transparent material, or polymerization in photoresist. By moving the target material across the laser focal spot, the laser induces continuous modifications in the material, enabling the creation of arbitrary structures in the three-dimensional space. One of the most interesting aspects of this technique it its exceptional precision and accuracy, reaching down to micrometer or even nanometer scale. This remarkable feature renders femtosecond laser direct writing as a potent tool for microfabrication and nanotechnology, with applications spanning across biomedical engineering, electronics, and photonics.

#### 1.2 Research Motivations

Direct laser writing with high repetition rate (>100 kHz) femtosecond laser often involves energy deposition into the transparent material by the absorption of thousands of low energy (nJ) femtosecond pulses. The high energy deposition efficiency enables rapid

material modification, making this fabrication technique excel in high throughput fabrications. However, the high energy absorption could also lead to the accumulation of thermal energy at a much faster rate than it can be dissipated from the focal spot, increasing the risk of unwanted thermal damage to the material due to the strong heat accumulation effects. Therefore, it is necessary to have a comprehensive understanding of thermal energy generation at the focal spot. This can be done by studying the thermal effect of laser writing parameters such as the pulse energy, dwell time, voxel size, and laser focus position. Manipulation of these laser writing parameters will directly impact the quality, precision, and reproducibility of the structures at the nanoscale. In addition, laser processing in different types of transparent materials requires distinctive laser treatment to achieve the desired resolution and application. This characteristic undoubtedly enhances the challenges in the fabrication process. Therefore, a comprehensive understanding of the fundamental mechanisms governing the interaction between intense femtosecond lasers with different transparent materials under various laser writing conditions will be the primary concern of this thesis.

### 1.3 Research Objectives

The main focus of this thesis is to carry out a comprehensive study of the interaction between high repetition rate femtosecond lasers and various transparent materials, namely glass, hard polymers, and photoresist. The outcomes of this study will provide significant understanding to the fundamental mechanisms governing laser-material interactions. There are 4 main objectives covered in this thesis, which are given as follows:

a) To establish the significance of different nonlinear optical responses in the interactions between high repetition rate femtosecond laser with various transparent materials.

- b) To study the light guiding characteristics of optical waveguide in soda lime glass defined using high repetition rate femtosecond laser.
- c) To investigate the modification characteristics of thermoset plastic materials using high repetition rate femtosecond laser.
- d) To fabricate 2D and 3D optical waveguide structures via two photon polymerization using high repetition rate femtosecond laser.

#### 1.4 Thesis outline

Chapter 2 provides a brief history of the advancement of DLW technology, followed by the introduction of the basic knowledge about the nonlinear absorption mechanism. A crucial aspect covered in this chapter is the explanation of two photon absorption (2PA) and laser induced optical breakdown, two important topics in the context of direct laser writing for the experiments presented in Chapter 4 and 5. In addition, the section about two-photons polymerization bears significance in the discussion of the waveguide core formation presented in Chapter 6. This chapter also provides in-depth explanation of several important concepts in laser processing, such as voxel, focus depth, and laser-induced damage threshold, each of which will be repeatedly featured throughout the dissertation.

Chapter 3 explains the laser writing system setup and the material preparation method, which is the important prerequisite of the experimental works described in this thesis. The characterization method for the fabricated devices is also featured in this chapter, including the surface morphology imaging, waveguide loss and mode field diameter measurements.

Chapter 4 explores the use of 515 nm femtosecond laser in the fabrication of optical waveguide in soda-lime glass. When high repetition rate femtosecond laser pulses are tightly focused into the bulk of a transparent material, the heat accumulation effects often cause undesired expansion of the modification area. This chapter presents the heat accumulation effects during the waveguide fabrication with DLW in soda lime glass and the technique to minimize its impact to the fabricated waveguide.

Chapter 5 discusses the laser processing in thermoset materials. The material morphological changes with varying laser processing parameters were investigated. It was found that the material morphology experiences distinctive changes when the femtosecond laser is focused within the bulk and on the surface of the materials. Based on the observations, a theoretical explanation is provided for the formation mechanism of the structure at different focusing depth.

**Chapter 6** provides an in-depth study in the fabrication of optical waveguide in photoresist. The importance of each laser processing parameter established in the previous chapters was applied to the waveguide fabrication in this chapter. Upon obtaining the optimal laser processing parameters, different waveguide structures were successfully fabricated. With the understanding of the effects of focusing depth from Chapter 5, a new 3D waveguide was simulated and fabricated.

**Chapter 7** provides an overall summary of the thesis, details some potential areas for future work and offers some concluding remarks.

#### **CHAPTER 2**

#### LITERATURE REVIEW AND BACKGROUND CONCEPTS

#### 2.1 Introduction

The roots of DLW can be traced back to the development of lasers and their applications in the mid-20th century. The invention of the world's first ruby lasers in 1960 by Theodore H. Maiman at Hughes Research Laboratories marked a significant milestone in the field of optics. The invention of laser immediately grasps the attention of researchers for using laser to study several scientific phenomena including laser spectroscopy (Archbold et al., 1964; Goldman & Rockwell, 1966; Mulvaney & Beck, 1968), nonlinear optics (Brown et al., 1965; Freund, 1968; Mocker & Collins, 1965), and biology (Goldman, Blaney, Kindel, & Franke, 1963; Goldman, Blaney, Kindel, Richfield, et al., 1963; Yules et al., 1967). However, it took several decades after for DLW to become a distinct and specialized technique. In the following years, various types of lasers were subsequently invented including the carbon dioxide (CO<sub>2</sub>) laser, argon ion laser, helium-neon (He-Ne) laser, and the semiconductor laser. Each of these laser types had distinct properties in their wavelengths and the output power, allowing for a wide range of research in different fields. The advancement of laser technology seeded the advent of the application of lasers in the manufacturing sectors such as laser cutting (Adams et al., 1965; Houldcroft, 1967; Patel, 1968), holography (Leith & Upatnieks, 1962), and laser metal deposition (Groh, 1968). These early experiments laid the foundation for the development of more sophisticated DLW methodologies. In the 1980s, researchers witnessed the emergence of titanium-sapphire (Ti:Sa) laser, which utilized crystalline of sapphire doping with the Ti<sup>3+</sup> ions as the lasing medium. The broad gain bandwidth of the crystals enables the generation of ultrashort femtosecond pulses with the pulse duration in the scales of few femtosecond (fs or  $1 \times 10^{-15}$ s) to few tens of picosecond (ps or  $1 \times 10^{-12}$ s) (He et al., 2015). In combination with the chirped pulse amplification technologies introduced in the mid1980s, femtosecond laser had achieved an intensity of more than 10<sup>13</sup> W/cm<sup>2</sup>. At such intensity, the laser can induce optical breakdown in any transparent material, inducing phase changes of the material from the initial one. This achievement marked the first step of the application of laser in material processing.

The first reported surface ablation using femtosecond laser was demonstrated on the bulk polymer material polymethylmethacrylate (PMMA). In the experiment, 300 fs UV excimer femtosecond laser at 248 nm was employed to ablate the surface of the PMMA (Küper & Stuke, 1987). This was followed by the laser ablation on fused silica using the UV excimer laser with 500 fs pulse width, which is the first reported laser ablation on glass (Ihlemann, 1992). It was soon found that the surface of the material ablated by UV laser often suffers from severe thermal damage due to the high linear absorption of the laser energy. To overcome this, H. Kumagai *et al* suggested to perform laser surface ablation with the multiphoton absorption mechanism, where Ti:Sapphire femtosecond laser (798 nm) was used for the first time over UV laser in laser ablation (Kumagai et al., 1994). The experiment demonstrated that laser ablation with infrared femtosecond laser has a similar ablation rate as the ablation with UV laser, however the thermal damage around the ablated region is significantly minimized. This result shows multiphoton absorption mechanism as a promising candidate in material micromachining with laser, to produce features with better structural modification and greater resolutions.

Up until then, the laser ablation experiment was limited to the surface of the material. The breakthrough of the laser material processing was saw in 1996 by Hirao *et al* (Davis et al., 1996), in which amplified 810 nm Ti:Sapphire femtosecond laser was employed to induce positive refractive index change within variety of dielectric material, demonstrated the capabilities of the DLW technique to create waveguide structure within bulk glasses for the first time. Since then, femtosecond laser index refractive index modification was applied in the processing of various hard material such as the glasses (Ehrt et al., 2004;

Lei et al., 2023; Sugioka et al., 2014; Tan et al., 2021) and the crystals (Jia et al., 2020; Li et al., 2022; Lipateva et al., 2023; Zhang et al., 2020). The development of the ultrafast femtoseconds pulsed laser also seeded the foundation of two-photon polymerization (2PP), which is a new fabrication technique that utilizes the nonlinear absorption of two-photons to induce polymerization within polymer material. The discovery of the 2PP techniques opens up the new possibility for the fabrication of three-dimensional polymer structures with sub-micrometer precision. Development of new material that is suitable for photopolymerization has been the primary concern of the research to enable the creation of high-resolution three-dimensional structure for application ranges from photonics to tissue engineering (Brown et al., 2023; Maruo et al., 2008; Sarker et al., 2023). In short, DLW represents the culmination of historical advancements in laser technology and the exploration in laser applications for fabrication purposes. From the early applications of laser to the development of direct laser writing technique, DLW continues to evolve, offering immense potential for the design and fabrication of intricate and functional structures.

#### 2.2 Direct Laser Writing with Ultrafast Femtosecond Laser

Direct laser writing (DLW) is a maskless photolithography technology that creates patterns on a material using a focused laser beam. This technique is particularly suitable for rapid prototyping and can produce complex structures with high precision and resolution (Abou Khalil et al., 2017; Chen et al., 2018; Gao et al., 2020; Jiang et al., 2016; Kelemen et al., 2019; Liu et al., 2015; Liu et al., 2020; McMillen et al., 2012; Nguyen et al., 2011; Nolte et al., 2009; Schröder et al., 2012). By focusing the laser beam inside bulk material with a microscope objective, localized refractive index modification can be made at the laser focal point. Both continuous wave (CW) laser (Mueller et al., 2014; Nguyen et al., 2016; Thiel et al., 2010; Tong et al., 2016) and pulsed laser (Lipatiev et al., 2017;

Marshall et al., 2006; Sakellari et al., 2012) can be used for DLW, depending on the types of target material and the resolution required. However, pulsed laser with ultrashort pulse durations (~250 fs) are typically used for fabrication of feature sizes smaller than the diffraction limit resolution of light ( $\lambda/20$ ) (Li et al., 2009). Davis et al demonstrated the first femtosecond laser induced optical breakdown in transparent material (Davis et al., 1996). By using an amplified 800 nm Ti:Sapphire femtosecond laser pulses, they successfully induced positive index changes inside a variety of dielectric materials. These results paved a new path for photonics waveguide fabrication in which waveguiding devices, who functions the same as the existing optical fiber, can be directly written within active or passive bulk materials simply by moving the sample across the laser focusing point. A rather fascinating feature of direct writing with femtosecond laser is that the material surrounding the focal point will remain unaffected by the laser due to the highly nonlinear nature of the laser absorption by the material. This particular feature enables the creation of embedded three-dimensional waveguide at arbitrary depth within the bulk material. The embedded waveguide design introduced greater tolerance of the fabricated devices to the changes of the environmental conditions, allowing the fabrication of photonics devices for various applications.

Direct laser writing had been used to fabricate complex photonic devices such as optical waveguide (Abou Khalil et al., 2017; Baghdasaryan et al., 2021; Chen et al., 2018; McMillen et al., 2012), diffraction gratings (Goraus et al., 2018; Marshall et al., 2006), splitters (Abou Khalil et al., 2017; Gašo et al., 2020; Wu et al., 2022), directional couplers (Ng et al., 2022), and optical memory devices (Bellec et al., 2008). Altering the local refractive index via laser induced material breakdown is the dominant process for waveguide fabrication in transparent materials. With the proper laser exposure conditions, positive or negative index changes could be induced at the laser focal spot. Type I (Fletcher et al., 2011; Will et al., 2002), II (Cheng et al., 2022; Jia et al., 2023;

Shimotsuma et al., 2003), or III (Okhrimchuk et al., 2005) waveguides can be fabricated accordingly, depending on the sign of the refractive index change.

In contrast to the laser induced damage in transparent material, multiphoton polymerization is used for device fabrication in photoresists material. In this case, the solution of monomers is exposed to the femtosecond laser, which are selectively polymerized at the laser focal point. The unexposed regions are then removed with the chemical developer, leaving the free-standing polymerized waveguide structures on the substrate. In both types of the materials, waveguiding regions are defined simply by moving the material in respect to the laser focal spot. Different types of material would have varying responses to the incoming laser including the structural modification, index changed, modification threshold, etc. It is interesting to investigate the modification of these material with different writing condition such as laser intensity, fluence, objective lens NA, and the focusing depth. Understanding the material modification under different writing conditions could assist in developing waveguide with better quality and performance. Considerable works have reported that slight differences in the writing conditions could affect the waveguide performance in many ways i.e. optical losses, waveguide dimensions, waveguide mode profile, numerical apertures, index changed, etc (Bhardwaj et al., 2005; Burakov et al., 2007; De Michele et al., 2019; Hernandez-Rueda et al., 2017a; Huot et al., 2007; Liu et al., 2006; Marcinkevičius et al., 2003; Xiong et al., 2023). These effects will be further explored throughout this dissertation.

#### 2.3 Physics of Direct Laser Writing

In the following section, the underlying physical mechanism of light-matter interaction in direct laser writing will be explained in detail with the goal of providing sufficient understanding for the work presented in this dissertation. The basic physics leads to the laser induced damage in transparent material will be discussed, which involves the nonlinear absorption and nonlinear ionization in the transparent material.

#### 2.3.1 Optical Absorption

Dielectric material tends to have a distinct energy bandgap,  $E_g$ , separating the valence band and the conduction band. When a photon with energy equal to or greater than the bandgap propagates through the medium, the photon will be linearly absorbed, causing an electron to be excited from the valence band into the conduction band (Figure 2.1a). It is commonly known that the energy, E of a photon is inversely proportional to its wavelengths,  $\lambda$ , following the relationship of  $E = hc/\lambda$ , where h is the Planck's constant and c is the speed of light. For wide bandgap dielectric such as glasses, only UV photons have sufficient energy to linearly excite a valence electron into the conduction band. At longer wavelengths, however, the photons no longer have sufficient energy to promote electronics transition. This means that the photons can now propagate through the glass freely without being absorbed, and thus, the glass is said to be transparent to the photons. In general, glass is transparent over a broad range of wavelengths, often spanning from UV to infrared, in which optical absorption of light at these wavelengths is improbable.

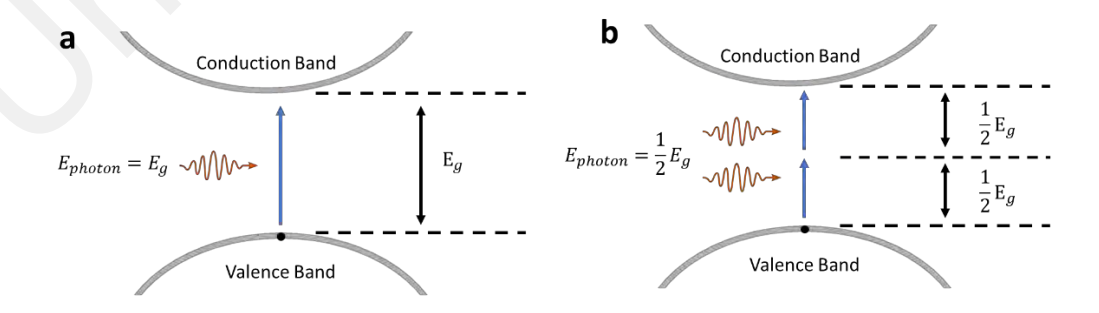


Figure 2.1. Schematic diagram of electron excitation from valence band to conduction band in (a) one-photon absorption and (b) two-photon absorption

However, Göppert Mayer found the exceptions to this condition in 1931 (Göppert - Mayer, 1931). She deduced that at sufficiently high laser irradiances, the nonlinear response of the medium will give rise to multiphoton absorption at the "transparent" wavelength range. As shown in Figure 2.1 (b), two or more photons will be absorbed by an electron simultaneously, in which the combined total energy exceeds the bandgap of the medium, which can then excite the electrons to their excited state. Multiphoton absorption was initially seen as an unwanted loss mechanism but is extremely sought after for applications that require nonlinear interaction between optical field with the medium, such as direct laser writing (Cao et al., 2023; Mainik et al., 2024; Song et al., 2024). Since multiphoton absorption is a nonlinear process, it can only occur within a highly localized volume in which the laser intensity is sufficiently high. This nonlinear behavior allows localized modifications within bulk material at arbitrary depth, creating optical devices for a broad range of applications.

#### 2.3.2 Multiphoton Absorption and Ionization

Multiphoton absorption (MPA) is a nonlinear phenomenon where two or more photons are absorbed by an electron in a single absorption event. MPA is the primary mechanism to initiate nonlinear interaction of material with high intensity laser in the nonlinear regime. It is highly intensity dependent with the absorption rate  $P(I) = \sigma_n I^n$ , where  $\sigma_n$  is the multiphoton absorption coefficient for n-photons absorption(Jones et al., 1989). If the total absorbed energy exceeds the medium's  $E_g$ , electrons can be excited from valence band into the conduction band, generating free carriers within the medium. The ionization of electrons via MPA is also known as multiphoton ionization (MPI). The total number of photons, n required during MPI is the minimum integer that satisfies the relation  $nhf \geq E_g$ , where h is the Planck's constant, and f is the laser frequency. On the other

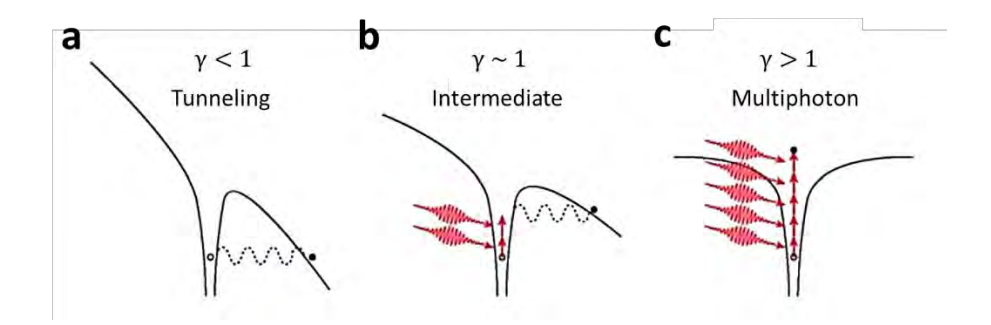


Figure 2.2. Schematic diagram of the photoionization of an electron in an atomic potential for different values of the Keldysh parameter. Image derived from (Schaffer, Brodeur, Mazur, et al., 2001).

hand, free carriers can also be generated via tunneling ionization (TI). This ionization process arises from the spatial distortion of the energy band in the presence of an extremely intense electric field that suppresses the Coulomb potential well binding the valence electrons to their atoms, increasing the probability of an electron to tunnel through the potential barrier into the conduction band which is normally impossible.

Both MPI and TI are responsible for generating free carriers during the interaction of high intensity laser with a material. As a rule of thumb, MPI dominates at higher intensity and longer wavelengths, whereas TI is an intensity independent ionization mechanism that occurs more dominantly at shorter wavelengths. The degree at which MPI or TI contributes to a photoionization event can be determined by the Keldysh's parameter,  $\gamma$  (Keldysh, 1965):

$$\gamma = \frac{\omega}{e} \sqrt{\frac{m_e cn \epsilon_0 E_g}{I}} \tag{2.1}$$

where  $\omega$  is the laser angular frequency, e is the fundamental electrons charge,  $m_e$  is the effective electron mass, c is the speed of light, n is the refractive index of the target material,  $\varepsilon_{\theta}$  is the permittivity of free space, and I is the laser intensity at the focal point. According to Keldysh, TI dominates when  $\gamma < 1$ , whereas MPI dominates when  $\gamma > 1$ 

(Figure 2.2). There exists an intermediate state at  $\gamma \sim 1$ , in which the ionization takes place through the combination of both processes. It is important to note that the reference value "1" is somewhat arbitrary and it is often modified to adapt to different experimental setup (Ams et al., 2012; Tan et al., 2016; Zheltikov, 2016). In some cases, researchers might use different values (eg:  $\gamma = 1.5$ ) to account for their specific experimental conditions or assumptions made in their simulation model.

#### 2.3.3 Avalanche Ionization

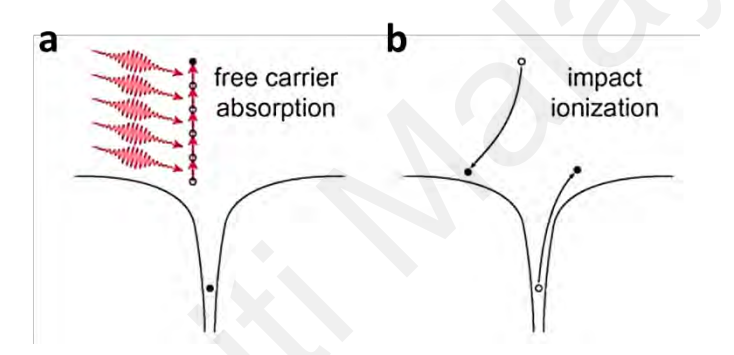


Figure 2.3. Schematic diagram of avalanche ionization. Image taken from (Schaffer, Brodeur, Mazur, et al., 2001).

Avalanche ionization is an important mechanism to initiate laser induced damage inside a transparent material. The avalanche effect usually started with some seed electrons that already reside in the conduction band. This can occur either by the photoionization event such as MPI or TI, by thermally excited electrons, or by the impurities in the material (Schaffer, Brodeur, Mazur, et al., 2001). These seed electrons will sequentially absorb the energy from the incoming photons linearly, moving to the higher energy states within the conduction band, as shown in Figure 2.3 (a). After the absorption of n photons, where n satisfies the relation  $nhf \ge E_g$ , the electron now has energy much higher than the conduction band minimum. These energized electrons then transfer their energy to other valance band electrons through collision, liberating them into the conduction band, as

shown in Figure 2.3 (b). This collisional event will produce two excited electrons near the conduction band minimum, each of which readily to continue absorb the laser energy through free carrier absorption and further impact-ionized the remaining valence band electrons (Ams et al., 2012; Schaffer, Brodeur, Mazur, et al., 2001). The process will continue as long as the electric field is present, leading to an exponential growth of the electron density,  $N_e$  in the conduction band in a rate of:

$$\frac{dN_e}{dt} = \eta N_e \tag{2.2}$$

where  $\eta$  is the avalanche ionization rate.

# 2.3.4 Laser Induced Optical Breakdown

Once sufficient energy was deposited in the material via the absorption mechanism described above, the rapid buildup of large free carrier density will give rise to material modification or damage. Avalanche ionization dominates when the laser pulse durations are at the order of 10 ps or more (Schaffer, Brodeur, Mazur, et al., 2001). At this pulse duration regime, the laser intensity is normally insufficient to directly photoionized the electrons by the laser itself. Thermally excited electrons or impurities within the bulk material are important to provide the seeds electron for avalanche ionization. Large energy deposited on the material due to the long pulse duration provides sufficient time for the exponential growth of the electron density to excite the modification. However, the rapid buildup of free carriers is often associated with the destruction of the material. Therefore, extra care needs to be taken while working with picosecond laser to prevent severe material damage. In contrast, femtosecond laser at the same pulse energy level could induce modification without causing significant damage to the substrate as compared to the pico- and nanosecond laser due to the shorter pulse durations. The biggest

advantage of using femtosecond laser is that it could start an avalanche ionization by itself without having the seeds electron from thermally excited electrons or impurities, due to the high peak intensity of the laser pulse (Lenzner et al., 1998). Photoionization with femtosecond pulse is achieved by the leading edge of the pulse, which is enough to generate sufficient free carriers for avalanche ionization during the remaining of the pulse duration (Stuart et al., 1996; Stuart et al., 1995). Owing to the shorter pulse duration, pulse energy is absorbed faster than it is transferred to the lattice, resulting in minimized collateral damage to the surrounding material. Hence, material modification with ultrafast femtosecond laser enables more precise, confined, and controllable modified region around the focus voxel. The results of this deterministic optical breakdown threshold and controllable material damage make femtosecond laser an ideal tool for material micromachining.

# 2.4 Two Photons Polymerization

Two-photon polymerization (2PP) is a new DLW technique based on the concept of 2PA that enables the creation of arbitrary three-dimensional structure in the photosensitive polymer or known as photoresist (Pillai et al., 2023; Wang et al., 2023). Similar to DLW in transparent material, 2PP involves focusing high intensity femtosecond laser into the photoresist to induce photochemical reaction that modifies the chemical structure of the photoresist. There are two types of photoresists namely positive-tone photoresist and negative-tone photoresist, in which they respond differently towards the light exposure. For instance, positive photoresist tends to become more soluble in a chemical developer after exposure, whereas negative photoresist will become less soluble upon exposure. The difference in the chemical reaction lies in the chemical structure of each type of photoresist.

### 2.4.1 Positive Photoresist

Positive photoresist is a type of resist that contains high molecular weight polymer. In the polymer consists of a photoactive compound called photoacid generator (PAG). This compound is sensitive to light and undergoes chemical change when exposed to a specific wavelength. Upon light irradiation, the PAG absorbs the light energy and the electrons in the compound excite to a high energy state. The excited PAG undergoes a bond cleavage reaction, breaking down the polymeric chain into multiple monomers or polymers with lower molecular weight. This reaction leads to the generation of a reactive species, which is typically a strong acid or a radical. The generation of the polymer radical cause changes in the solubility of the photoresist, making it more soluble in a base-type chemical developer. When working with a positive photoresist, the exposed region is generally removed by the developer, whereby the unexposed region will be left on the substrate with the desired pattern. Therefore positive photoresist is not suitable in DLW as it is inefficient to scan across the photoresist film to remove the unwanted region.

## 2.4.2 Negative Photoresist

Negative photoresist, on the other hand, is a type of photoresist where the exposed region toughens and becomes insoluble to the developer. In general, a negative photoresist contains monomers, oligomers, and photoinitiator (PI). When the negative photoresist is exposed to light, the PI will absorb the photon energy and undergoes a photochemical reaction. This reaction generates free radicals and other reactive species to initiate the polymerization process. The generated free radicals react with the monomers or oligomers present in the negative photoresist, leading to the sequential addition of monomers, creating polymer chains within the exposed regions. This process is known as polymerization. The generated reactive species can also form covalent bonds between

the polymer chain or within the polymer chain itself, which is a process called cross-linking. The results of polymerization and crosslinking at the exposed regions led to the formation of a three-dimensional network structure in the photoresist. The crosslinked regions in the negative photoresist become less soluble in the developer solution compared to the unexposed region. Therefore, the solubility difference allows for selective removal of the unexposed regions during the development process, leaving behind the desired pattern. In DLW, three-dimensional structure can be created by moving high intensity femtosecond laser within the negative photoresist to induce polymerization and cross-linking along the desired path. The unexposed region who remains soluble will be selectively removed by the developer, leaving behind the crosslinked areas on the substrate.

# 2.4.3 Photopolymerization Induced by Two Photon Absorption

Most photoresist that can be polymerize under single photon absorption can undergo similar photochemical reaction with two photon absorption (2PA), provided the laser intensity is sufficiently large. In this case, PI is excited to higher energy state by absorbing two photons simultaneously. This process forms the initial radicals which is an important process to generate monomer radicals by attacking the monomers or oligomers. The process is known as photoinitiation and can be described with the formula (Zhou et al., 2015):

$$PI \xrightarrow{2h\nu} PI^* \to R \bullet + R \bullet$$
 (2.3)

where  $R^{\bullet}$  is the monomer radicals, hv represents the energy of a photon, and  $PI^{*}$  is the intermediate state of the PI after absorbing photons. The process is then followed by a chain propagation, in which the radicals combine with the monomers or oligomers to form the monomer radicals:

$$R \bullet + M \to RM \bullet \stackrel{M}{\to} RMM \bullet \dots \to RM_n \bullet$$
 (2.4)

The monomer radical will then combine with another monomer to form a new monomer radical, and the new monomer radical will proceed to combine with another monomer to form a new monomer radical. As a result, the monomer radicals expanded in a chain reaction forming a long polymeric chain. The process will keep repeating until one radical meets with another monomer radical, when the process is terminated:

$$RM_n \bullet + RM_m \bullet \to RM_{m+n}R$$
 (2.5)

It is interesting to note that, electrons excitation during MPI in photoresist is not to a bound excited state. Instead, the electrons are excited to an unbound state where one or more electrons are separated from their molecules (Müller, 2015). Therefore, the laser absorption and excitation could be done by the monomer itself and thus, PI is not necessarily required. However, in some cases PI with selected optical properties is still needed for efficient radical generation.

In a negative tone photoresist, covalent bonds are formed between the polymeric chains as the polymerization reaction proceeds, creating a crosslinked polymer network (Faraji Rad et al., 2021). Cross-linking in SU-8 requires thermal treatment, which can be done by heating the exposed substrate with a hotplate, where the process is commonly known as post-exposure bake. The cross-linked polymer then becomes insoluble to the chemical developer. By subsequently developing the exposed photoresist, the unpolymerized/unexposed region will be removed, leaving the solid free-standing polymer structure on the substrate. SU-8 is a negative-tone photoresist with a refractive index of about 1.57 at 1550 nm. By properly design the dimension and shape of the polymer structure, the resin can serve as the core of a waveguide. Cladding material could be added to the surrounding to protect the waveguide. At the same time, the cladding

material can also reduce the index contrast of the waveguide, thus improving the scattering loss of the device. Details of the fabrication process is provided in Chapter 6.

# 2.5 High Repetition Rate Femtosecond Laser for Direct Laser Writing

High repetition rate laser is a type of laser that emits pulses of light at an exceptionally high frequency, typically ranging from hundreds of kilohertz (kHz) to several megahertz (MHz). This high frequency allows the laser to produce a large number of pulses per second, resulting in a higher energy delivery rate to the target material as compared to the low repetition rate laser. Therefore, high repetition rate laser offers significant advantage in direct laser writing such as increased writing speed and improved refractive index contrast (Shane M Eaton et al., 2011; Little et al., 2008). However, the shorter interval between pulses, often less than the material cooling time, causes insufficient time for the thermal energy to dissipate between successive pulses. This leads to an increase in local temperature within the laser focal volume, causing a larger diameter size of the modified zone (Eaton et al., 2005; Miyamoto et al., 2011), which undermines the precision required for micro-fabrication. While heat accumulation effects can be mitigated by adjusting the pulse energy and scanning speed, the literature on this topic remains limited. Therefore, this dissertation aims to fill this gap by providing valuable insights and contributing additional knowledge on the response of transparent material to high repetition rate lasers.

## 2.6 Direct Laser Writing in Glass

Material processing has attracted tremendous attention from both the scientific and technology community. In particular, the use of femtosecond laser in creating 3D microstructures in transparent material has opened up new possibilities for 3D photonics integrated circuits (Li et al., 2023). The primary interest involves controlling the positive

or negative index changes within the laser affected region under various exposure conditions. Davis *et al* discovered that femtosecond laser can induced refractive index changes, Δn of 10<sup>-2</sup> to 10<sup>-3</sup> within bulk glasses (Davis et al.). By focusing high intensity laser into the glass, the deposited energy will create local index modification via thermal expansion. In their report, permanent optical waveguide was produced by translating the glass sample in both perpendicular and parallel direction to the optical axis, inducing continuous refractive index changed along the path of the laser focus spot. Since then, the effect of different processing parameters such as laser wavelength, polarization, intensity, pulse energy, pulse durations, and repetition rate had been intensively studied and reported for a variety of glasses with different composition including fused silica (Shane M. Eaton et al., 2011; Shah et al., 2005), borosilicate (Dharmadhikari et al., 2011; Eaton, Ng, et al., 2008; Kowalevicz et al., 2005; Mittholiya et al., 2017; Zhang et al., 2006), chalcogenide (Hughes et al., 2007; McMillen et al., 2012), and doped-glasses (Thomson et al., 2010).

Fundamental study on the structural behavior of the glasses to the femtosecond laser paves the pathway to the creation of the optical devices i.e. beam splitters (Mittholiya et al., 2017), waveguide gratings (Zhang et al., 2006), directional couplers (Kowalevicz et al., 2005), and sensors (Kamata et al., 2005). As one of the commercially available glass, low loss waveguide (0.3 dB/cm at 1550 nm) was first demonstrated in borosilicate glass (Eaton, Ng, et al., 2008). The report showed that heat accumulation effect was one of the key factors to produce waveguide in bulk glass by varying the pulse energy and repetition rate. Dharmadhikari *et al* then presented the slit beam shaping method to produce a symmetrical waveguide cross-section in borosilicate glass (Dharmadhikari et al., 2011). By using the similar approach, a 3-D 1x4 splitter was successfully fabricated with an insertion loss of 16.3 dB at 1550 nm (Mittholiya et al., 2017). Raman analysis by Wu *et al* revealed that the laser induced waveguiding region in borosilicate glass was due to the

increase of local refractive index by the compression of two expansion regions (Wu et al., 2021). Heat accumulation effect also plays a significant role in high refractive index ( $\Delta n > 1 \times 10^{-2}$ ) fused silica waveguide writing (Shane M Eaton et al., 2011; Shah et al., 2005). Shah *et al* was the first to demonstrate waveguide writing in fused silica using a frequency doubled laser (522 nm), producing a waveguide with high refractive index of 1 x  $10^{-2}$  at 1550 nm. The coupling loss and propagation loss of the fabricated waveguide were 1.4 dB and 0.9 dB/cm respectively, demonstrating the great performance of the waveguide. Later, Eaton *et al* reported the highest reported index contrast ( $\Delta n = 0.022$  at 1550 nm) in fused silica waveguide writing, by enhancing the heat accumulation effect using a 1.25-NA oil immersion objective lens at 522 nm.

## 2.6.1 Nonlinear Absorption in Glass

Borosilicate, fused silica, and soda-lime are the popular examples of glasses that offer over 90% UV transparency across the broad spectrum of visible light. The high transparency of the glasses is a results of their optical energy band gap, which is 9 eV for fused silica (DiStefano & Eastman, 1971; Lancry & Poumellec, 2006; Sudrie et al., 2002), 3.3 eV for borosilicate (Mansour et al., 2021; Yadav et al., 2013), and 3 eV for soda lime (Ali et al., 2018; Shehata et al., 2019). The broad band gap characteristics signify that nonlinear absorption processes take precedence when utilizing visible and near-infrared femtosecond laser to induce modifications in these glasses. For instance, when processing fused silica with femtosecond lasers at wavelengths of 515 nm, 800 nm, and 1030 nm, it requires 4 photons, 6 photons, and 8 photons, respectively, for absorption. Table 2.1 provides an overview of the nonlinear absorption coefficient of various glasses in the visible to near-IR range. Notably, borosilicate and soda-lime glass exhibit high two-photons and three-photons absorption coefficient, making them an ideal choice for laser

Table 2.1: Nonlinear absorption coefficient of borosilicate glass, fused silica glass, and soda-lime glass.

Glass	λ (nm)	2PAx10 <sup>-12</sup>	3PAx10 <sup>-24</sup>	Ref
		(cm/W)	(cm3/W2)	
BS	354.7	13		(Smith, 1981)
BS	532	2.9		(White et al., 1985)
BS	532	0.4		(White et al., 1985)
BS	800	1.5	1	(Jamshidi-Ghaleh et al., 2009)
BS	800		0.645	(Andrásik et al., 2020)
BS	800		0.635	(Andrásik et al., 2020)
BS	800		2.7	(Okhrimchuk et al., 2009)
FS	532	< 0.2		(Boudebs & Fedus, 2009)
FS	800	0.48		(Mary et al., 2015)
FS	1064	<0.2		(Boudebs & Fedus, 2009)
SL	800	5.79		(Moghaddam & Jamshidi, 2010)
SL	800		0.828	(Andrásik et al., 2020)
SL	800		21	(Jamshidi-Ghaleh et al., 2005)

<sup>\*</sup>BS: Borosilicate; FS: Fused Silica; SL: Soda Lime

processing within this wavelength range. Comprising a mixture of silicon dioxide, sodium oxide, calcium oxide, magnesium oxide, and aluminum oxide, the soda lime glass possesses notable high nonlinear absorption coefficient (2PA: 5.79 cm/W (Moghaddam & Jamshidi, 2010) and 3PA: 21 cm³/W² (Jamshidi-Ghaleh et al., 2005), measured at 800 nm). Nonlinear absorption is an intensity dependent phenomenon, meaning that optical absorption and material modification occurs only above a certain threshold laser intensity. By precisely control the intensity of the laser at the focal spot, nonlinear absorption can be confined within a desired volume, allowing localized modification within the material.

This high precision modification is crucial for achieving fine spatial resolution in DLW, allowing for the creation of detailed structures at the nanoscale. Soda-lime glass exhibits a bandgap of 3.5 eV (Shehata et al., 2019) suggested that nonlinear absorption is necessary for optical absorption at 515 nm (2.4 eV). This characteristic opens up possibilities for modification of soda-lime glass using 515 nm femtosecond laser.

# 2.6.2 Coefficient of Thermal Expansion and Direct Laser Writing

The coefficient of thermal expansion (CTE) also plays a crucial role in determining the suitability of glass for a given DLW project. CTE quantifies a material's response to temperature changes, indicating how much it expands or contracts. In general, a high CTE suggests significant expansion with temperature fluctuations, while a low CTE implies stability with minimal size changes. Fused silica stands out with its exceptionally low CTE value (0.55 x 10<sup>-6</sup>/K) (White, 1973) when compared to borosilicate glass (3.3 x 10<sup>-6</sup>/K) <sup>6</sup>/K) (Bouras et al., 2009) and soda lime glass (Dannemann et al., 2012; Ohdaira et al., 2008) (9.35 x 10<sup>-6</sup>/K). This makes fused silica an excellent choice for crafting microoptics via DLW. In fused silica, the optical waveguide fabricated often closely match the voxel size, with no observable heat affected zone around the core. Heat-affected zone is a zone which is thermally modified by laser energy, expanded outwards from the centre of the laser focal spot. The coverage of the heat-affected zone mainly dependent on the CTE of the material, the pulse duration, and the dwell time of the laser. DLW in borosilicate and soda lime glass typically produces larger core sizes with heat-affected zone, which attributed to glass deformation due to thermal expansion (Eaton, Ng, et al., 2008; Eaton, Zhang, et al., 2008).

Materials with a high CTE value are typically avoided in micro-fabrication processes due to their high sensitivity to temperature changes. In the context of DLW, where heat accumulates at the focal spot, the thermal expansion characteristics implies a considerable enlargement of the modified area. This expansion poses challenges in achieving fine spatial resolution for micro-fabrication. However, the elevated temperature sensitivity also suggests that lower pulse energy is sufficient to induce modifications within the materials with a high CTE value. The advantage of this characteristics featuring material modification with high pulse repetition rate femtosecond laser with lower pulse energy. Therefore, precise modifications in soda-lime glass can be achieved at a pulse energy lower than the pulse energy required for the modification of fused silica (Huang et al., 2011a) as well as improved fabrication efficiency by taking advantage of its rapid thermal responses. While borosilicate and soda lime glass may not be ideal for microstructure creation, their higher CTE values support rapid thermal response during laser processing, allowing material modification in these glasses with lower pulse energy compared to fused silica (Huang et al., 2011b). Combined with their cost-effectiveness and the ready availability, these glasses offer advantages over fused silica when efficient micro-processing and rapid prototyping are the primary considerations.

## 2.6.3 Soda Lime Glass for Direct Laser Writing

Despite being a commercially available glass, soda-lime glass received minimal attention in waveguide writing (Dyakonov et al., 2016; Kowalevicz et al., 2005; Minoshima et al., 2001; Tong et al., 2006). Most report involves waveguide fabrication using high repetition rate (1 - 25 MHz) at 800 nm, whereas only one reported waveguide writing using frequency doubled 515 nm femtosecond laser (Dyakonov et al., 2016).

In addition, it is found that the waveguide characterization was mostly carried out using visible wavelengths i.e. 633 nm, and 800 nm, whereas the performance of soda lime glass waveguide in the 1550 nm remains inadequate. Therefore, an experiment was

designed and presented in Chapter 4, with the aim of filling in the research gap of soda lime glass waveguide in the telecommunications wavelengths, while at the same time building the foundation of waveguide writing system in the lab, as well as understanding the importance of each laser processing parameters in femtosecond laser waveguide writing.

## 2.7 Laser Ablation in Hard Polymer

Laser ablation (LA) using femtosecond (fs) laser has garnered much attention for fabrication of micro- and nano-structural devices. Upon focusing the fs laser on the surface of a material, nonlinear excitation followed by ionisation can lead to structural changes at the laser focus area. Despite limited knowledge on the actual mechanism of LA, a general concept may be explained based on several ablation processes, including electrostatic ablation, thermal ablation, and non-thermal ablation (Gamaly et al., 2006; Gamaly et al., 2002). A substantial number of studies have looked into the effects of varying ablation parameters on the quality of ablated structures including substrate material, optical power, laser pulse duration, and pulse repetition rate (Biswas et al., 2016; Chichkov et al., 1996; Day & Gu, 2005). The fabricated structure had found various applications in optical waveguide, microfluidic channels, and optical memory storage devices (Chen et al., 2018; Shane M. Eaton et al., 2011; Hsieh et al., 2017; Parthenopoulos & Rentzepis, 1989; Wlodarczyk et al., 2018).

Generally, LA involves high energy laser with pulse energy that ranges between micro-joules (μJ) and mili-joules (mJ). Prior studies have assessed ablation in some polymer substrates, namely poly(methyl methacrylate) (PMMA), polycarbonate, polyethylene, and polytetrafluoroethylene (Baudach et al., 2000; De Marco, Eaton, Suriano, Turri, Levi, Ramponi, Cerullo, Osellame, et al., 2010; Ravi-Kumar et al., 2019).

De Marco et al investigated the surface ablation on PMMA using femtosecond laser operating at 800nm with 1 mJ of pulse energy (De Marco, Eaton, Suriano, Turri, Levi, Ramponi, Cerullo, & Osellame, 2010). They observed that the femtosecond laser ablation had altered the surface wettability of PMMA, enabling PMMA to be used as microfluidic channel. Krüger et al. then compared the behaviour between doped and undoped PMMA. They realized that the incubation effect by multiple pulse ablation was more pronounced in pure PMMA than the doped-PMMA, due to different ablation threshold (Krüger et al., 2005). Wang et al. extended their study into comparison of the ablation efficiency of Teflon PTFE at different pulse fluence, and found that the ablation efficiency drops during the ablation in air due to air ionization (Wang et al., 2003). In most cases, fs laser is used with chirped pulse amplifier (CPA) system to produce laser pulses with pulse energy large enough to overcome optical breakdown threshold of the targeted material. On the other hand, the low optical breakdown threshold of polymer substrates allows the use of non-amplified fs laser system that delivers low energy pulses at high repetition rate. Although the pulse energy from these systems (nJ) is insufficient to cause direct ablation, studies have reported that the impact of heat accumulation due to irradiation of high repetition rate laser pulses may effectively minimise optical breakdown threshold, thus leading to thermal ablation in the material. Considerable research works have been carried out on high repetition rate pulse laser ablation. Belaud et al. investigated the ablation of polypropylene at different laser conditions i.e. intensity and number of pulses (Belaud et al., 2014). They reported an increase in ablation depth with higher number of pulses due to the energy accumulation of multiple pulses. Baudach et al. then demonstrated the reduction in ablation threshold of polycarbonate and PMMA due to the heat accumulation effect (Baudach et al., 2000). Day et al. fabricated microfluidic channels in bulk PMMA substrate using a 800nm laser with a pulse repetition rate of 82 MHz (Day & Gu, 2005). Due to the high repetition rate, the pulse energy they used in the experiment was only 0.9

nJ, which is about 6 orders of magnitude smaller than the pulse energy used by De Marco *et al.* as aforementioned (De Marco, Eaton, Suriano, Turri, Levi, Ramponi, Cerullo, & Osellame, 2010). The above findings have proven the potential of ultrafast laser ablation using high repetition rate laser. Nonetheless, surface ablation of polymer substrate using low energy and high repetition rate laser seems to be an unexplored area.

# 2.7.1 CR-39 for Direct Laser Writing

CR-39, also known as poly allyl diglycol carbonate (PADC), has been extensively applied in many research and technological domains. The term "CR-39" refers to the abbreviation "Columbia Resin – 39", which stands for the 39<sup>th</sup> formula of this thermosetting plastic by the Columbia Resins project in 1940. In particular, CR-39 is commonly used as a solid-state nuclear track detector and in eyeglass lenses (El Ghazaly & Hassan, 2014; Lounis-Mokrani et al., 2003; Zaki et al., 2015). CR-39 exhibits an outstanding transparency within the visible and NIR spectrum and is almost completely opaque in the ultraviolet range, corresponding to an optical energy band gap between 3.15 eV to 3.81 eV (Nidhi et al., 2009; Sagheer et al., 2016; Shekhawat et al., 2011; Traynor et al., 2018). This high transparency rendered it a suitable material for optical device application.

The refractive index of CR-39 in the visible wavelength region is 1.498 (El Ghazaly & Hassan, 2014). The Z-scan analysis by Rafique *et al.*, revealed that CR-39 exhibited third-order nonlinearity with third-order absorption coefficient,  $\alpha_3 = 1.0 \pm 0.3 \times 10^{-24} \, \text{cm}^3$  W<sup>-2</sup>, which makes it a promising candidate for nonlinear optical applications. These properties ensure precise control of laser beams, allowing for the creation of intricate and high-resolution structures. CR-39 also exhibits low chromatic dispersion (Chandrinos & Reviews, 2021), minimizes chromatic aberration during DLW, resulting in higher quality and more precise fabrication. Additionally, CR-39 cost effectiveness is of paramount

importance in DLW research and development. It provides an economically viable option for creating prototypes and experimental setups, making it an accessible choice for scientists and engineers in the photonics and DLW industry. These properties collectively underscore CR-39's suitability and value in the DLW domain, enabling the precise fabrication of micro-optical and photonics devices for a wide range of applications. An experiment was presented in Chapter 5 to assess the surface ablation of CR-39 using low energy and high repetition rate laser operating at 800 nm. Energy deposition onto CR-39 sample was achieved via multiphoton absorption at 800 nm and straight trenches were ablated by translating the sample across the laser focal point.

# 2.8 Microfabrication with SU-8

SU-8 is a commonly used, high aspect ratio epoxy-based negative photoresist that is designed for microfabrication where a thermally and chemically stable structure is desired. Upon exposure to UV light, photochemical reaction will trigger cross-linking process where the exposed region toughens, while the remaining unexposed region remains soluble and can be washed away during chemical development. Its primary constituent is an epoxy resin such as bisphenol A, providing the material's structural framework. The formulation often includes cyclopentanone as the solvent, to facilitate spin-coating onto substrates. By adjusting the viscosity of the SU-8, film thickness of 0.5 μm to > 200 μm can be achieved with a single coating process. The SU-8 employed in the experiment was SU-8 2002 and SU-8 2010, each of which can produce a maximum film thickness of 3 μm and 20 μm, respectively. Similar to all the other optical materials, SU-8 offers exceptional optical transparency across visible and NIR spectrum. Above the wavelength of 400 nm, SU-8 exhibits over 95% of transparency, making it optically transparent at the telecommunication wavelength at 632.8 nm and 1550 nm. SU-8 is therefore suitable for

optical device application. Additionally, it boasts the capability to produce structures with high aspect ratios, making it ideal for crafting complex 3D microstructures. SU8's thermal stability allows it to endure elevated temperatures without distortion, while its strong adhesion to various substrates, along with its chemical resistance, broadens its utility across diverse DLW applications. These properties collectively position SU-8 as a versatile and reliable material for DLW, facilitating the creation of sophisticated optical devices.

As a traditional UV-lithographic photoresist, SU-8 has been widely used to produce various kinds of micro-devices such as microfluidics channels (Ayoib et al., 2016; Garcia et al., 2009), waveguide and optical devices (Hamid et al., 2015; Piruska et al., 2006; Yang et al., 2008), and biosensors (Esinesco et al., 2005). Due to its high transmittance in the infrared wavelengths, SU-8 has also piqued interest in two-photon lithography using near-infrared intense laser sources. Its capabilities of creating localized, sub-surface device patterning via two-photon polymerization (2PP) make SU-8 one of the best photoresists for 3D microfabrication, which has diverse applications in many advanced fields (Maruo & Fourkas, 2008). A considerable amount of research has been carried out to study the processing characteristics of SU-8 2PP. Ohlinger *et al* investigated the wavelength dependence of 2PP in SU-8 between 720 nm – 780 nm and successfully created undistorted 3D microstructures using the direct laser writing technique (Ohlinger et al., 2011). Tsutsumi *et al* then created SU-8 micro-lens array via 2PP and used it to produce various microstructures (Tsutsumi, Hirota, et al., 2017).

# 2.8.1. 2D/3D Waveguide Fabrication with SU-8

Despite the promising results of 2PP in the fabrication of micro-optical devices, there are not many reports on the planar optical waveguide fabrication in SU-8 using direct laser

writing (DLW), specifically single mode optical waveguide. In fact, to the best of the author's knowledge, there is only one report on the SU-8 planar waveguide fabrication via DLW (Ramirez et al., 2017). However, the reported waveguide was fabricated using one-photon polymerization technique, instead of 2PP. Therefore, the information on the characteristics of single-mode SU-8 waveguide produced via 2PP using near-infrared laser sources remains very limited.

The potential of SU-8 in waveguide fabrication has been extended into the 3D space. Schumann et al demonstrated a 3D bridge waveguide which can function as a polarization rotator and for a free standing polymer disk resonator (Schumann, Bückmann, et al., 2014a). The group demonstrated the flexibility of DLW by producing a rotational bridge waveguide with low loss and high conversion efficiency. Following that, there were a few reports on the fabrication of photonics wire bonding for both out-of-plane and in-plane coupling between the waveguide chips (Lindenmann et al., 2012; Lindenmann et al., 2011). The design effectively reduces the lateral distance between the waveguides as compared to the conventional fiber coupling technique. Adão et al then proposed a suspended waveguide design for on-chips optical interconnects (Adão et al., 2022). Their design consists of a parametric curve waveguide a tapered between the surface waveguide and the suspended waveguide, as well as to support the waveguide to be suspended in the air. A similar design was presented by Gao et al but the suspended waveguide was fabricated for efficient fiber coupling applications, with the aim of circumventing the need to cleaving the waveguide end facet while preserving the coupling efficiency (Gao et al., 2020). These reports demonstrated that the flexibility and potential of DLW in photoresists for the fabrication of 3D optical waveguide for photonics integrated circuits applications. However, it is undoubtedly that the research is still in its infancy and requires further exploration. With that, a thorough study on the fabrication and characterization of single-mode SU-8 waveguide with a 780 nm femtosecond laser is designed and presented in Chapter 6 of this thesis.

Multiple straight channel waveguides were fabricated under different fabrication conditions i.e. laser writing power and scanning speed, to obtain the desired processing window to create a single mode optical waveguide. With the information obtained, a directional coupler with a 50:50 coupling ratio had been successfully fabricated and characterized. To further establish the viability of this fabrication technique, an air suspended waveguide was fabricated. This suspended design finds application as a waveguide overpass in high level photonics integrated circuit (Nesic et al., 2019; Xu et al., 2018b), whilst the high refractive index air-clad polymer waveguide can be used to fabricate waveguide with smaller dimension and bending radius (Li et al., 2018; Marinins et al., 2016).

## 2.9 Physics of Voxel

Direct laser writing has been a powerful microfabrication technique that revolutionizes the precise and intricate creation of three-dimensional structures. At the heart of the DLW lies the concept of a volume pixel (voxel), which is a three-dimensional pixel that serves as the fundamental building blocks for constructing complicated structures at high precision and accuracy. The voxel often forms a prolate spheroidal shape at the focal point, as shown in Fig. 2.4 (a). Three-dimensional structure can be constructed by placing the voxels in close proximity to induce overlapping between the voxels as demonstrated in Fig. 2.4 (b). By harnessing the properties of laser and transparent material, DLW enables the fabrication of structures voxel by voxel, offering unprecedented control over their shape and size in a three-dimensional manner.

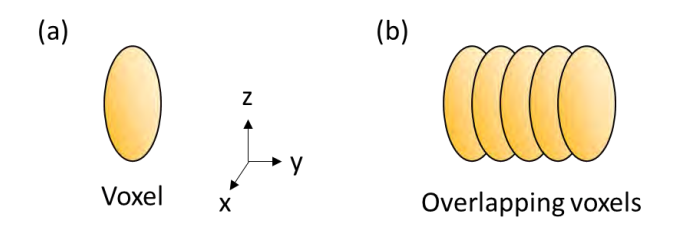


Figure 2.4. Schematic diagram of the (a) voxel, and (b) overlapping voxels in DLW.

DLW system typically employs laser beams to selectively expose or modify a transparent material. The laser beam is directed onto the material, and through mechanisms such as two-photon polymerization or laser ablation, the material is either modified or removed, voxel by voxel. By controlling the laser intensity and scanning the material through the laser beam, complex three-dimensional structures can be created by the overlapping of numerous voxels together, as shown in Figure 2.4. In this context, the size of the voxel plays an important role as it directly influences the resolution, accuracy, and the quality of the fabricated structure. Smaller voxel size corresponds to higher resolution helps create structures with finer details as well as enable more precise control over the shape of the fabricated structure. Using small voxel size in DLW can also minimize the surface roughness of the fabricated structure, resulting in the final product with a smoother surface. However, fabrication of large structure with small voxel will require multiple steps and longer time to complete the fabrication. Therefore, it is not always correct to use very small voxel size in DLW. Instead, it is rather important to understand the resolution and accuracy required for that particular fabrication, then adjust the voxel size accordingly to optimize the fabrication efficiency while maintaining the quality of the fabricated products.

There are several factors that influence the size of the voxel in DLW such as the focusing lens, characteristics of the laser, and optical properties of the target material. Understanding these factors is an important step to leverage the fabrication process with exceptional resolution and efficiency. By controlling the laser beam and manipulating the

material modifications voxel by voxel, DLW empowers researchers to explore in areas such as microfabrication (Balena et al., 2023; Fatkullin et al., 2004; Maruo & Fourkas, 2008), additive manufacturing (Ali et al., 2020; Grabulosa et al., 2023), and nanotechnology(Fischer et al., 2013; Kostovski et al., 2014), opening doors to limitless possibilities from biomedical engineering (Selimis et al., 2015; Turner et al., 2014; Yu et al., 2022), electronics (Teh, 2017), photonics (Yang et al., 2020), and beyond.

### 2.9.1 Focus Lens

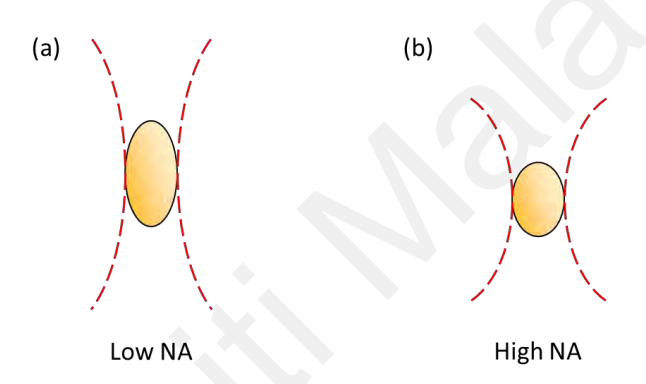


Figure 2.5. Voxel formed by (a) low NA lens, and (b) high NA lens.

Microfabrication with DLW typically involves focusing high energy laser into the sample with a focusing lens. The primary purpose of the lens is to concentrate the laser beam into a small spot, thereby achieving a higher power density at the focal point which is essential for material modification. Moreover, concentrating the laser beam into a smaller volume creates a small voxel size at the focal spot for precise fabrication. The voxel size at the focal spot can be determined by the lens properties such as numerical aperture (NA) and focal length of the lens. The NA of a lens determines the acceptance angle for the incoming light as well as the cone angle for the focused laser beam. A higher numerical aperture corresponds to a wider cone angle, thus creating smaller voxels facilitating the fabrication of finer details and higher precision in the final structures, as shown in Figure 2.5. In DLW system, laser beam is usually tightly focused with high NA lens to

concentrate the laser energy to achieve sufficient energy to induce material modification or ablation within a small volume. On the other hand, focal length determines the distance between the lens and the focal point, where the laser beam at its smallest beam waist diameter. A shorter focal length results in a short focusing distance, leading to a larger focusing angle and smaller voxel size. Conversely, a long focal length produces a longer focal distance and larger voxel. By carefully selecting the NA and focal length of the lens, it is possible to manipulate the spot size diameter to achieve the desired resolution of the structures.

There are two types of focusing lenses used in DLW namely spherical lens and objective lens. Objective lenses commonly have higher NA than spherical lens, therefore objective lens is used when the fabrication requires sub-micrometer resolution and precision (Landowski et al., 2017; Schumann, Bückmann, Gruhler, Wegener, Pernice, et al., 2014; Trautmann et al., 2019), whereas spherical lens is used during the fabrication of larger structures where high fabrication resolution is not the primary consideration (Kim & Xu, 2003; Lafleur et al., 2019). The focused beam diameter by the spherical lens is directly proportional to its focal length and can be estimated with

$$2\omega_0 = \frac{4\lambda f}{\pi D} \tag{2.6}$$

where  $\omega_{\theta}$  is the focused beam radius,  $\lambda$  is the laser wavelengths, f is the focal length of the lens, and D is the beam diameter at lens. Following that, the focused beam diameter by an objective lens can be approximated using

$$2\omega_0 = \frac{1.22\lambda}{NA} \tag{2.7}$$

where *NA* is the numerical aperture of the objective lens. It is important to note that the voxel size is also influenced by other factors such as the optical properties of the material, characteristics of the laser beam, laser beam profile, and spherical aberrations. However,

Equations (2.6) & (2.7) can provide a good estimation for initial planning of the experiment and optimization of the fabrication process.

#### 2.9.2 Continuous Wave Laser and Pulsed Laser

To understand how the voxel size can be controlled with a laser, it is important to note that voxel size is not only the minimum spot size achievable with the focused laser beam. A more accurate description for the voxel is the minimum volume achievable which the material can be selectively modified or interact with the incoming laser beam. While the spot size at the focal spot contributes to the size of the voxel, the laser beam properties will also influence the overall dimension of the voxel. There are two types of lasers used in DLW, namely continuous wave (CW) laser and pulsed laser. The difference in the properties of these lasers can significantly influence the voxel characteristics, offering distinct advantages for controlling the size of the voxel created.

CW laser is a type of laser that emits a continuous beam of coherent light, where the output power remains constant over time. When using a CW laser for DLW, the voxel size is primarily controlled by the optical power and exposure time of the laser. By adjusting the power of the laser, the energy deposited into the material can be varied, affecting the size of the voxel. Higher power leads to larger voxel, while lower power results in a smaller voxel. Following that, the exposure time, or the total irradiation time of the laser at a specific location, will also affect the voxel size. Longer exposure creates larger voxel, whereas short exposure time forms a smaller voxel. Therefore, controlling the laser power and exposure time can adjust the voxel size when doing DLW with a CW laser (Smolík et al., 2022; Thiel et al., 2010).

Pulsed laser, on the other hand, emits laser light in the form of pulses. Instead of providing a steady stream of laser beam, the laser emits short pulses of high intensity light.

Due to the unique temporal characteristics of pulsed laser, it offers additional control of the voxel size in DLW on top of the laser power and exposure time. With pulsed laser, the voxel size can be controlled by other factors including the pulse duration, pulse repetition rate, energy per pulse, and the beam scanning speed (Figure 2.6). By adjusting these parameters, precise control of the voxel size can be achieved.

Pulses duration refers to the temporal period in which the laser stays "on". In DLW, the pulse duration used typically ranges from nanosecond (ns) to femtosecond (fs). When using pulses with long pulse duration, the energy deposition occurs over a relatively longer period. This extended interaction time can lead to thermal effects such as heat accumulation effect. The accumulated heat will then dissipate into the surrounding material, resulting in a large modification area or voxel. In contrast, short pulse duration laser such as femtosecond laser offers greater temporal confinement of laser energy. These ultrafast lasers deliver pulses with high peak power within a short period of time, minimizing the thermal effects. The short interaction time confines the energy deposition into a smaller volume, resulting in a smaller voxel size. Therefore, ultrafast laser is commonly used in DLW where high fabrication resolution is required. By adjusting the pulse duration, it is possible to manipulate the voxel size to adapt to the fabrication requirements, i.e. long pulse duration when large feature sizes are desired, while short pulse durations are preferred for achieving finer details and higher fabrication accuracy.

Repetition rate refers to the frequency at which laser pulses are emitted by the pulse laser system. It represents the number of laser pulses per unit time, often expressed in hertz (Hz), kilohertz (kHz), or megahertz (MHz). The repetition rate affects the temporal spacing between each consecutive pulses, where high repetition rate refers to a larger number of pulses during a given time period. During the DLW process, consecutive laser pulses could overlap if the repetition rate is too high (MHz). Overlapping of the laser pulses might create larger voxel due to the heat accumulation by the large number of laser

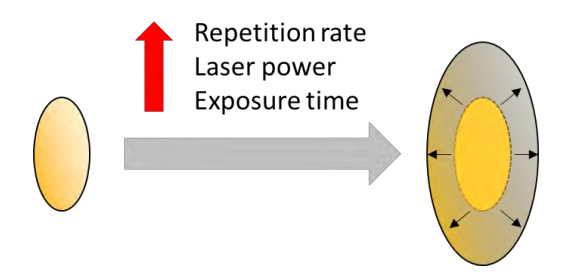


Figure 2.6. Schematic diagram showing the enlargement of voxel size with the increase of pulse repetition rate, laser power, and the exposure time.

pulses illuminating on the same area. Conversely, low repetition rate (< 1 kHz) laser has a longer time period between the pulses which allow the material to cool down. In this case, the heat accumulation is minimized or neglected and thus offering fabrication with smaller voxel. However, using low repetition rate laser in DLW limits the material processing speed. This is to avoid the separation of the voxels when processing the material at higher speed and causing discontinuity on the final products. Therefore, it is important to consider the desired processing speed and the need for resolution and efficiency of the fabrication. High repetition rate laser offers faster material processing speed but may lead to larger voxel and potential heat accumulation. A low repetition rate laser then offers greater spatial resolution but may result in slower processing speed. Optimizing the repetition rate allows the adjustment to achieve the desired processing speed, voxel size control, and the fabrication efficiency.

Pulse energy refers to the amount of energy contained in a single laser pulse emitted by the pulsed laser system. In DLW, pulse energy directly influences the total amount of energy transferred into the material during the fabrication process. There is a threshold energy requirement to induce modification in every transparent material. Once sufficient energy is deposited onto the material, this energy can induce various physical and chemical processes around the voxel, such as cross-linking, polymerization, ablation, or melting, depending on the specific characteristics of the target material. Higher pulse

energy tends to produce larger voxels due to the increased energy deposition and therefore a broader region of modification. Meanwhile, low pulse energy provides smaller voxels with better energy confinement. It is important to optimize the pulse energy used for DLW to ensure optimal material modification and avoiding unwanted damage to the material. Insufficient pulse energy may result in incomplete material modification or inadequate material removal. On the other hand, excessive pulse energy might lead to thermal damage of the material. Therefore, it is important to find out the optimal pulse energy for that particular fabrication, to obtain a balance between achieving the desired dimensions and material properties, while avoiding detrimental damage to the material.

Laser scanning speed refers to the rate at which a laser is moved or scanned across the sample during the DLW process. It is a critical parameter that directly affects the fabrication efficiency, and quality of the fabricated product. The scanning speed is the most complicated factor of all in controlling the voxel size as it interacts with all the other factors mentioned above. For example, a slower scanning speed combined with low laser power, short pulse duration, and low repetition rate can result in small voxel size, enabling high resolution fabrication. However, if the pulse repetition rate increases, a faster scan speed is required to avoid overlapping of the laser pulses for potential thermal damage. Every change in the laser properties required the adaptation of the laser scanning speed to achieve the desired fabrication properties. Therefore, it is extremely difficult but important to optimize the laser scanning speed accordingly with the laser parameters for precise control over the voxel size, which directly affects the fabrication resolution, efficiency, and the quality of the fabricated structures.

## 2.10 Depth Dependent Laser Interaction

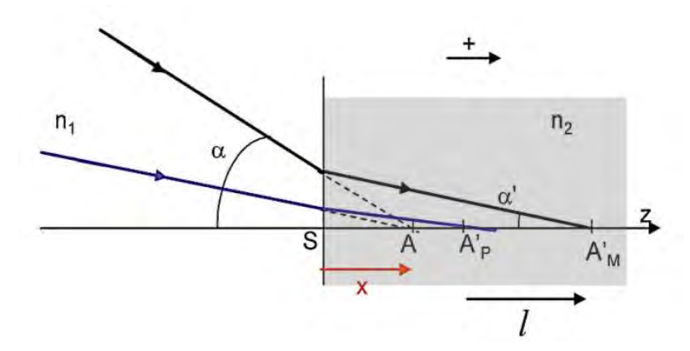


Figure 2.7. A sketch map of laser focusing across a plane interface from air into the sample. Image taken from (Huot et al., 2007).

In DLW, femtosecond laser is typically focused on bulk material using an objective lens. Objective lenses with higher NA can focus the laser beam into a much smaller focal spot, not only improving the modifications resolution, but at the same time enhanced the laser intensity locally to enhance he nonlinear absorption. Most of the commercially available objective lens are designed with a specific correction factor to match with the refractive index (n = 1.522) and thickness (0.17 mm) of the cover glass used for microscopic imaging. This type of objective lens correction is needed to prevent spherical aberrations introduced by the cover slip mounted on top of the specimen, which could result in distorted or blurred images. However, since the target material (transparent material or photoresist) used for DLW could have different refractive index than the said cover glass, spherical aberrations may be significant while carrying out direct laser writing, specifically for 3-D device fabrication where the focusing depth is constantly varying during the process. Therefore, understanding spherical aberrations is extremely important and will be discussed in this section.

Spherical aberrations (SA) are caused by the refractive index mismatch between the sample and the immersion medium, which can be air or immersion-oil, depending on the objective lens NA used in the laser writing. As shown in Figure 2.7, assuming if there is

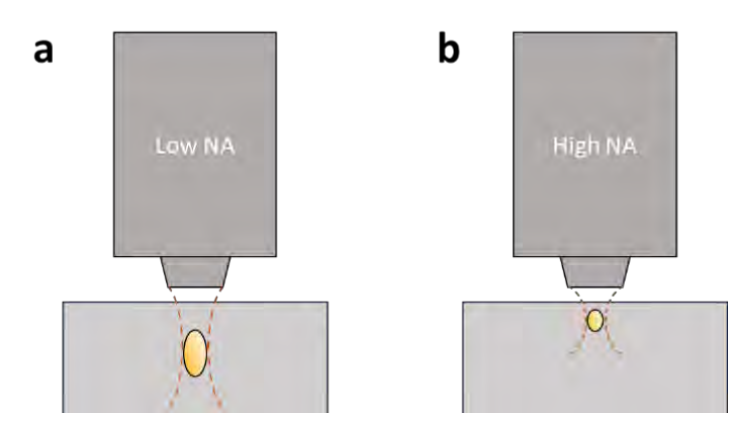


Figure 2.8. Schematic diagram showing the focusing depth into the material by (a) low NA, and (b) high NA objective lens. Objective lenses with higher NA has larger focusing angle than the low NA objective lens, therefore the maximum focusing depth of high NA objective lens is closer to the sample surface.

no index mismatch between the medium, the laser will be focused on position A. However, due to refraction at the interface between two non-identical mediums, the actual focus spot is shifted towards position A'<sub>P</sub> and A'<sub>M</sub>, whereas the shifted position is dependent on the input angle  $\alpha$ . For higher value of  $\alpha$ , the ray converges to the marginal spot A'<sub>M</sub>; while for lower value of α, the ray converges to the paraxial spot A'<sub>P</sub>. The outcome is the focused beam extended longitudinally along the optical axis, forming an anti-symmetry voxel at the focus spot. The elongation of the spot size within the medium causes the reduction of laser intensity at the focal point, as well as enlarging the effective volume of the modifications. Several factors could affect the amount of spherical aberrations including the objective lens NA (Hnatovsky et al., 2005), refractive index mismatch (Sun et al., 2005; Williams et al., 2012), and focus depth (Gross & Withford, 2015; Huang et al., 2016; Liu et al., 2006; Marcinkevičius et al., 2003). Hnatovsky et al reported that high-NA objective are more susceptible to the spherical aberration effect as compared to the low-NA objective (Hnatovsky et al., 2005). With low-NA objective it is possible to induce laser modification at a depth of more than 10 mm without concern of intensity drops, whereas high-NA objective lens (NA = 0.90) might be restricted to a few tens of

micrometer beneath the surface of the silica glass before the intensity reduced to below the threshold energy to induced significant material modifications, as shown in Figure 2.8.

# 2.11 Laser Induced Damage Threshold

Laser-induced damage threshold (LIDT) refers to the maximum level of laser energy or power that an optical material can withstand before it experiences permanent damage or degradation. It is a critical parameter in laser applications as exceeding the LIDT can lead to irreversible damage, reducing the performance of the fabricated structure. In the practical point of view, the current peak power of the free-space laser is limited by the damage threshold of the optical components in the system. Understanding the mechanism responsible for the optical damage could help in the construction of optical components with higher damage threshold. On the other hand, laser ablation at the surface and within the bulk of transparent material had been applied for optical micromachining of photonics devices. A better grasp on the idea of the nonlinear interaction between high power laser and the transparent material may allow for better precision and efficiency in the micromachining process. It is found that the damage threshold will be affected by the properties of the material and the laser, thus careful experimental testing and characterization are required to determine the LIDT of that specific material in that particular laser writing system.

## 2.11.1 Wavelength

Direct laser writing in transparent material involves the absorption of laser energy, leaving irreversible damage at the laser focal spot. The absorption rate generally depends on the material properties and the wavelength of the laser. In transparent material, there

exists an energy gap separating the conduction band and the valance band of the material, known as the optical bandgap, E<sub>g</sub>. Depending on the bandgap, one or more photons with total energy larger than the bandgap are required to promote the excitation of the valence band electrons into the conduction band. The absorbed energy then contributes to the heating and damage within the material. Simanovskii *et al.* have studied the wavelength dependence LIDT for wide and narrow bandgap materials, for visible to mid-infrared picosecond laser (Simanovskii *et al.*, 2003). It is found that the damage threshold for narrow bandgap material is typically lower than the wide bandgap material and it is independent of the wavelength at the mid-IR regime. Similar observations was reported by Gallaias *et al.*, where they revealed the linear dependency of LIDT with various materials of increasing bandgap (Gallais et al., 2015). While tunneling ionization also exhibits no wavelength dependence (Keldysh, 1965), it is believed that tunneling ionization alone is sufficient to induce breakdown in narrow bandgap material.

In the visible region for wide bandgap material, however, it is found that the damage threshold increases with the wavelength since more photons are needed for multiphoton ionization in longer wavelengths. The drop in the photoionization rate with wavelength greatly suppresses the growth of electron density in the conduction band, leading to weak avalanche reactions to cause damage. The increase of LIDT of wide bandgap material with the incident laser wavelength at visible to near-infrared has been reported by several studies in the femtosecond timescale (Gallais et al., 2015; Jia et al., 2006; Migal et al., 2019). For the mid-IR wavelengths, on the other hand, tunneling ionization dominates the photoionization process and contributes to the growing of the electron density with impact ionization (Grojo et al., 2013; Jia et al., 2006). The conduction band electron density becomes sufficiently strong to develop the avalanche ionization, causing the formation of dense electron plasma leading to laser absorption and damage (Migal et al., 2019; Simanovskii et al., 2003). The high efficiency of avalanche ionization in the generation

of electron density has thus lowered down the damage threshold fluence in this wavelength regime.

### 2.11.2 Pulse Duration

Many studies have dealt with the temporal effects of laser induce damage, as the length of the pulse duration will greatly affects the evolution of the ionization process. In the event of laser ablation of dielectric material with pulse duration longer than a few tens of picosecond, the initial seeds electrons in the conduction band are very important to excite the avalanche ionization. For such pulse, the intensity is typically too low for photoionization. Therefore, avalanche ionization is the primary process to produce sufficient electron density in the conduction band to induce optical damage in transparent material (Stuart et al., 1995). The absorbed energy will then transfer to the lattice over the pulse duration. The extended interaction time between the long pulse and the transparent material allows the thermal energy to diffuse out from the focal point via thermal diffusion. This slower thermal accumulation causes the relatively higher damage threshold when using long pulse. The heat generated has longer time to spread and dissipate, thus reducing the local temperature around the focal point. Damage occurs only when the accumulated temperature at the irradiated region is high enough to cause the material to melt or fracture. Since the energy is deposited into the material by the laser pulses, and transfer to the lattice by thermal diffusion, the damage threshold is determined by the rate of pulse energy deposition and the thermal diffusion rate of the material. Theoretical model predicted that the threshold fluence to induce damage scales with the square root of the temporal pulse duration,  $\tau^{1/2}$  (Stuart et al., 1996).

The LIDT for sub-picosecond or femtosecond lasers is differ significantly from pulse laser with longer pulse durations due to the unique characteristics of ultrashort pulses.

Despite the shorter pulse duration, ultrashort pulses have extremely high intensity that is able to directly photoionizing the valence band electrons. At such high intensity, nonlinear effects become more prominent, enabling nonlinear photoionization such as multiphoton ionization, and tunneling ionization. These ionization mechanisms can excite electrons from their valence band to the conduction band in the leading edge of the pulse (Stuart et al., 1996), producing a large density of seeds electrons in the conduction band for avalanche ionization during the rest of the pulse. Because the pulses are so short, the avalanche ionization occurs at a much faster rate than they can be cooled down by phonon emission. Only after the laser pulse is gone, the absorbed energy is transmitted from the electrons to the lattice. This shock-like energy deposition creates localized ablation in the transparent material with essentially no collateral damage to the surrounding lattice. The self-seeded avalanche ionization also makes short pulse higher efficiency in producing conduction band electrons, therefore the damage threshold for ultrashort pulse is much lower than the long pulse. Experimental work showed the deviation of  $\tau^{1/2}$  scaling when the pulse duration is < 10 ps. The damage threshold still reduces with the pulse width, but at a slower rate (Stuart et al., 1996).

# 2.11.3 Spherical Aberrations

Spherical aberrations can influence the LIDT by degrading the beam quality. Spherical aberrations cause different parts of the beam to focus on different positions, leading to the formation of a larger focal spot size and reduced power density at the intended focal point. A larger focal spot size means that the laser energy is distributed over a larger area, resulting in a lower energy density. Consequently, the LIDT increases as higher energy is needed to have sufficient energy to damage the material. Marcinkevičius *et al* demonstrated the laser induced damage threshold (LIDT) in silica glass varies with the

focusing depth due to spherical aberrations (Marcinkevičius et al., 2003). Since the aberration increases with the focusing depth, the focal spot enlarged as the light focus deeper into the material, thereby reduce the maximum intensity dramatically (Hnatovsky et al., 2005). To compensate for the intensity drop demand an increased in pulse energy during the writing process. Similar observations had been reported by Liu et al., 2006) in their attempt of waveguide writing using 1 kHz femtosecond laser in silica glass. At a focus depth of < 150 μm, the range of pulse energy to induce smooth index change is strictly narrow and the sample is easily damaged with slightly increased pulse energy. However, the energy range is broadened as the focusing depth increased, providing a better degree of freedom in choosing the suitable pulse energy for the fabrication. A 3x3 waveguide array of non-symmetrical output was fabricated by producing waveguide of different aspect ratio, making use of the spherical aberrations at different focusing depth. In a nutshell, SA could either be an unwanted phenomenon that should be prevented at all costs or making use of it to produce devices with specific applications. The effect of SA could be seen throughout this dissertation, whereas Chapter 6 will provide details on how SA affects the 3D waveguide fabrication.

### 2.12 Conclusion

In this chapter, the fundamental principle and current advancements in the field of direct laser writing of transparent materials using high repetition rate femtosecond laser has been explored. The basic mechanisms of laser-material interactions are discussed, highlighting the unique characteristics of femtosecond laser that make them particularly suitable for precise micro-fabrication. Thermal effects that arise during direct laser processing with high repetition rate femtosecond laser has been the main concern of the dissertation. Through a comprehensive review of recent literature, it is found that there are several important parameters that influence the quality and efficiency of laser-induced

modification with high repetition rate laser, which includes pulse duration, laser fluence, focus spot size, and writing speed. Precise control over these parameters is of paramount importance to overcome the thermal effects and further enhance the capabilities of direct laser writing techniques. The insights gained from this chapter lay a solid foundation for the experimental investigations and methodologies that will be detailed in the subsequent chapters.

### **CHAPTER 3**

### **EXPERIMENTAL METHOD**

### 3.1 Introduction

This chapter provides a detailed description of the experimental setups used throughout the works presented in this dissertation, together with the physical/optical characterization methods used. Section 3.2 presents the laser sources used; Section 3.3 shows the sample alignment technique used in all the experimental work included in this thesis; Section 3.4 describes the UV-Vis spectroscopy technique; Section 3.5 to 3.7 explains the laser writing setup for different experiments; Section 3.8 show the sample preparation method; and Section 3.9 explains the waveguide characterization method that was used in each experimental work, which include the measurement for the propagation loss, mode field diameter, and refractive index change.

## 3.2 Ultrafast Femtosecond Laser System

### 3.2.1 Ti:Sapphire Tsunami Femtosecond Laser

The Tsunami Ti:Sapphire laser source is a high-power class IV mode-locked femtosecond laser oscillator manufactured by Spectra-Physics. The active medium of the laser is a Titanium-doped Sapphire crystal, optically pumped by a continuous wave (CW) laser at 532 nm (Millenia Prime) which can supply up to 10 W of optical power. At a pump power of 7 W, the maximum output power of the femtosecond laser is about 1 W measured at 780 nm wavelength. Since the Tsunami is a mode-locked pulsed laser, its pulse repetition rate is determined by the laser cavity length, which is approximately 3.75 m. In this case, the laser operates at a pulse repetition rate of 80 MHz, which yields a maximum pulse energy of 12.5 nJ. To account for the long cavity length, the laser employed a folded-

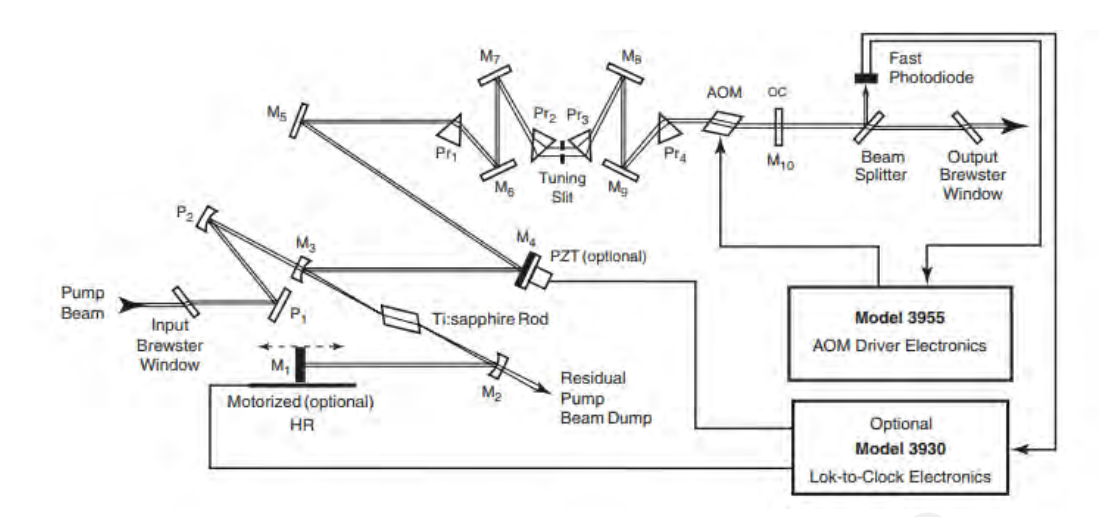


Figure 3.1. Laser beam path in a Spectra-Physics Tsunami Ti:Sapphire mode-locked laser system (Spectra-Physics, 2002)

cavity design as shown in Figure 3.1, to optimize the laser performance in a minimal space. The laser system can continuously produce femtosecond laser pulses with a tunable wavelength from 690 nm to 1080 nm, with a pulse duration ranging from < 50 fs to 80 ps, depending on the optics used. Wavelength selection and pulse width optimization of the output laser can be controlled by adjusting the position of the prism (Pr<sub>2</sub> and Pr<sub>3</sub>), as well as the tuning slit. The wavelength was tuned to 800 nm and 780 nm for the experimental work presented in Chapter 5 and Chapter 6, respectively. Although the laser cavity can produce sub-50 fs pulses, the actual pulse width used for the experimental writing was about 120 fs due to pulse stretching by the external optics throughout the entire experimental setup presented in Section 3.3.

### 3.2.2 NKT OneFive Origami XP

The OneFive Origami XP laser is a high pulse energy laser manufactured by NKT. The laser has a dual-wavelength laser outputs, in which the nominal wavelength is 1030 nm, which can be converted to 515 nm via the built-in second harmonic generator, as shown in Figure 3.2. The pulse duration of the laser is less than 300 fs, with a tunable pulse



Figure 3.2. Picture of the NKT OneFive Origami XP high energy femtosecond laser.

repetition rate from 50 kHz to 1 MHz. A much lower repetition rate can be achieved with the pulse division control function provided by the laser system. The controller uses Acoustic Optical Modulator (AOM) to block certain number of pulses periodically, effectively reducing the pulse repetition rate. This laser system operates at constant laser power mode, whereas the pulse energy changes with the pulse repetition rate. The highest pulse energy achievable is  $40~\mu J$  at 100~kHz when the laser wavelength is 1030~nm. Laser pulse energy and repetition rate are controlled with the software provided with the laser system. For the work presented in Chapter 4, the laser was set to 515~nm at 100~kHz repetition rate to provide a sufficient range of pulse energies for the intended study.

# 3.3 Sample Alignment

Sample alignment is a crucial procedure during DLW to precisely position the sample to be perpendicular to the optical axis of the laser. It is an important step in DLW experiment when high accuracy of the laser focusing depth is required. Properly aligning a sample

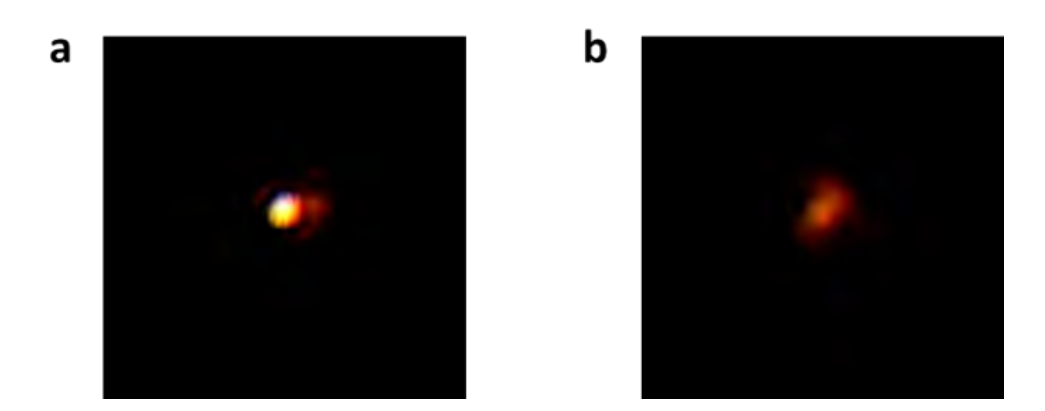


Figure 3.3. Beam profile image captured by a CCD camera when the laser focus position is (a) on the sample surface, and (b) away from the sample surface with a 40x (0.65 NA) objective lens.

can avoid certain unwanted experimental errors when focusing depth is one of the essential variables. For instance, a poorly aligned sample can result in the variation of laser focusing depth during the laser writing process, which will then affect the fabricated dimensions of the structure due to spherical aberrations, as stated in Section 2.5.

To ensure that the laser is focusing on the sample surface across the entire area of interest, a laser alignment system has been established. The alignment system consists of a laser source, alignment stage, and a CCD camera. The laser source employed for alignment was also the laser utilized for material processing but at a much lower laser power. Typically, the laser source will be tuned to continuous wave (CW) operation instead of a pulsed laser during sample alignment to avoid nonlinear modification or damage to the sample during the writing process. This low power laser will be focused onto the sample with an objective lens, where the back-reflected laser beam from the sample surface will be captured by a CCD camera to visualize the focused laser beam on the sample. A bright and sharp image should be observed when the laser is focused on the surface of the sample, while a more diverged or blurred image will be seen when the laser focusing spot moves away from the sample surface. An example of the CCD images for

both scenarios is shown in Figure 3.3 below. By inspecting the images of the back-reflected beam, one can identify the laser focusing position.

It is important to note that, in this alignment system the laser focusing spot is static at one point, while the target sample is moving around the focal spot on a 3-axis translational stage. The stage should consist of a pair of x- and y-axis which were used to move the sample around the laser focal spot, and another translational stage to move the sample in the z-direction to adjust the position of the sample surface with relation to the focal spot. Additional rotational stages could be added, if necessary, to control the angular position of the sample. Once the sample alignment is completed, a bright spot across the entire sample surface area of interest should be observed while moving the sample along with the x- and y-axis.

# 3.4 UV-Vis Spectroscopy

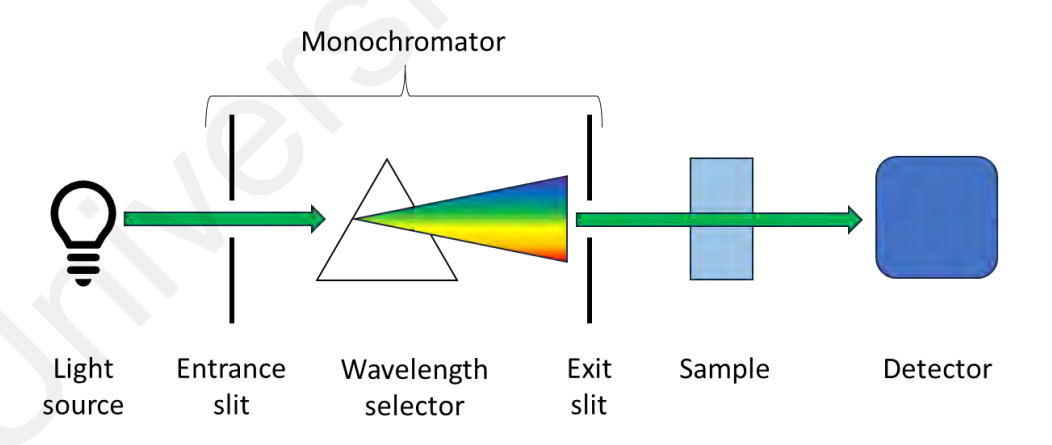


Figure 3.4. Schematic diagram of the main components in a UV-Vis spectrophotometer.

UV-vis spectroscopy is a widely used analytical technique in both chemistry and physics that measures the amount of light absorbed or transmitted through a sample, in comparison to a reference material or a blank sample. The term "UV-Vis" is the

abbreviation for "Ultraviolet-Visible", which refers to the range of wavelength used in this spectroscopy technique. A UV-vis spectrophotometer typically consists of a light source that emits a broad spectrum of light ranging from the UV to visible wavelengths, as shown in Figure 3.4. This broadband light source is incident upon a monochromator that selects individual wavelength of light, one at a time, and illuminates it on the target sample. A detector was utilized to measure the intensity of the transmitted or absorbed light after it passes through the sample. By doing this, the wavelengths at which the material exhibit linear absorption can be determined experimentally. The absorption spectrum of a material will provide useful information including the absorbance, transmittance, absorption edge, and the bandgap of the material in the wavelength ranges from ultraviolet to visible light.

# 3.5 Soda Lime Glass Waveguide Writing

The primary objective of this study is to fabricate straight channel waveguide within the bulk soda-lime glass by inducing positive index change in the material. This is achieved by tightly focusing an intense femtosecond laser into the material, inducing localized modification through multiphoton ionization. The creation of the straight channel waveguide structure involves moving the glass sample in a linear path across the laser focal spot. Throughout the laser writing process, systematic adjustments were made to pulse energy and translational speed to investigate their effects on the laser-induced modification.

To achieve this, several crucial components are necessary in the experimental setup. These include a femtosecond laser source for nonlinear absorption excitation, an objective lens for focusing the laser beam into the medium, and a one-axis motorized linear translational stage for the fabrication of straight channel waveguides. Detailed

information on the experimental setup employed in this study is provided in Section 3.4.1. Additionally, specifics information regarding the characteristics and the preparation for the glass utilized in this research are detailed in the subsequent section.

# 3.5.1 Experimental setup

This section outlines the methodology employed in the soda-lime glass writing experiment conducted in Chapter 4. The experimental setup is illustrated in Figure 3.5. The laser source utilized was the OneFive Origami XP femtosecond laser, featuring adjustable pulse repetition rate ranging from 1 kHz to 1 MHz via the dedicated computer software. The pulse energy varies with the repetition rate, reaching a maximum of 40  $\mu$ J at 100 kHz and 4  $\mu$ J at 1 MHz. To ensure an optimal range of pulse energy for nonlinear absorption in the experiment, the laser system was set to operate at 100 kHz with a wavelength of 515 nm for this study. Due to the high pulse energy employed, the entire laser writing system was enclosed within a black box throughout the laser writing process to prevent any potential hazard to individuals in the laboratory.

The output laser beam passes through a set of plano-convex lens, where the beam size is expanded to overfill the objective lens aperture. A dichroic mirror was placed before the objective lens to serve two purposes: (1) to transmit the incident laser beam towards the objective lens and focused onto the sample; and (2) to reflect the laser beam that was back-reflected from the sample towards a CCD camera to have an in-situ visualization for the focused laser beam and the on-going process on the sample. A microscope objective (40x, 0.65 NA) was used to focus the laser beam on the sample. The calculated focused spot diameter in free space was ~1  $\mu$ m, according to the equation  $D = 1.22 \lambda/NA$ , where  $\lambda$  denotes the wavelength of the laser in free space. The sample was mounted horizontally on a high precision motorized 3-axis translational stage (Vexta), controlled

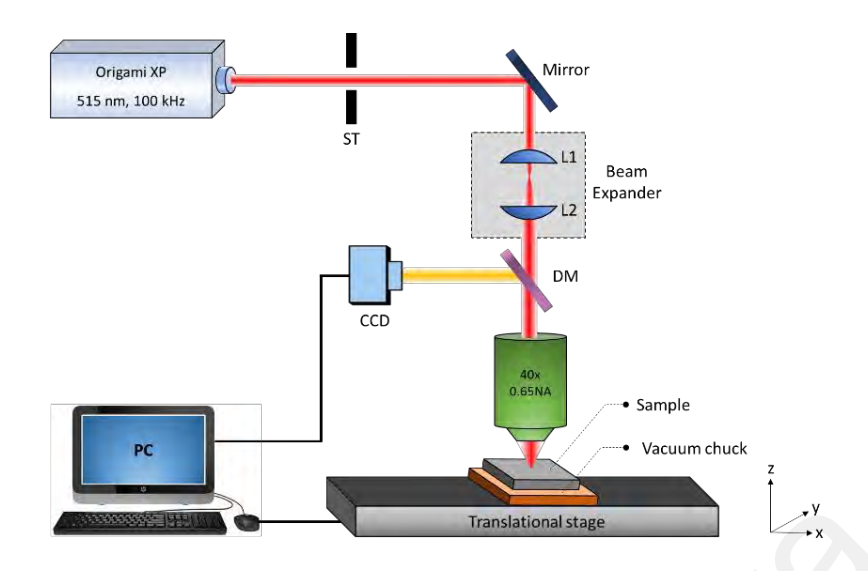


Figure 3.5. Schematic diagram of the glass writing system. ST: Shutter; L1&L2: Spherical lens 1 and 2.

with a stepping motor controller (Suruga Seiki D220) in conjunction with a self-coded Labview program. The traveling range of all axes is 30 mm with a resolution of 1 µm/step and a maximum translation speed of 10 mm/s. The laser focusing depth was adjusted by moving the z-axis stage, whereas waveguide writing direction was controlled using the XY stages. In order to ensure the steadiness of the sample, a vacuum chuck coupled to a vacuum pump system was mounted on the XY stages as the sample holder. Prior to the waveguide writing process, the sample was aligned perpendicularly to the incident laser beam path with the aid of a CCD camera, ensuring that the focusing depth across the sample is the same throughout the writing process.

The maximum pulse energy of the writing system was measured using an optical power meter placed after the objective lens. The optical system exhibits a 7.8 dB optical loss, reducing the initial maximum pulse energy of 40  $\mu$ J at the output of the laser head to 6.6  $\mu$ J after the objective lens. The relatively high optical loss in the system was attributed to the use of multiple optics for guiding laser light towards the writing stage.

In addition, approximately 20-30% of the light was obstructed by the objective lens aperture to ensure that the aperture was overfilled for maximum focusing NA. However,

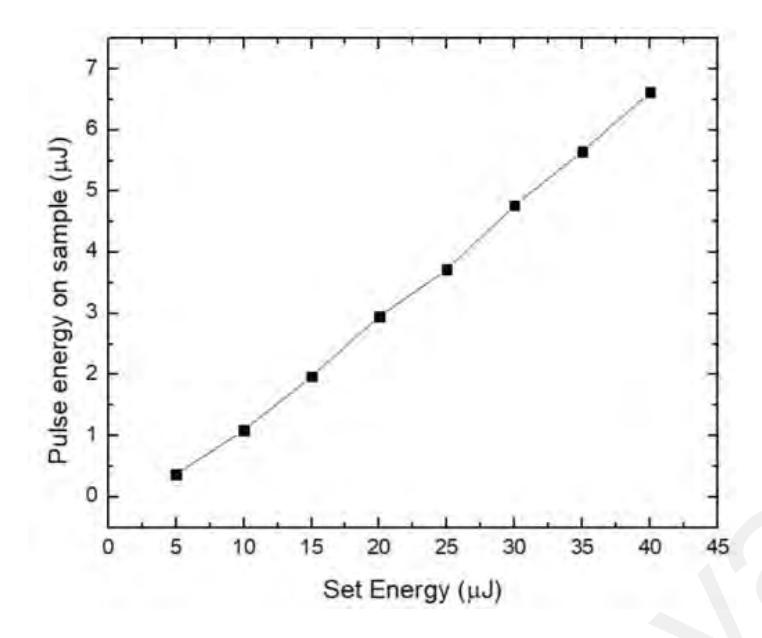


Figure 3.6. Laser pulse energy calibration. Set energy is the pulse energy coming out from the laser head, whereas the pulse energy on the sample was measured in the position between the objective lens and the glass sample.

since the remaining pulse energy was still higher than 1  $\mu$ J, it remains sufficient for this work. It should be noted that it is extremely important to measure the pulse energy after passing through the objective lens to provide a more accurate description of the laser parameters used for laser processing in the material. To achieve this, the pulse energy measurement after the objective lens was measured while systematically varying the actual pulse energy emitted from the laser head. This calibration established a precise relationship between the pulse energy at both ends, as depicted in Figure 3.6. Consequently, with this dataset, the pulse energy at the sample surface can be estimated based on the pulse energy emitted by the laser head.

#### 3.6 Femtosecond Laser Ablation On CR-39

This study delves into the interaction between femtosecond laser pulses and thermoset plastics (CR-39). Thermoset plastics are known to undergo irreversible curing when exposed to elevated temperatures. Since melting and reshaping were the common

mechanism for continuous material modification and waveguide fabrication, it is interesting to investigate the effects of thermal induced curing in DLW process. In this investigation, the impact of high repetition rate femtosecond laser pulses incident on the thermoset plastic was observed, specifically focusing on the laser-induced heat accumulation effects. The DLW process was similar to the glass writing material, which involves the scanning of an intense femtosecond laser through the bulk material at varying speeds. However, modifications at different focusing depths were concurrently compared to explore their implications for the modified structure. With that, the experiment was divided into two parts: bulk modification and surface ablation.

# 3.6.1 Experimental Setup

Similar to DLW writing in glass, the experimental setup for this study involves a femtosecond laser light source, an objective lens for laser light focusing, and a translational stage for the sample motion. However, a nitrogen purging system was added to the system for the surface ablation experiment where the gas purging direction is indicated with an arrow in Figure 3.7, in which the application of the system can be found in Chapter 5. The characteristics and preparation method for the CR-39 thermoset plastic used in this work are provided in Section 3.5.2.

The laser processing of CR-39 sheets was carried out with an 800 nm Ti:Sapphire femtosecond laser oscillator that generates 120 fs pulses at a high repetition rate of 80 MHz. The maximum pulse energy of the laser system was determined through average power measurements, which is found to be approximately 9 nJ per pulse. To control the pulse energy, a homemade variable attenuator consisting of a half-wave plate and a polarizing beam splitter was placed in front of the output of the laser head. Subsequently, the laser beam was focused onto the sample using a long working distance 20x objective

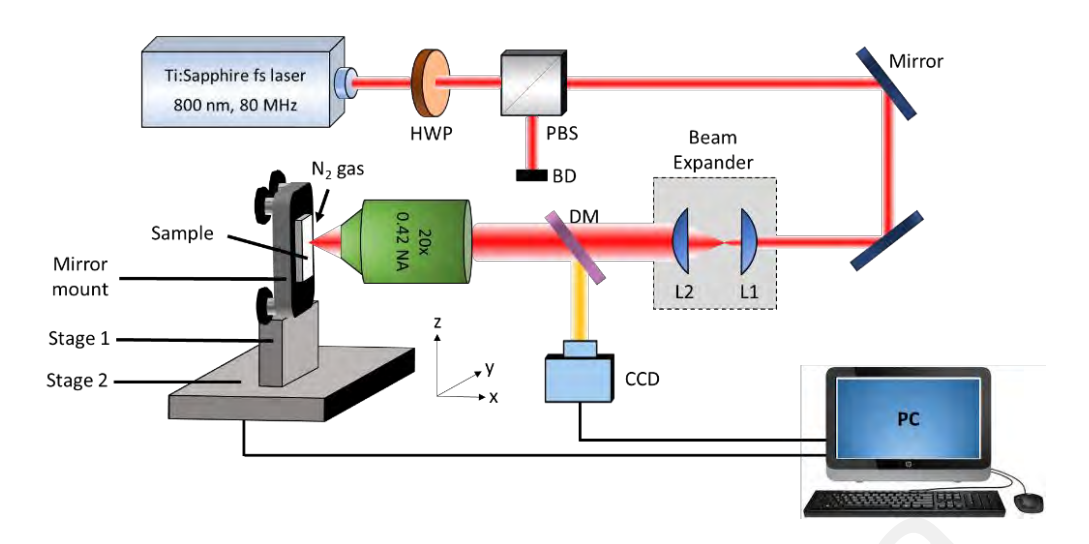


Figure 3.7. Schematic diagram of the surface ablation system. HWP: Half-wave plate; PBS: Polarizing beam splitter; BD: Beam dump; L1&L2: Plano-convex lens 1 and 2; Stage 1: XZ micrometer stage; Stage 2: LTS300 translational stage.

lens (Mitutoyo) with a numerical aperture (NA) of 0.42. To ensure a diffraction-limited focus, the beam size was expanded to approximately 0.7 cm with a set of plano-convex lenses to fully fill the aperture of the objective lens. The focused beam diameter, D, was calculated to be approximately 2  $\mu$ m in free space. The number of laser pulses applied to each spot on the sample was regulated by varying the sample's translation speed based on  $N = 2\omega_0 R/v$ , where N indicates the number of pulses irradiated per spot,  $\omega_0$  is spot radius, R denotes laser repetition rate, and v is the translation speed.

To achieve the precise sample positioning, multiple stages were required in the setup. One of these stages is a two-axis linear translational stage (Newport), referred to as "Stage 1". This stage allows later adjustments of the sample's position in both the X- and Z-directions. Additionally, a motorized linear translational stage (Thorlabs LTS 300/M) denoted as "Stage 2" was employed for controlling the sample's motion in the Y-direction. The travel range of this stage is 300 mm with a minimum movement increment of 0.1 µm, and the maximum translational speed is 50 mm/s. This motorized stage is also responsible for the sample movement for the line ablation experiment. The combination of these two stages allows for comprehensive translation of the sample in all three spatial

dimensions. The sample position was adjusted to be perpendicular to the incoming laser beam by observing the back-reflected beam from the sample surface in conjunction with a CCD camera (Amscope MD310B-BS). By adjusting the angle of the mirror mount, the angular position of the sample was precisely adjusted to the optical axis of the incident laser, making it possible to maintain a consistent focal plane of the laser beam across the entire sample during the laser processing.

In addition to the laser source and translational stage, a nitrogen gas purging system was introduced into the setup with its nozzle directed to the sample surface, providing a steady flow of nitrogen gas to the sample surface. This is to minimize the surface contamination due to the plume produced during the ablation process. The generated plume can also hinder the laser ablation process, which the details will be explained in Chapter 5.

# 3.7 SU-8 Waveguide Fabrication

The ultimate goal for this work is to fabricate a 3D standing waveguide in SU-8 photoresist. To do this, the experiment was divided into few parts. First part of the experiment involves planar waveguide writing, where multiple straight channel waveguide was fabricated at varying laser fluence. The threshold fluence for polymerization and the damage threshold was obtained at this part of the experiment. Subsequently, a 50:50 directional coupler was fabricated as the second part of the experiment, based on the optimized laser processing parameters obtained. Finally, a 3D standing waveguide was produced.

The foundation of the experimental setup for this work was based on the glass writing setup presented in Section 3.4, but the laser source was replaced with the 780 nm Ti:Sapphire femtosecond laser. To adapt to the laser wavelength, the optics used (mirrors, lens) were also replaced with the designated optics at this wavelength to prevent optical

loss. Another notable difference is the addition of motorized 3-axis translational stage, to facilitate the 3D DLW.

## 3.7.1 Experimental setup

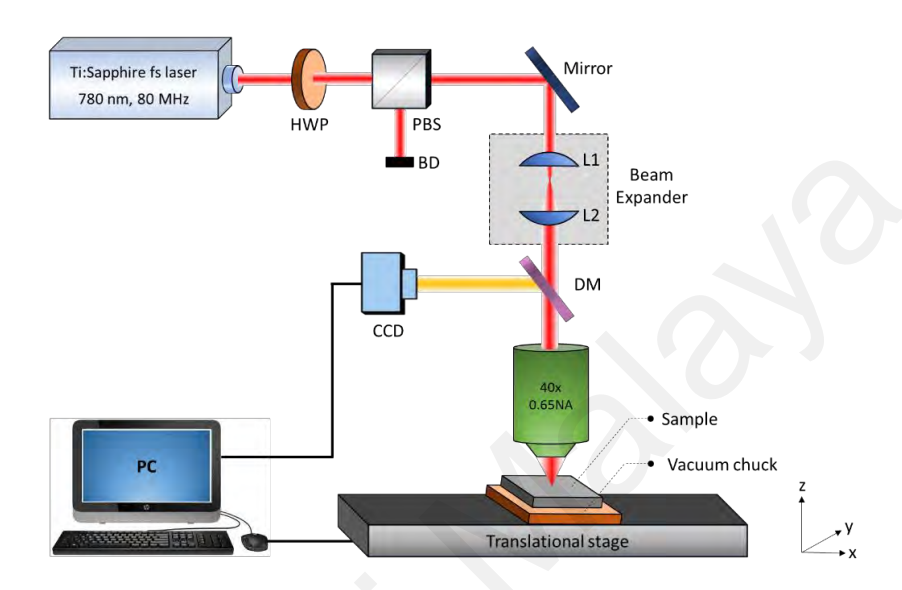


Figure 3.8. Sketch of the experimental setup for SU-8 waveguide writing.

The SU-8 waveguide fabrication was performed using DLW technique via the 2PP process. A Ti:Sapphire femtosecond laser operated at 780 nm was employed, delivering 270 fs pulse duration at 80 MHz repetition rate was employed for the fabrication process, as shown in Figure 3.8. The laser system could provide femtosecond pulsed up to 1 W, when the pumped laser (Millenia 632 nm CW laser) was set to 6 W. Precise control of the laser power was achieved with a home-made optical attenuator, consisting of a half-wave plate and Glan-Taylor polarizer. The femtosecond laser beam was focused onto the spin-coated SU-8 film using a 20x long working distance objective lens (Mitutoyo, 0.42 NA). The focus spot diameter in free space is approximately 2.2 µm. Sample alignment was done with the assistance of the CCD camera, by observing the back-reflected image from the sample surface. To avoid photopolymerization of the SU-8 resist during the alignment, it is crucial to operate the laser at low power CW-laser power mode. It is also important

to consider the edge beading effects, where a larger volume of SU-8 accumulates at the edge of the substrate, causing the film to become thicker than the desired thickness. Edge beading is a common phenomenon during spin coating of SU-8 on the silicon wafer even at the industrial level, however, the effect is more pronounced in this case because the size of the substrate is much smaller (Figure 3.9 (b)). Therefore, the laser writing area should avoid the edges of the substrate and be limited to the central area of the substrate only.

The SU-8 waveguide fabrication experiment comprises of 2 parts: 2D waveguide and directional coupler fabrication, and 3D bridge waveguide writing. For the 2D waveguide writing, the translational stage used is the Newmark 2-axis translational stage (NLE series), which is computer controlled with the Galil tools software and programmed with DMC programming language. The maximum travelling range of this stage is 300 mm with a resolution of 0.1 µm, whereas the maximum travelling speed is 50 mm/second. For the 3D waveguide writing, the high precision motorized 3-axis translational stage (Vexta) was employed to allow synchronized movement for the 3D motion, programmed with the self-written Labview program. The vacuum sample holder was included in both 2D, and 3D waveguide writing to ensure the sample stayed intact at its position.

Waveguide structure was created by translating the substrate through a pre-defined motion using a computer-controlled 2-axis translational stage (Newmark). In the experiment, multiple straight waveguides were fabricated at different combinations of laser power and scan speed to determine the optimal processing parameters for single-mode waveguide fabrication. The laser power varied from 80 mW to 180 mW, while the sample scanning speed ranged from 2 to 10 mm/s. Each waveguide was positioned 100 µm away to avoid overlapping with the neighboring waveguides.

After completing the waveguide writing process, the exposed sample undergoes a post exposure bake (PEB) to finalize the cross-linking reaction. Similar to the soft-baking

process, the PEB starts with a pre-bake at 65°C for 2 minutes, followed by a subsequent bake at 95°C for 10 minutes. This step is of utmost importance as it significantly enhances the solubility contrast between the exposed and unexposed areas of the photoresist. In the case of SU-8, during PEB, the exposed areas undergo cross-linking, making them less soluble in the developer solution, while the unexposed regions retain their solubility. In the chemical development step, the unexposed regions are selectively removed from the substrate, leaving behind the exposed regions as the patterned waveguide. The substrate is immersed in the chemical developer solution for 10 seconds to completely remove the unexposed regions. After the chemical development process, the sample will be rinsed with the isopropyl alcohol (IPA). If a white-colored solution is observed on the surface during this process, it indicates that the same has not been fully developed. In such cases, the sample is immersed in the developer for an additional 30 seconds. This process is repeated until the substrate shows a clear and clean surface after rinsing with the IPA. Finally the waveguide chip is subjected to a hard bake at 150°C for 30 mins to complete the fabrication process. The hard bake helps to further stabilize and solidify the patterned waveguide, ensuring its durability for the waveguide application. The edge of the waveguide chips was carefully diced with a diamond cutter, to remove the edge

# 3.8 Sample Preparation

To achieve successful outcomes in laser micromachining, the preparation of the sample is of paramount importance. Proper sample preparation ensures the effective interaction between the laser beam and the material, leading to improved accuracy, quality, and reproducibility of the micromachining process. Three crucial steps in sample preparation for laser micromachining are dicing, cleaning, and polishing. Each step plays a vital role in ensuring the dimensional accuracy, removing the surface contaminants, and optimizing

the sample's surface quality, which directly impacts the overall performance and reliability of the final product.

Dicing involves the precise cutting of the sample into smaller individual pieces. This step is especially crucial when dealing with large samples or removing unwanted areas from the sample. By dividing the sample into smaller, manageable pieces, the laser micromachining process becomes more controllable, and the potential for waste is minimized, contributing to cost-effectiveness. Next, the cleanliness of the sample surface significantly impacts the outcome of laser micromachining. Even minute traces of contaminants, such as dust, oil stains or residues, can interfere with the laser-material interaction, leading to irregularities, defects, or reduced material processing precision. Cleaning the sample thoroughly ensures the removal of any surface contaminants and creates an ideal environment for the laser to interact directly with the material, maintaining the desired dimensional accuracy and surface integrity throughout the micromachining process. Lastly, polishing the sample surface is essential to obtain a smooth and flat surface with reduced roughness and defects. Uneven or rough surfaces can lead to scattering of the light beam, affecting the observation of the sample quality under an optical microscope. By carefully polishing the sample, any irregularities and impurities on the surface can be removed, enabling a better view on the sample surface for data analysis.

#### 3.8.1 Soda Lime Glass

The glass sample used in this study is the commonly available soda lime glass (Sailing boat, China). It came in with a dimensions of 75 mm x 26 mm x 1 mm, which is mainly for the application as the microscope glass slide. Prior to the experiment, the glass slide is carefully diced into two different pieces with a slicing machine (Ultraslice compact),

each with a length of 30 - 40 mm. Distilled water was rinsing the sample surface throughout the dicing process to remove the debris, as well as to cool down the dicing saw. After the sample is diced, the sample surface will undergo an additional cleaning process to remove the invisible contaminant remaining on the surface. Cleaning of the glass sample will follow the standard procedure, starting by rinsing the sample with deionized water, followed by acetone and isopropyl alcohol (IPA), and finally rinsing with deionized water again. The remaining liquid/droplets on the surface will be air blown with a rubber air blower and the sample is ready for the laser writing process. Once the laser writing process is completed, the edges of the sample will be diced once again to remove the damage area at the cross-section of the sample. Removing the damaged surface is a crucial step to reveal the structure of the underlying modified region. The diced sample typically has a rough surface, therefore polishing the cross-section of the diced surface is necessary to have a better view of the cross-section. Polishing the sample will also minimize the light scattering of the coupling facets, thereby enhancing the coupling efficiency and the performance of the waveguide. Polishing the glass sample involves the use of the diamond lapping film of different grit sizes. In this case, the grit size of the polishing film used from coarse to fine is 30, 15, 5, 1 and 0.5 microns respectively.

#### 3.8.2 CR-39

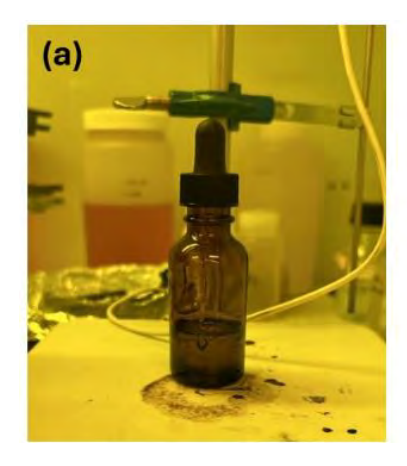
The CR-39 was cut into smaller pieces of 20 mm by 20 mm with a pair of scissors from the bulk for experimental use. The debris or dust particles on the surface from cutting were blown away with a rubber air blower to prevent scratches during the subsequent cleaning process, and also to avoid burning of the particles that might introduce unwanted burning or damage to the sample during the laser writing process. As CR-39 will dissolve in most chemical solutions, especially acetone, the sample surface was cleaned by simply wiping the surface with deionized water using a lens tissue. The cross-section of the

sample was polished with the same technique stated in Section 3.4.2. to investigate the structure from its cross-section.

#### 3.8.3 SU-8

The preparation of the SU-8 samples adhered to the standard SU-8 processing protocol, with the exception that the DLW was used instead of photolithography. SU-8 resist was usually stored in a tightly sealed container in a cool refrigerator (Figure 3.9 (a)), shielded from direct sunlight. This is to extent the resist's shelf life and to prevent any undesirable chemical reactions induced by UV light exposure. Storing SU-8 in a designated yellow room within a cleanroom environment served for additional protection to the resist. To avoid contaminating the resist, a small quantity was dispensed into another small glass container for experimental use and refilled from the main container as needed. It's worth noting that the viscosity of SU-8 depends on temperature i.e. high viscosity when its temperature is low, and lower viscosity when the temperature increases. Therefore, to ensure consistent viscosity, SU-8 removed from the refrigerator was allowed to equilibrate to room temperature over a period of 2 hours inside the yellow room. Two types of SU-8 were utilized in this study: SU-8 2002 was employed for 2D planar waveguide fabrication, while SU-8 2010 was chosen for 3D waveguide fabrication. SU-8 2002 possesses lower viscosity than SU-8 2010, producing thin films with a maximum thickness of 3 µm, an ideal thickness for a planar waveguide. In contrast, SU-8 2010 was able to produce a thicker film up to 20 µm, enabling the creation of larger 3D structures.

The substrate used in this experiment was a p-type <111> silicon wafer with 5  $\mu$ m silicon oxide layer. The wafer is typically polished on one side, while remains dull on the other side. The dicing of the silicon wafer can be done by placing the dull side on a soft surface and locate the orientation of the primary flat. Then, the primary flat or the edge



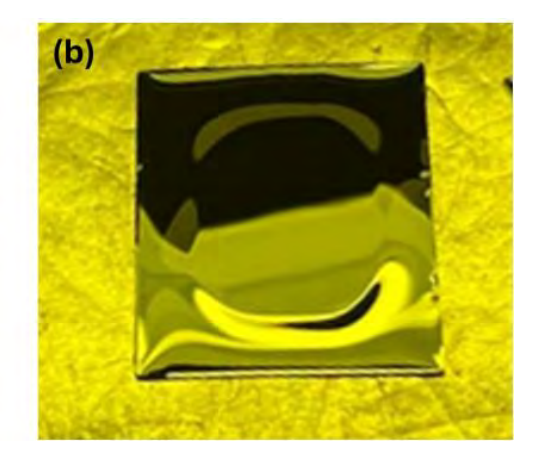


Figure 3.9. (a) SU-8 stored in a glass container, (b) spin-coated SU-8 with edge beading effect.

90 degrees from the primary flat is scribed using a diamond cutter to create a dent. By applying a slight pressure on both sides of the dent, a clean line cut along the wafer can be achieved. These steps are repeated to dice the wafer into smaller pieces with the desired dimensions. A single wafer can be diced into about 10 pieces of square substrate with a size of approximately 25 mm by 25 mm. Each of the silicon pieces will then be rinsed with the deionized water, IPA, and acetone, to remove any surface contaminants introduced during the dicing process. After that, the SU-8 photoresist will be spin coated on the substrate for waveguide fabrication. Once the laser writing process is completed, the wafer is diced once again to reveal the cross-sectional structure of the waveguide. Polishing is not needed in this case as the waveguide material is the photoresist and not the silicon wafer, and polishing the polymer waveguide might cause irreversible damage to the waveguide.

Spin coating with static dispense technique will be employed for coating SU-8 on the silicon substrate. About 1 ml of resist was dispensed on the surface of the substrate with a pipette. It is beneficial to dispense excessive resist on the substrate at this stage that is more than the amount required in the final coating thickness. This is to ensure a complete coverage of the substrate surface at the end of the coating. It is also important to remove

any bubbles formed on the substrate while dispensing the solution to ensure a smooth coating.

After dispensing the resist onto the substrate, the substrate is accelerated by the spin coater, reaching a high rotational speed of few thousand rounds per minute (rpm). During this rotational motion, the photoresist is allowed to spread uniformly across the substrate, enhancing its adhesion to the surface. Excess photoresist will be expulsed from the substrate due to the rotational motion, subsequently thinning down the film to achieve the desired thickness. The choice of spin speed is adjusted based on the viscosity of the material and the target final thickness depends on the application. For instance, the SU-8 2002 used in this work was spun at 3000 rpm to achieve a thin film with a maximum thickness of 2  $\mu$ m. In contrast, SU-8 2010 was spun at 2000 rpm to produce a thicker film of 20  $\mu$ m. The selection of spin speed is crucial to achieving the desired film characteristics, and it should be tailored to the specific material and application requirements.

The SU-8 films subsequently soft-baked after it has been coated to the surface of the silicon wafer. SU-8 is typically dissolved in a solvent to achieve the desired viscosity during the coating. Soft baking helps to remove most of the solvent, ensuring the remaining photo resist left on the wafer surface is in its solid form. As the solvent evaporates, the photo resist can also form a better physical and chemical bond with the substrate surface, thereby enhanced the surface adhesion. To prevent the introduction of thermal stress to the photo resist due to the drastic temperature changed, pre-baked is carried out at 65°C for 2 minutes, and subsequently ramped up to 95°C to soft-baked the photo resist for 10 minutes. It is notably that oven is generally avoided for soft-baking SU-8 due to their uncontrolled temperature distribution within the large volume of the oven. While soft-baking temperature will significantly affect the quality of the

photopolymerization, hotplate is often recommended for soft-baking as they provide better temperature control at the substrate level.

## 3.9 Waveguide Characterization Techniques

Waveguide characterization is an important and crucial step in any waveguide design and fabrication. It is necessary to evaluate the quality of the fabricated waveguide to confirm that it meets the requirements for a particular application. Understanding the evolution of the waveguide characteristics under various fabrication conditions also provides fundamental information for modification and optimization of the waveguide design and fabrication, improving the performance of the fabricated waveguide. There are several key characteristics used to evaluate a waveguide which include the physical characterization and optical characterization. For physical characterization, optical microscope, FESEM, and surface profiler were utilized to access the physical properties of the sample such as the surface morphology, surface roughness, shape, and size of the sample. Whereas optical characterization includes the measurement of the optical loss, index changed, waveguide shape and size, etc. Experimental evaluation methods will be provided alongside the theoretical estimations.

#### 3.9.1 Optical Microscope

All the samples were examined under an optical microscope (ZEISS) once the fabrication process is completed. The microscope was equipped with multiple objective lenses with different magnification i.e. 4x, 20x, 50x, and 100x. Top-light illumination will be employed for the investigation of the top view of the fabricated structure (Figure 3.10), whereas bottom light illumination will be utilized for cross-sectional structures examination (Figure 3.11). Depending on the aim of the investigation, bottom light

illumination with opened or closed aperture will be applied accordingly to obtain the desired image of the sample. For instance, open aperture was employed to access the surface morphology of the sample such as the shape and size of the sample, whereas close aperture will be applied to identify the light guiding region. The microscope is connected to a CCD camera that feeds real-time images into the computer using an imaging software (TS View). The software also provides a measurement feature that helps measure the dimensions of the fabricated structure.

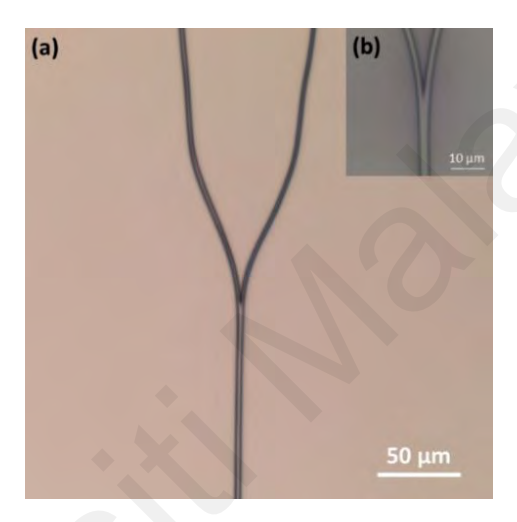


Figure 3.10. (a) Top view of a SU-8 directional coupler captured under the optical microscope with a 10x objective lens. (b) Inset: same directional coupler captured with a 100x objective lens.

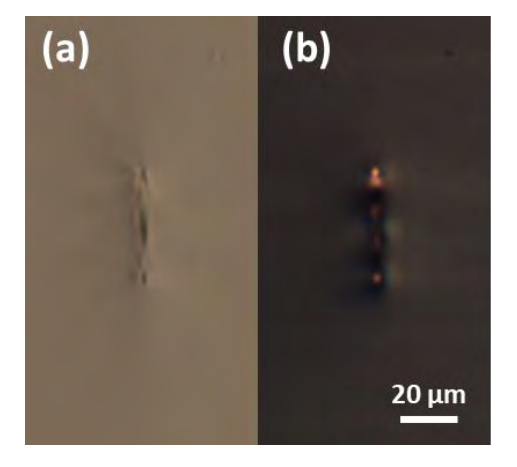


Figure 3.11. Cross-sectional image of soda lime glass waveguide captured under 10x objective lens using (a) top illumination, and (b) bottom illumination.

#### **3.9.2 FESEM**

Field Emission Scanning Electron Microscopy (FESEM) is an advanced imaging technique used in materials science, nanotechnology, and various other scientific disciplines. It works by emitting electrons through a process known as field emission. The emitted electrons are then focused into a fine beam and directed towards the sample. When the electron beam interacts with the sample, it can create a variety of signals, including secondary electrons, backscattered electrons, and characteristics X-rays. These signals are detected and used to create the high-resolution images of the sample surface, as illustrated in Figure 3.12. The FEI Quanta 400F FESEM has a minimum resolution of 3 nm and up to 250,000x magnification, was used in the study to capture high resolution images of the fabricated microstructures. The accelerating voltage was set to 10.0 kV with a magnification factor of 20,000x for most cases, to produce a sharp image of the fabricated structure with ultra-fine details.

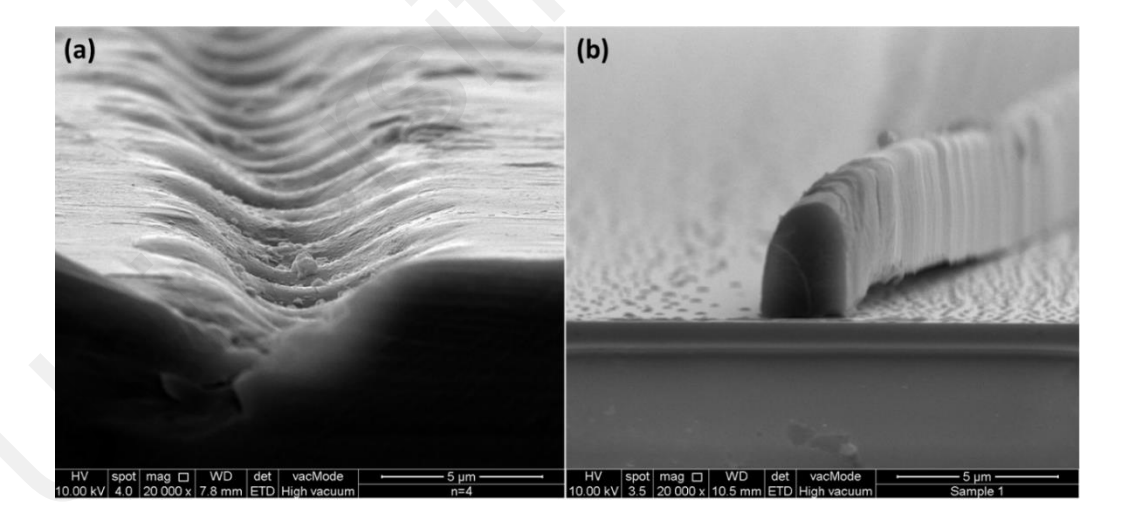


Figure 3.12. Example of FESEM images for (a) CR-39 surface ablation, and (b) SU-8 waveguide.

#### 3.9.3 Surface Profilometer

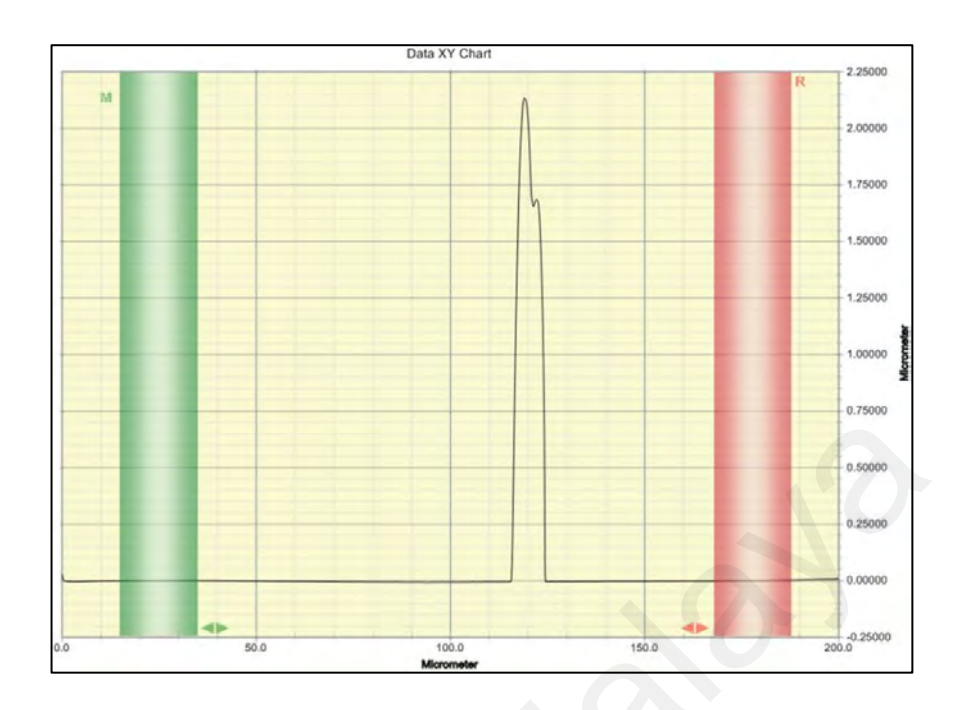


Figure 3.13. SU-8 waveguide heigh measurement using Dektak 150.

Surface profilometer is a tool typically used to measure the step height, surface roughness, and waviness of the surface of a material or structure. A diamond-tipped stylus will be moving laterally across the sample surface while in contact and measure the deflection of the stylus. Dektak 150 has a high vertical resolution of 1 Å with a selective stylus force ranging from 0.03 mg to 15 mg, allowing its flexibility to measure various sample surfaces without inducing irreversible damage to the sample surface. Figure 3.13 shows the example measurement of using the Dektak to measure the depth of the ablated trenches in CR-39 and the dimensions of the SU-8 waveguide.

#### 3.9.4 Insertion Loss

Insertion loss is the measurement of the power loss as light transmits through an optical device, i.e. an optical waveguide. Insertion loss includes both coupling loss and propagation loss. It is commonly expressed in decibels (dB) and is calculated as the ratio of the output power to the input power. To measure the insertion loss of a waveguide, the

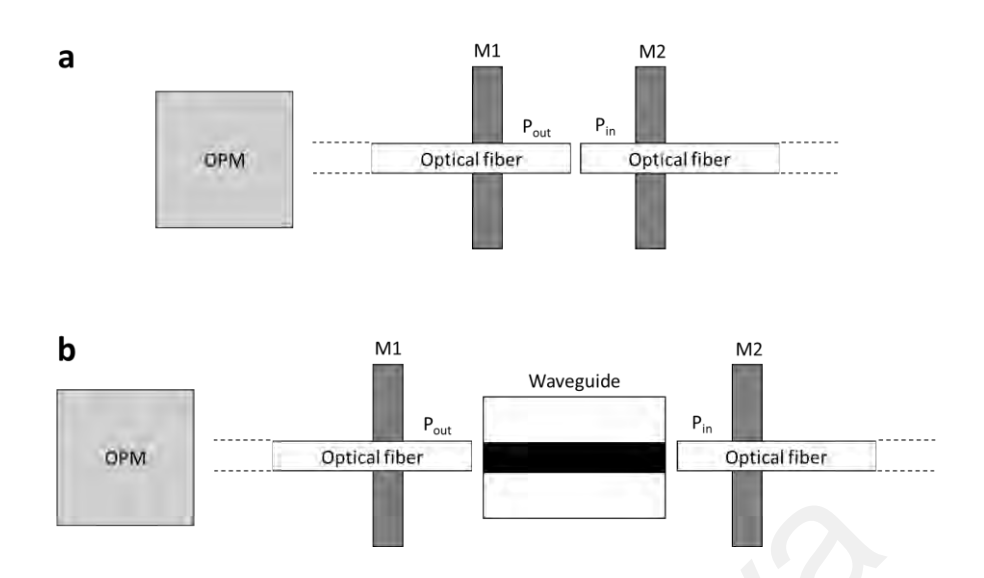


Figure 3.14. (a) Calibration of the measurement setup and (b) waveguide insertion loss measurement.

optical power levels at the input and output of the waveguide are measured using an optical power meter. Figure 3.14 shows the experimental setup to measure the insertion loss of an optical waveguide. The measurement setup typically consists of a stable laser source that emits laser at the wavelength of interest, and an optical power that measures the light's power level. Light coupling can be achieved with optical fiber positioned at the input and output of the waveguide. Both coupling fibers are mounted on a 3-axis linear translational stage to allow adjustment of the orientation of the couplers with respect to the waveguide input/output facets. Therefore, accuracy of the alignment stage plays an important role in obtaining an accurate measurement. In this case, an XYZ linear translational stage (Newport) with 0.05 μm resolution was used.

It is important to calibrate the measurement setup to establish a baseline reference power before measuring the insertion loss of the waveguide. First, laser will be coupled from the input coupling fiber directly into the output coupling fiber without the waveguide. The power level will then be recorded with an optical power meter, as shown in Figure 3.14 (a). This measured power is the baseline reference power that represents the intrinsic loss of the entire measurement setup. After that, waveguide will be inserted in between

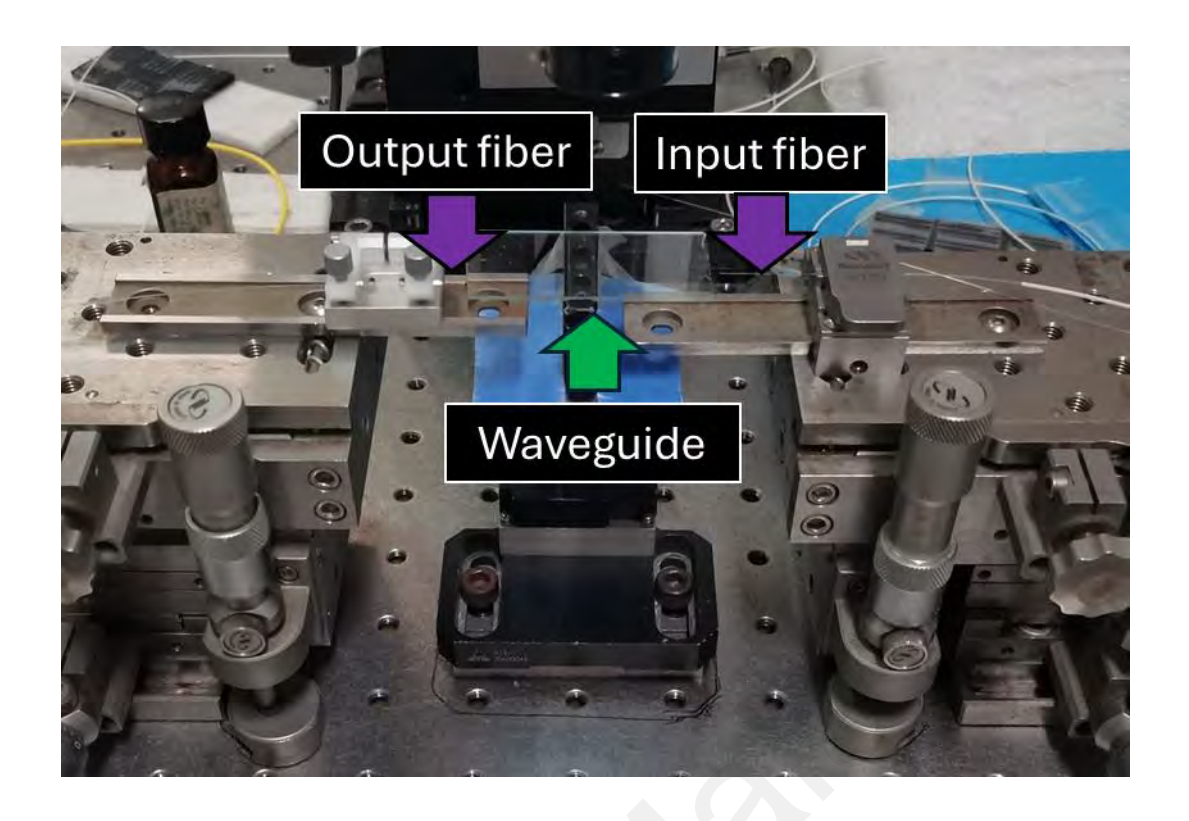


Figure 3.15. Optical loss measurement setup.

the coupling fibers, which will then be realigned to the waveguide input/output facets, as shown in Figure 3.14 (b). The output power with the waveguide inserted is measured once again. By calculating the difference of the power with and without the waveguide, the insertion loss for the waveguide can then be calculated as follow,

$$Loss (dB) = -10 \log_{10} \frac{P_{out}(W)}{P_{in}(W)}$$
 (3.1)

where  $P_{out}$  and  $P_{in}$  are the optical power measured with and without the waveguide, respectively. It should be noted that in addition to optical fiber, objective lenses with suitable numerical aperture can also be used for light coupling into and out of the waveguide.

Insertion loss is an important parameter in optical systems, as it can have a significant effect on the optical system. High insertion loss can result in reduced signal strength, increased noise, and reduced system sensitivity. In applications such as

telecommunications, where optical signals may need to travel long distances through multiple components, minimizing insertion loss is crucial for maintaining the signal strength. Whereas for applications such as waveguide sensor, insertion loss might also lead to reduced sensitivity of the waveguide. Hence, understanding the cause of the insertion loss for a waveguide is crucial in optimizing the quality of the fabricated waveguide.

### 3.9.5 Coupling Loss

Coupling loss is one of the main factors of insertion loss of an optical waveguide. It occurs at the interface between the coupling fiber and the optical waveguide. The loss is usually caused by the mismatch between the optical waveguide and the input/output fiber, including numerical aperture (NA) mismatch, mode field diameter (MFD) mismatch, imperfect waveguide alignment, and defects or contaminations at the waveguide end facet. The latter two factors can be avoided by giving careful attention during waveguide fabrication and preparation processes. However, theoretical calculations are necessary for the mismatch losses as these characteristics are rather difficult to determine experimentally. Understanding these factors is an important step to optimize the waveguide coupling and prevent power loss.

NA of an optical fiber or any optical component is a measure of its angular acceptance of light, or the range of angles of light that can be coupled into that optical component. Mathematical description of NA of a component is defined as the product of the refractive index of the receiving optics and the sine of the maximum angle against the optical axis, for which light can be transmitted throughout the system at minimum propagation loss,  $NA = n_0 \sin \theta_{max}$ . The NA mismatch loss occurs only when the light emitter has higher NA than the light receiver. Take example for the light coupling from optical fiber into an

optical waveguide, there will be a NA mismatch loss if the NA of the input fiber is higher than the NA of the waveguide. In this case, optical loss occurs as some of the light is not coupled into the waveguide or loss to the surrounding as it propagates towards the waveguide. The magnitude of the NA mismatch losses can be mathematically determined by the equation:

$$Loss_{NA}(dB) = \begin{cases} -10\log_{10}\left(\frac{NA_2}{NA_1}\right)^2, NA_2 < NA_1\\ 0, NA_2 > NA_1 \end{cases}$$
(3.2)

Similar to the NA mismatch, MFDs for both the emitter and receiver must be matched as well as possible to avoid power loss during the light coupling process. Conventionally, MFD mismatch measurement was performed using an optical time domain reflectometer (OTDR) However, this method is only applicable for a fusion spliced optical fiber, and not suitable when the light is coupled from optical fiber to a waveguide. Hence, theoretical approximation is required for the MFD measurement when light is coupled between fiber and a waveguide. MFD is the measurement of the beam size where the intensity falls to  $1/e^2$  of the laser peak intensity.

The size of the MFD is dependent on the waveguide core diameter, laser wavelengths, and the numerical aperture of the waveguide, which can be approximated using the following the equation:

$$MFD = 2a \left( 0.65 + \frac{1.619}{V^{\frac{3}{2}}} + \frac{2.879}{V^{6}} \right), \tag{3.3}$$

$$V = \frac{2\pi a}{\lambda} NA,\tag{3.4}$$

where a is the core radius of the waveguide.

It is important to note that Eq (3.3) is intended for the calculation of the MFD of a step index fiber where the core dimension is radially symmetrical. For laser written waveguide,

the structure is not the same as the optical fiber. Depending on the material and the application, ridge waveguide and buried waveguide structure are the most commonly found in direct laser writing. Ridge waveguide usually has a square or rectangular core sandwiched between cladding of various refractive index. Due to the non-symmetrical cladding index profile, ridge waveguide can support multiple modes and have mode profiles that are different from a Gaussian-like distribution, which the formula assumes. Therefore, Eq (3.3) is only a rough approximation of the MFD of ridge waveguide (Marcuse, 1977).

On the other hand, laser written buried waveguide is formed by inducing high index waveguiding core at the laser focus spot, surrounded by the unmodified material that has a relatively lower index which made up the cladding. The waveguiding core of laser written buried waveguide can have a complicated cross-sectional geometry, but it is often circular or elliptical shape, according to the shape of the voxel. This waveguide structure mimics the design of an optical fiber, and thus Eq (3.3) provides a more accurate approximation for the MFD of the buried waveguide. Justification has been made based on the data provided in several report (Dias et al., 2018; Shane M Eaton et al., 2011). For instance, the measured MFD for WG<sub>2</sub> written in borate glass (Dias et al., 2018) and fused silica (Shane M Eaton et al., 2011) was 11 µm and 7.1 x 7.4 µm, whereas approximation with the equation shows 11.5 µm and 7.3 µm respectively, showing a consistency of the calculated value with the experimental measurements.

It can be seen from the equation that MFD and NA are inversely proportional to each other. This means that if the MFD of the emitter is smaller than the receiver, the input light will not be fully captured by the receiver due to the larger cone angle of the emitting light. On the other hand, if the MFD of the emitter is larger than the receiver, the input light overfilled the core of the receiver, resulting in portion of the light scattered at the cladding area and lost to the surrounding. Therefore, it is extremely important to match

the MFD of both emitter and receiver as closely as possible to avoid any power loss. Though it is difficult to perfectly matched the MFD of different optical components, the mathematical expression can help address the degree of the mismatch losses:

$$Loss_{MFD} (dB) = -10 \log_{10} \frac{4}{\left(\frac{MFD_1}{MFD_2} + \frac{MFD_2}{MFD_1}\right)^2}$$
 (3.5)

where *MFD1* and *MFD2* refers to the measured MFD of the emitter and the receiver respectively.

#### 3.9.6 Propagation Loss

When light propagates in a waveguide, some of its optical power might be loss due to several factors including material absorption, defects scattering, bending loss, nonlinear frequency conversion, radiation loss, and mode conversion loss. Some of these factors come from the basic properties of the material and it is unavoidable, whereas there can be additional extrinsic losses due to poor quality of the waveguide fabrication and design. To sum up all the factors, the propagation loss of a waveguide can be obtained by simply using a cut-back method.

The cut-back method involves measuring the optical power at the output of a waveguide, and then cutting off a known length of the waveguide and then repeating the power measurement. By comparing the optical power for different lengths of the waveguide, the propagation loss per unit length (dB/cm) of the waveguide can be calculated. The cut-back method is useful for accurately measuring the optical loss in a waveguide as it considers all the aforementioned intrinsic loss in that particular waveguide. Though cut-back method can be time-consuming and destructive, it remains as a valuable tool in the characterization and optimization of a waveguide.

#### 3.9.7 Mode Field Diameter Measurement

To calculate the MFD mismatch between the optical fiber and the waveguide, the first attempt is to measure the MFD of both components. The optical fiber used in the work presented in this dissertation includes SMF-28, and UHNA4 fiber. Both fibers are conventionally available and thus, the MFD can be obtained from their respective data sheets. However, the waveguide was fabricated using direct laser writing techniques. Therefore, a sensible MFD measurement technique is necessary to obtain the MFD of the fabricated waveguide.

An attempt was made to measure the MFD of the waveguide with a near-field imaging approach. With this measurement technique, an objective lens is used, where the focusing plane of the lens is positioned at the waveguide output facet. The output facet image was focused onto an infrared (IR) camera for beam profile analysis, as shown in Step 1 of Figure 3.16. The image captured by the CCD camera is in unit pixel. Once the beam profile of the waveguide output is captured, the waveguide was removed, and the optical fiber was translated towards the objective lens until a sharp image of the beam profile at the fiber tip is observed on the IR camera, as shown in Step 2 of Figure 3.16. Since the MFD of the optical fiber was obtained from the data sheet, the captured beam size of the fiber on the IR camera can be used as a calibration tool to calibrate the IR camera, to convert the beam size in pixels into the micrometer scale. Then, by comparing the captured beam diameter of the optical fiber and the waveguide, the MFD of the waveguide output mode profile can be approximated. The major hurdle of this measurement technique is that it is extremely important to maintain the distance between the objective lens and the IR camera. A slight difference in the distance would affect the measurement accuracy. Therefore, extra care needs to be taken during the removal of waveguide and translation of the optical fiber. Despite the difficulty of the measurement technique, it is actually very simple with sufficient practice.

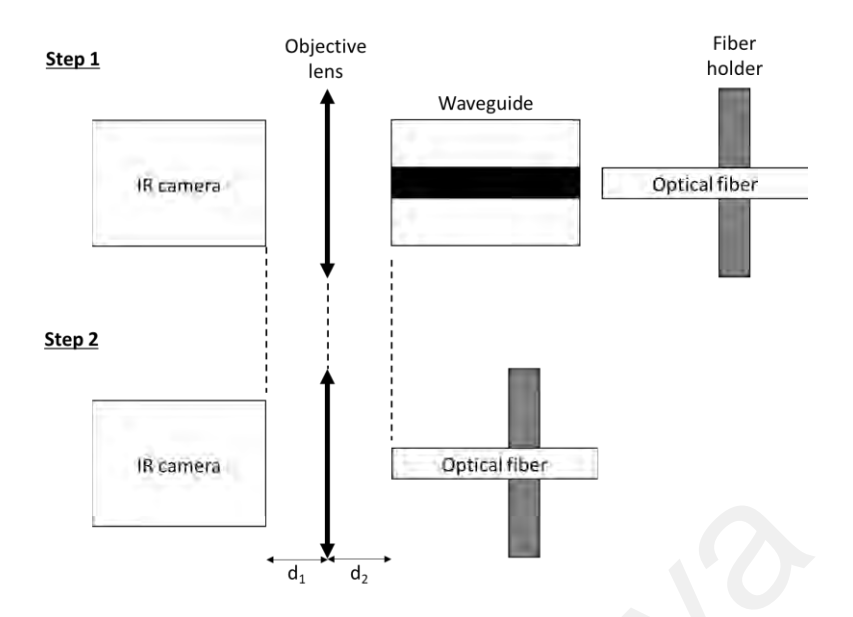


Figure 3.16. Illustration of the near field MFD measurement technique. Distance d<sub>1</sub> and d<sub>2</sub> were kept constant during the measurement period. The objective lens and IR camera remained static during the measurement, whereas the optical fiber was translating back and forth to obtain the calibration factor and as a light source for the waveguide loss measurements.

#### 3.9.8 Numerical Aperture Approximation

The numerical aperture of the fabricated waveguide was then approximated from using Equation (3.4). The diameter of the waveguide was measured under an optical microscope (Zeiss). The microscope was equipped with 4x, 10x, 50x, and 100x objective lenses, allowing the visualization and measurement of the waveguide output facet with appropriate magnification. Together with the MFD measured using the technique introduced in Section 3.7.7, the V-number of the waveguide was obtained using numerical iterations to obtain a value that fits well with the measured MFD. Once the V-number is obtained, the waveguide NA can be calculated using Equation (3.4). It is important to note that the entire measurement was performed under an assumption that the output beam was a single mode Gaussian beam. By making another assumption that the waveguide is

a step index waveguide, in which the cladding was the unexposed region during the direct laser writing process, the index contrast of the waveguide core can be approximated with:

$$NA = \sqrt{n_1^2 - n_2^2} = n_1 \sqrt{2\Delta n} \tag{3.6}$$

$$\Delta n = \frac{n_1 - n_2}{n_1} \tag{3.7}$$

where  $\Delta n$  is the index contrast,  $n_1$  is the laser induced modified index (core) and  $n_2$  is the original refractive index of the target material (cladding).

#### 3.10 Conclusion

This chapter focused on the design, setup, and optimization of the experimental framework for direct laser writing of different transparent material using a high repetition rate femtosecond laser. Details of the experimental setup are described, including the laser system, beam delivery optics, and sample positioning apparatus. Understanding the application of each part of the setup is important for maintaining the quality and precision of the fabrication process throughout the experiments. Sample preparation method is also included in this chapter, involving dicing, cleaning, drop-casting, and polishing of the sample pre- and post- laser processing. Understanding the sample preparation method is essential for achieving consistent laser-induced modification. Characterization techniques that were employed to evaluate the written structures are also included in this chapter. Techniques such as scanning electron microscopy, surface profiler, and optical microscopy were utilized to access the physical morphology, surface roughness, and structural integrity of the micro-structures. On the other hand, optical characterizations techniques of the waveguide fabricated are presented, including the insertion loss, propagation loss, coupling loss, and mode field diameter. This chapter highlights the importance of precise control over the laser parameters and the experimental environment in achieving high-quality micro-fabrication. The optimized conditions identified here form the basis for the subsequent experiment, in which they provide a repeatable and reliable results, which are crucial for the practical application of DLW in photonic device fabrication.

#### **CHAPTER 4**

# FEMTOSECOND LASER WRITTEN SODA LIME SILICATE GLASS WAVEGUIDE.

#### 4.1 Introduction

This chapter presented direct laser writing in soda lime glass for optical waveguide fabrication. The objective of this research is to study the bulk modification of soda lime glass using 515 nm femtosecond laser and its application as optical waveguide. Therefore, the first part of the experiment involves the waveguide fabrication by systematically adjusting the pulse energy and translational speed to study the impact of each laser writing parameters to the bulk modification. Following that, the optimal laser processing parameters for waveguide fabrication in soda lime glass will be examined. The second half of the experiment will be the characterization of the fabricated waveguide. The characterization process involves the measurement of the mode field diameter, insertion loss, propagation loss, and the index contrast of the fabricated waveguide.

## 4.2 Waveguide Fabrication

Systematic adjustments were made to both the pulse energy and sample scanning speed to determine the optimal parameters for creating the waveguide. The pulse energy was controlled within the range of  $0.4-5~\mu J$ , while the scanning speed ranges from 0.1~to~2~mm/s. Waveguide fabrication for all the laser parameters was carried out using single-scan technique, where each waveguide was distant by  $100~\mu m$  to prevent overlapping with the neighbouring waveguides. To ensure consistency and repeatability, the waveguide writing process was repeated five times for each set of laser parameters. After the laser writing process, the cross-section of the samples was grinded and polished. The polishing

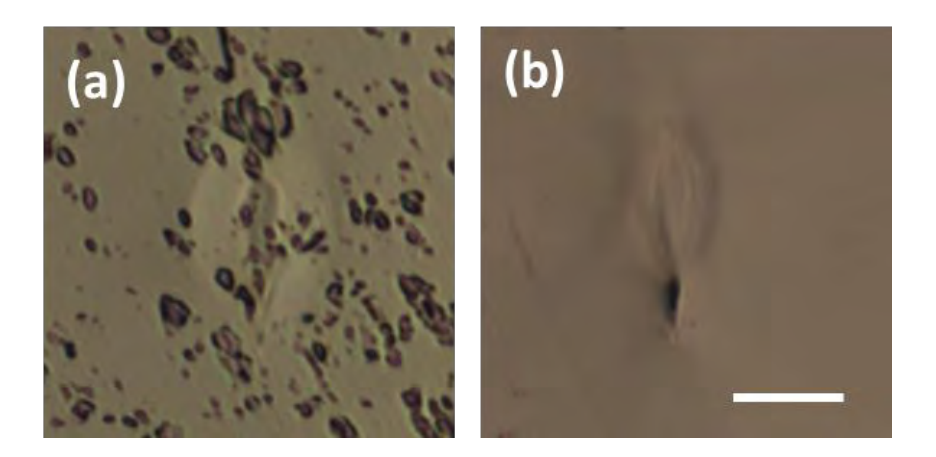


Figure 4.1. Comparison of (a) incomplete polishing, and (b) complete polishing. Scale bar is 30  $\mu m$ .

process started with the use of a 30 microns diamond lapping film for initial coarse polishing, followed by subsequent polishing stages with 15-, 5-, 1-, and 0.6-microns film, each contributing to achieving a progressively smoother surface. The polishing with each film takes about 15 minutes, leading towards a total of 75 minutes for the complete polishing for each side of the sample. The significance of this thorough polishing of the cross-section lies in its role in achieving high quality waveguide facet. The major concern is to minimizes light scattering and enhances light coupling efficiency. A well-polished cross section is vital for ensuring that the waveguide core area appears clean and smooth, as illustrated in Figure 4.1. The additional attention in this post-writing treatment contributes to the overall success of the waveguide fabrication process, ensuring the desired optical characteristics and performance are attained.

# 4.3 Waveguide Cross-Section Analysis

Following the completion of the polishing process, a detailed inspection of the waveguide was conducted using a transmission optical microscope to assess the top and cross-sectional views of the waveguides. For the examination of the waveguide's cross-section,

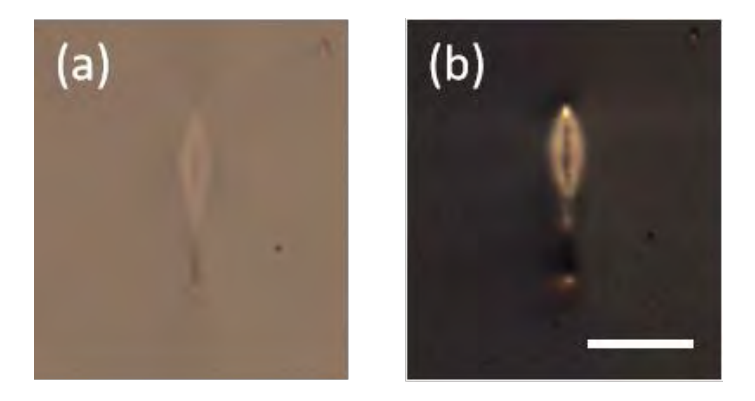


Figure 4.2. Cross-sectional view of the laser written waveguide under 10x optical microscope bottom illumination with (a) open, and (b) close aperture. The scale bar is  $30 \ \mu m$ .

bottom light illumination was employed. This approach was chosen to take advantage of the waveguide's light guiding properties, resulting in the production of a well-defined image under the microscope. To further enhanced the contrast of the image, the aperture of the bottom light was minimized. With that, the background light was significantly reduced, and the boundary of the waveguide is more pronounced. The advantage of this technique is demonstrated in Figure 4.2, which showcases a comparative analysis of open and close aperture. Figure 4.2 (b) shows the image of the waveguide cross-section obtained through bottom light illumination, in which the image exhibited significantly enhanced contrast and aided in the observation of light-guiding region. In practice, the open-aperture configuration was employed to observe the structure, size, and surface morphology of the waveguide, while the closed-aperture configuration was utilized to assist in precisely defining the light-guiding region and the waveguide's boundary.

Investigation of the waveguide cross-section revealed that glass modification is achievable across the range of pulse energies used in the experiment. However, at pulse energy below  $0.7~\mu J$ , the glass showed insignificant modification. A more pronounced modification was only observed at pulse energy higher than  $0.7~\mu J$ . Figure 4.3 presents

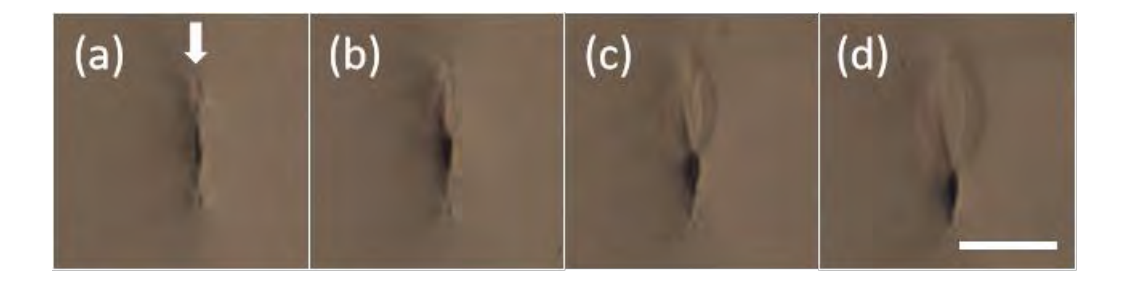


Figure 4.3. Soda-lime glass waveguide fabricated using (a) 1  $\mu$ J, (b) 2  $\mu$ J, (c) 3  $\mu$ J, and (d) 4  $\mu$ J pulse energy, with a scan speed of 0.1 mm/s. Arrow indicates the laser direction. The scale bar is 30  $\mu$ m.

the microscope image of the waveguide written at pulse energies ranging from 1 to 4  $\mu$ J, with a writing speed of 0.1 mm/s. The modified area was found to be a complicated structure consisting of a transparent region at the top and a darker region at the bottom. Below the dark region it was found a tiny bright spot across all fabrication parameters. It was noticed that the depth of the bright spot remained unchanged and is independent of pulse energy  $(1-4 \mu J)$  and sample scanning speed (0.1-2 mm/s). Therefore, the bright spot was attributed as the laser focal spot, where most of the laser energy was deposited before the focus.

At 100 kHz and 0.1 mm/s, the transparent region presented a noteworthy transformation in both shape and size in response to varying pulse energy. At a pulse energy of 1  $\mu$ J, the dimensions of the transparent region produced an area of 4.7 x 13.5  $\mu$ m<sup>2</sup>, as depicted in Figure 4.3 (a). As the pulse energy increases, the transparent region expanded and evolved into an inverted tear-drop shape. The modification was particularly evident when employing 4  $\mu$ J pulses for the modification, resulting in a significantly enlarged transparent region with an area of 20 x 35  $\mu$ m<sup>2</sup>, as shown in Figure 4.3 (d).

To gain further insight of the effects of pulse energy to the modification, the width and height of the transparent region was measured from the transmission microscope images.

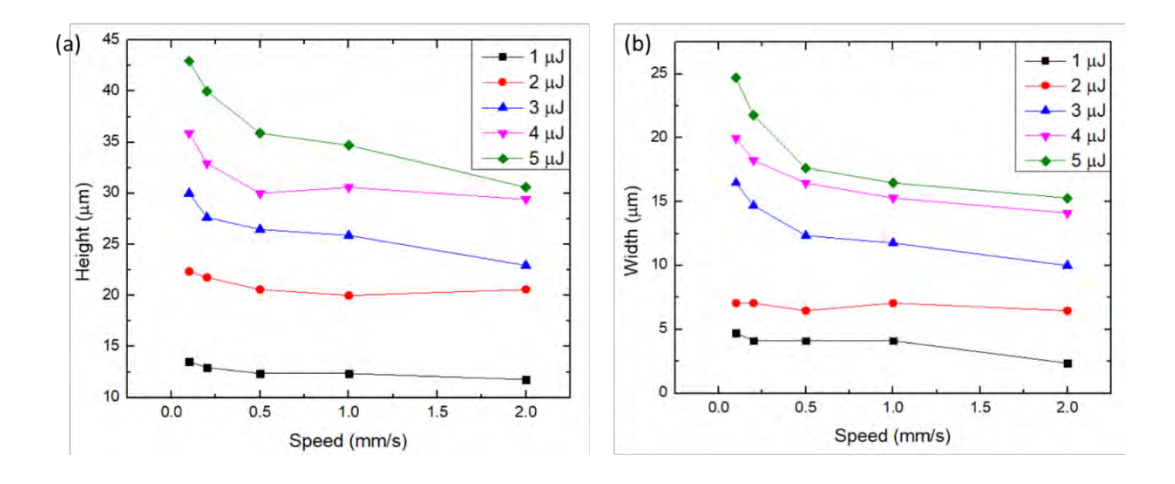


Figure 4.4. Width and height of the transparent region plotted against the sample scanning speed for pulse energies from 1 μJ to 5 μJ.

The measurement result is shown in Figure 4.4 as a function of scanning speed from 0.1 -2 mm/s for the pulse energies ranges from 1  $\mu$ J to 5  $\mu$ J. Notably, for pulse energies exceeding 3 µJ, the height and width of the transparent region showed insignificant changes (1  $\sim$  2  $\mu$ m) at scanning speeds higher than 0.5 mm/s. As the scanning speeds reduces, interestingly, the transparent region experienced an exponential enlargement in both width and height. These results indicate a strong heat accumulation effect during the laser processing at this regime. Direct laser writing with high repetition rate femtosecond laser typically associated with heat accumulation effects as the primary mechanism for inducing material modification (Eaton et al., 2005; Huang et al., 2011b; Minoshima et al., 2001; Schaffer, Brodeur, García, et al., 2001). This is because the thermal diffusion time (35 µs (Sakakura et al., 2015)) is longer than the interval between successive pulses at 100 kHz (10 µs), hence there is no sufficient time for the material to cool down in between the laser pulses. The temperature at the focal spot is subsequently increased due to the accumulation of large thermal energy within the voxel, facilitating material modification. Further increase in the incident laser energy from 3 µJ to 5 µJ resulted in much higher initial temperatures and more pronounced heat accumulation effects, leading to the creation of larger transparent regions. However, there is no evidence of strong heat

accumulation effects for transparent regions produced by pulse energies below 2  $\mu$ J, as the dimensions remained relatively constant across all tested scanning speeds. This result suggests that 2  $\mu$ J is the threshold for material modification without strong thermal expansion by heat accumulation effects. Beyond this critical threshold, the material experienced abrupt structural changed associated with the increased pulse energy due to the enhanced heat accumulation at 3  $\mu$ J.

Based on the observations leads to a conclusion that the formation mechanism of the soda-lime glass waveguide involves a complex interplay of multiple thermal events. At 1 μJ, the interaction between the glass and the high repetition rate femtosecond laser initiates the temperature elevations, facilitated by the heat accumulation of the high energy pulses. The elevated temperature around the laser focal spot then induces thermal ionization, generating a high density of free electrons through avalanche ionization. The rapid buildup of the free electrons density results in damage, ultimately giving rise to the formation of a dark region near the laser focal spot. As the pulse energy further increases, the heat accumulation intensifies. The excess thermal energy diffuses outward from the focal spot, following the direction of the laser source. Subsequently, the accumulated thermal energy produces a heat affected zone before the damage area. Further increase the pulse energy to 3 µJ will induce strong heat accumulation effects leading to the formation of a transparent region by thermal expansion. The consequence of the strong heat accumulation effects is the transformation of the transparent region from an elongated structure at 2 µJ to an elliptical one at 3 µJ, where the diameter of the transparent region expanded by 2-folds. This observation emphasizes the pivotal role of pulse energy in shaping the generated waveguide structure.

## 4.4 Waveguide Mode Analysis

Light guiding region is revealed with near field imaging in conjunction with light coupling using single mode fiber (SMF-28) at 1550 nm at the input facet. The near field image from the waveguide output was imaged by a 40x (0.65 NA) objective lens into a CCD camera. Near field images are presented on the right-hand side of their respective waveguide in Figure 4.6. It is interesting that light guiding can only be observed at the top area transparent region, whereas no light is observed from the central area as well as the dark region at the bottom. The waveguiding region was located within the 4.5 x 7 µm<sup>2</sup> area near the peak of the transparent region. This observation indicates that within this modified area has a positive index changed and it is identified as the core of the waveguide. In contrast, no visible light guiding within the central of the transparent region and the darker area at the bottom, indicating negative index changed within these areas.

A rather symmetrical beam can be seen in Figure 4.5 (a-b) whereas the beam shape is slightly distorted for the waveguide fabricated using 3 μJ of pulse energy, as illustrated in Figure 4.5 (c). The formation of the distorted beam profile indicates that there exists two area across the transparent region with different refractive index, an outer ring with a positive index changed, and the central area with a negative index changed. Similar phenomenon was observed and explained by Manuel *et al* where the heat accumulation in the glasses produced a temperature gradient that causes the migration of ions within that vicinity, resulting in areas of different refractive indices (Macias-Montero et al., 2021). They found that network former (Si ion) tends to migrate towards the centre of the molten region, whereas the glass modifiers ion such as Na, K, or Ca will preferentially move towards the peripheral of the modified regions due to the temperature gradient. The migration of glass modifiers towards the peripheral region is due to the large diffusion coefficient of those modifiers, whereas the glass network former will agglomerate at the



Figure 4.5. Microscope cross-sectional image (left hand side) and near field image (right hand side) of the 515nm femtosecond laser induced waveguide at (a) 1 μJ, (b) 2 μJ, and (c) 3 μJ respectively. Scale bar is 30μm.

laser focal point due to their strong binding energy (Kanehira et al., 2008; Liu et al., 2009; Liu et al., 2008). In this case, the large amount of glass modifiers at the peripheral region (transparent region) increases the local refractive index and thus creates the light guiding core. For the modification at high energy laser (3  $\mu$ J), the strong heat accumulation effects cause the migration of greater amount of glass modifier ions towards the peripheral region. Since the migration is of random direction from the high temperature core, an outer ring with higher refractive index is formed around the transparent region, leaving the central with a lower refractive index. Consequently, the homogeneous index changes across the outer ring granted the entire structure the similar light guiding ability, thereby producing the distorted beam profile that follow the pattern of the structure.

To gain further insight of the beam profile, curve-fitting was performed on the near-field images of the beam profile using an image analysis tools (ImageJ). The resulted graph was presented in Figure 4.6, showing the intensity variation of the beam as a function of the radial position. The solid curve represents the actual intensity variation of the beam profile, whereas the dotted curve represents the Gaussian-beam fitting. It is clearly observed that the mode profile of the waveguide fabricated using 1 µJ of pulse energy has a relatively poor fitting with the Gaussian distribution in comparison with the other two beam profile produced by with pulses at higher energy levels. The poor fitting can be attributed to the insufficient amount of glass modifier ions produced at this energy

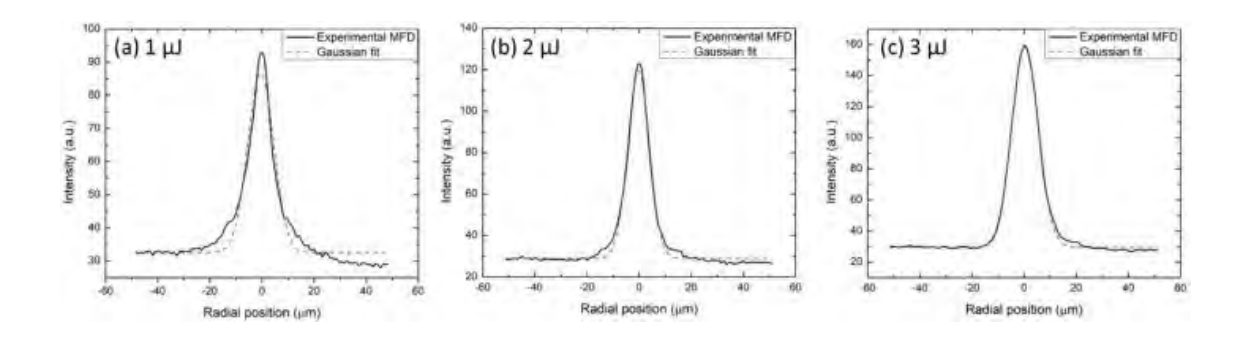


Figure 4.6. Near field profile of the waveguide (a) 1  $\mu$ J, (b) 2  $\mu$ J, and (c) 3  $\mu$ J.

level to provide significant refractive index changed to the glass. In contrast, the waveguide fabricated at 2 - 3  $\mu$ J both show a good fitting with the Gaussian profile, despite the waveguide fabricated at 3  $\mu$ J having a distorted beam profile as shown in Figure 4.5 (c). This is because the curve fitting was performed on the horizontal axis across the centre of the beam profile, therefore the characteristic of the distorted beam at 3  $\mu$ J in the lateral position is less pronounced. These results provided an important information where there is a narrow processing window to produce waveguide in sodalime glass using 515 nm femtosecond laser. For waveguide fabricated at 1  $\mu$ J, the induced modification is insufficient to produce a waveguide that emits Gaussian beam, whereas fabrication with pulse energy higher than 3  $\mu$ J leading to the formation of distorted beam profile due to the strong heat accumulation effects. As a conclusion, it is confirmed that the optimal pulse energy for waveguide fabrication is 2  $\mu$ J in this work.

# 4.5 Mode Field Diameter and Refractive Index Contrast

The MFD of the waveguide was determined by analysing the beam profile shown in Figure 4.5. Since the beam profile was captured using a CCD camera in pixel units, it is necessary to convert these units into micrometres for accurate MFD descriptions. To achieve this, a single-mode fiber (SMF-28) with a known MFD was selected to facilitate

the calibration process. The near-filed output beam profile of the waveguide was first projected onto the IR camera using an objective lens (0.65 NA), and the resulting image was captured in unit pixels. Subsequently, the waveguide was replaced with a SMF-28 fiber, and the near-field image of the fiber tips was captured once aagin. Both images were analysed using ImageJ, an image processing tool, to determine their respective MFDs in unit of pixels. Through a comparison with the official data sheet's MFD values for SMF-28, the MFD of the laser written waveguide can then be determined. Further details regarding the measurement setup are shown in Section 3.7.7.

Upon obtaining the MFD of the waveguide, it becomes possible to estimate the refractive index contrast ( $\Delta n$ ) induced in the waveguide core using the near-field images of the waveguide mode profile, using Equation (3.3) and (3.4). It is important to note that certain assumptions were made in these calculations, namely:

- 1) assuming a step-index waveguide, and
- 2) assuming radial symmetry in the waveguide core.

An explanation of these assumptions can be found in the same Section 3.5.7. With these assumptions in place, the measured MFD enables a rough estimation of the  $\Delta n$  induced in the waveguide core through Equation (3.6).

In consideration of the actual device application, MFD measurement was carried out exclusively for the optimized waveguide, which is the one fabricated using pulse energy and scanning speed of 2  $\mu$ J and 0.1 mm/s. Using the measurement technique mentioned above, the MFD of the laser written waveguide was determined as 9.7  $\mu$ m, which is comparable to the 10.4  $\mu$ m MFD of the SMF-28 fiber at 1550 nm. It is advantageous to have matching MFD between the waveguide and the optical fiber, where it enables light coupling with minimum coupling loss. Following with the MFD measurement, the V-

number of the waveguide was obtained by numerical iteration using Equation (3.3), resulting in values of 1.3485. The V-number is smaller than 2.405, which indicates that the waveguide is a single mode waveguide. This calculated result agrees well with the beam profile observed in Section 4.6. The V-number was then used in Equation (3.4), together with waveguide diameter of 4.5  $\mu$ m, to obtain the value of numerical aperture of the waveguide. Mathematical calculation shows that the laser written waveguide achieved a high NA 0.148. This approximated NA was the highest achievable value for laser writing waveguide in soda-lime glass as of the preparation of this dissertation. In conjunction with the high numerical aperture of the waveguide, the index contrast,  $\Delta n$  of the waveguide core was estimated to be 4.7 x  $10^{-3}$  by employing  $n_2 = 1.5247$  into Equation (3.6) and (3.7). The index contrast was among the highest value recorded in comparison with the waveguide writing in fused silica and borosilicate glass, showing the excellent optical characteristics of the soda-lime glass waveguide fabricated in this work. Optical loss measurement was necessary to further characterize the optical performance of the soda-lime glass waveguide.

## 4.6 Propagation Loss Measurements

In order to assess the propagation loss of the waveguide, insertion loss of the waveguide was first measured. A continuous-wave laser operating at 1550 nm was first connected to two single-mode fibers (SMF-28), without passing through the waveguide. This step was taken to directly measure the optical power originating from the input source, which serves as a reference value representing the initial input power. Subsequently, the waveguide was inserted between the fibers, and the laser was butt-coupled into the waveguide using the SMF-28 fibers at the waveguide input and output facets. Optical power measurements were conducted once again. The difference between

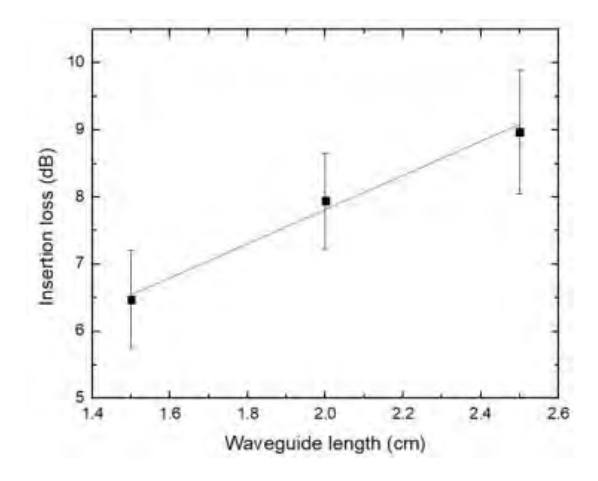


Figure 4.7. Insertion loss measurement of the waveguide fabricated at 2  $\mu J$  and 0.1 mm/s.

the optical power before and after the insertion of the waveguide constituted the insertion loss. Details of the measurement setup can be found in Section 3.7.4. Multiple measurements were carried out for each waveguide, and the average insertion loss was calculated to accommodate any variations in the experimental setup or waveguide performance. Cut-back method was then carried out by cutting the waveguide into 3 different lengths, and the measurement process was repeated to estimate the propagation loss of the waveguide.

It is commonly known that slight changes in the fabrication condition such as fluctuation of laser power, polishing quality of the waveguide facets, surface contamination, etc, will give rise to a different waveguide performance despite the waveguide was fabricated under the same fabrication condition. Therefore, to account for the fabrication error, multiple straight waveguides were fabricated on the same glass sample at 2 µJ and 0.1 mm/s scan speed. Averaging the measurements from all the waveguides fabricated under the same conditions can provide a better estimation of the loss. By plotting the average insertion loss of the waveguides against the waveguide length, the average propagation loss of the waveguide can be obtained from the gradient

Table 4.1. Summary of laser written glass waveguide characteristics.

Glass	$\lambda_{write}$	$\lambda_{\text{couple}}$	L <sub>prop</sub>		References
	(nm)	(nm)	(dB/cm)	$\Delta n (x 10^{-3})$	
FS	400-1400	660	-	0.42 - 1.65	(Hernandez-Rueda et al., 2017b)
FS	800	800	-	0.7 - 1.3	(Blömer et al., 2006)
FS	514	777	0.1	1.8 - 3.5	(Guan et al., 2017)
FS	800	633	-	0.07	(Chan et al., 2003)
BS	515	808	0.86	1.0	(Eaton, Ng, et al., 2008)
BS	800	633	-	1 – 5	(Minoshima et al., 2001)
BS	800	633	-	5	(Kedia et al., 2015)
BS	800	635	0.5	0.3	(Dharmadhikari et al., 2011)
BS	1030	1550	0.65	3	(Mittholiya et al., 2017)
BS	1045	1550	0.35	1 – 7	(Eaton, Zhang, et al., 2008)
SL	800	633	0.03	1.4	(Tong et al., 2006)
SL	800	800	1.64	-	(Kowalevicz et al., 2005)
SL*	515	1550	2.5	4.7	

<sup>\*</sup>Results from current work \*\*FS: Fused Silica; BS: Borosilicate; SL: Soda Lime

of the curve. Figure 4.7 presents the measurement results. Linear fit of the experimental data show that the propagation loss of the waveguide is 2.5 dB/cm. Error bar is included in the plot to show the measurement uncertainty of the insertion loss arising from all the waveguides measured. The good agreement of the linear fitting with the error bar indicates that all waveguides exhibit identical propagation loss, and good repeatability of the waveguide fabrication. Despite the good fitting results, the waveguide exhibits higher propagation loss compared to the reported loss in other work, as shown in Table 4.1. Though different coupling wavelength could be one of the reasons of the high propagation

loss, the dominant factor can be attributed to the inhomogeneity of the glass components, causing fluctuations in the laser induced refractive index in the core. Non-uniform refractive index along the waveguide core will result in scattering loss when the light propagates inside the waveguide.

Coupling loss of the waveguide can be obtained from the Y-intercepts of insertion loss vs waveguide length (Figure 4.7), where the propagation loss is omitted. In this case, the average coupling loss of the waveguide fabricated at 2 µJ is 2.8 dB. It is important to note that typical coupling loss is about 0.5 dB per facets (Eaton, Zhang, et al., 2008; Tong et al., 2006). To investigate the source for the high coupling loss for the waveguide, analytical calculations based on the mismatch losses were carried out. Generally, coupling loss arises from the mismatch between the properties of the waveguide emitter and receiver. Typical mismatch loss including NA mismatch loss, MFD mismatch loss, and waveguide core mismatch loss are all possible factors to the coupling loss. By using Equation (3.2) and (3.5), the NA and MFD mismatch losses were calculated. Interestingly, due to the good match of the NA and MFD of the fabricated waveguide and the SMF-28, these mismatch losses exhibit insignificant contributions toward the coupling loss. The NA and MFD mismatch loss between the waveguide and SMF-28 fiber was found to be 0.47 dB and 0.019 dB respectively, providing only 0.508 dB to the total coupling loss. Further investigation found that the large coupling loss might have come from the elliptical mismatch loss between the input fiber and the waveguide. During the measurement, the 1550 nm laser is emitted from SMF-28 with a circular core diameter (8.2 µm), coupled into the laser written waveguide having an elliptical core with an area of 4.5 x 7 µm<sup>2</sup>. Light coupling between a circular core fiber and an elliptical core waveguide might give rise to the ellipticity mismatch loss, whereby the light propagates through the waveguide encounters a mismatch in the mode between the emitting and receiving waveguide. Therefore, the excess coupling loss of 2.29 dB was attributed to

ellipticity mismatch loss. It is challenging to validate the exact value of the ellipticity mismatch loss with an analytical method, however, it is possible to address the upper and lower limit of the loss by calculating the optical loss along the heigh and width of the core, with the expression:

$$Loss_{EM}(dB) = -10 \log_{10} \left(\frac{a_2}{a_1}\right)^2, a_2 < a_1$$
 (4.1)

where  $a_1$  is the core diameter of the optical fiber and  $a_2$  is the height or width of the waveguide core. For instance, substituting 4.5 µm and 7 µm simultaneously into  $a_2$ , and 8.2 µm into  $a_1$  in Equation 4.1, the upper and lower limit of the ellipticity mismatch loss at the input coupling facets was found to be 5.2 dB and 1.4 dB, respectively. The excess coupling loss falls within the range of the theoretical limit of the loss validates the contribution of 2.29 dB of core diameter mismatch loss towards the total coupling loss.

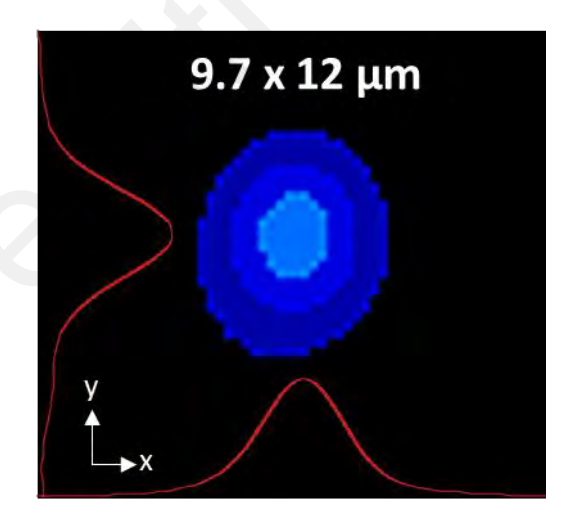


Figure 4.8 Intensity mode profile for single mode soda-lime glass waveguide fabricated at 2  $\mu J$ .

The high elliptical mismatch loss showed that the shape of the waveguide core also plays an important role in waveguide coupling. The core shape determines the distribution of the refractive index within the waveguide, which in turn influences the propagation of

light and the formation of the guided modes. Figure 4.8 shows the intensity mode profile of the waveguide. It is found that the waveguide mode falls into the elliptical regime  $(\omega_x/\omega_y=0.8)$ , where  $\omega_x$  and  $\omega_y$  describes the width of the waveguide mode in both x-and y-direction.

Despite the high index change (4.7 x 10<sup>-3</sup>) and the matching numerical aperture (0.148) with the SMF-28, the composition of the waveguide material also showed a pivotal role in defining the final performance of the waveguide fabricated. Additional efforts are required to enhance the performance of this waveguide. Several methods can be explored to mitigate the observed coupling loss. One approach involves employing a slit beam shaping method to fabricate a waveguide with a more circular core, potentially reducing elliptical mismatch loss. Additionally, refining the coupling technique or exploring alternative materials with different compositions, refractive index, or doping levels could be helpful in improving the waveguide quality. The ultimate objective is to create a waveguide core with dimensions and properties precisely matching those of the existing optical fiber, including shape, dimensions, and numerical aperture. These refinements aim to minimize the insertion loss, leading to improve the overall performance of the fabricated waveguide. However, it is beyond the scope of the current objective of the work and shall be considered as the future project.

## 4.7 Conclusion

In conclusion, fabrication of soda lime glass waveguide using 100 kHz, 515 nm femtosecond laser was presented. The formation mechanism of the laser-induced cross-section was investigated. It is found that heat accumulation effects play a major role in the creation of the transparent region, where ions migration produces multiple zones with

different refractive indices. In combination of the microscope image analysis and beam profile investigations, it is concluded that the optimum laser processing parameters is 2  $\mu$ J at 0.1 mm/s, when employing 515 nm femtosecond laser at 100 kHz repetition rate. The mode field diameter and  $\Delta n$  of the optimized waveguide was determined to be 9.7  $\mu$ m and 4.7 x 10<sup>-3</sup> respectively. These results show that the fabricated waveguide is in good compatibility with the standard single mode fibre for photonics applications. Unfortunately, the waveguide exhibited relatively high propagation loss of 2.5 dB/cm, due to the scattering loss by the non-uniform core refractive index. Further research and development efforts are required to improve the optical characteristics of the waveguide. The outcome of this study demonstrates the pivotal role of each laser processing parameters in controlling the quality of the fabricated waveguide. Nonetheless, the experience gains from this work provided the fundamental knowledge of direct laser writing fabrication and characterization for the lab and for the subsequent experiments.

#### **CHAPTER 5**

# SURFACE ABLATION OF CR-39 POLYMER USING HIGH REPETITION RATE FEMTOSECOND LASER

#### 5.1 Introduction

In this chapter, a 780 nm high repetition rate femtosecond laser was utilized to investigate the response and modification of the thermoset polymer, CR-39. Despite varying the pulse energy and translational speed, the laser was tightly focused into the CR-39 at different focusing depth. By adjusting the laser focus position, the difference between bulk and surface modification was discussed. After that, the experiment will focus on the surface ablation of CR-39 by controlling the number of pulses irradiation per spot to investigate the surface ablation process and efficiency.

## 5.2 Determination of the orders of Nonlinear Absorption

Figure 5.1 shows the UV-visible absorption spectrum of the pristine CR-39 sample, represented by the blue dashed line. The spectrum reveals that CR-39 exhibits strong absorption in the UV region, with an absorption edge at 300 nm. It is clearly that observed that CR-39 exhibits high transmission from visible to near-infrared range where no other significant absorption peaks is observed within this wavelength range. This observation confirms that the linear absorption of CR-39 at 800 nm is negligible and therefore plays a relatively insignificant role in the modifications of CR-39. Instead, it suggests that nonlinear absorption mechanisms are more relevant in the context of laser ablation of CR-39 with 800 nm femtosecond laser. To gain further insight of the absorption characteristics of CR-39, the absorption coefficients is calculated by using the Beer-Lamber law (Sagheer et al., 2016):

$$\alpha_0 = 2.303 \frac{A}{t} \tag{5.1}$$

where  $\alpha_0$  is the absorption coefficient, A is absorbance, and t is the thickness of the sample in cm. The absorption coefficient,  $\alpha_0$ , is an important parameter as it allows the deduction of the optical bandgap of a material from the UV-Vis spectrum using the Tauc relation (Shekhawat et al., 2011):

$$\alpha_0 = \beta \left( h\nu - E_g \right)^2 / h\nu \tag{5.2}$$

Here hv is the energy of the incident photon,  $E_g$  is the optical bandgap energy, and  $\beta$  is a constant. To determine the optical bandgap energy of CR-39,  $(\alpha hv)^{1/2}$  was plotted as a function of photon energy (hv) as shown in the inset of Figure 5.1.

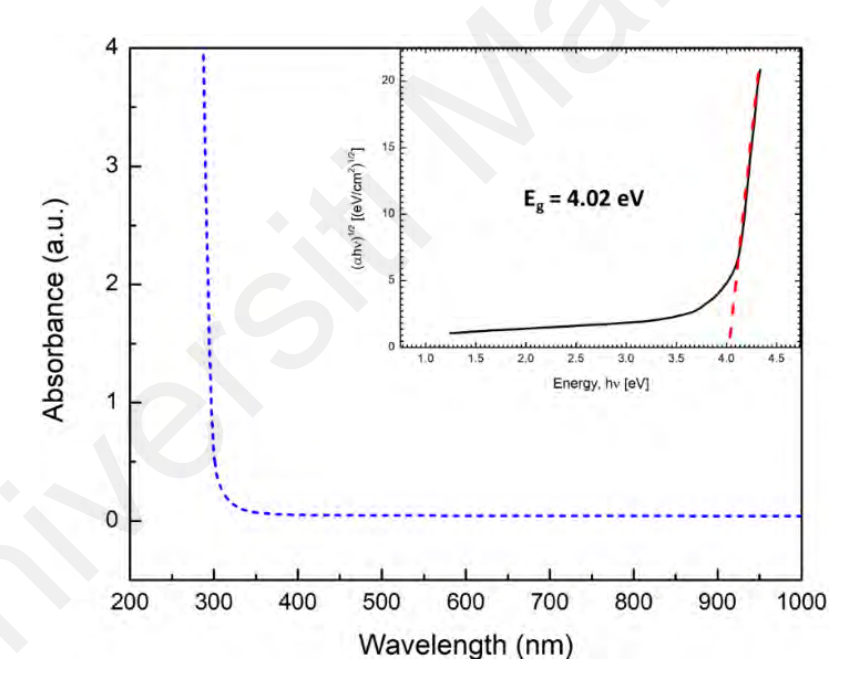


Figure 5.1. UV-VIS spectrum of CR-39. Inset shows the measurement of CR-39 optical bandgap via Tauc plot method.

The optical bandgap energy can be obtained by extrapolating the linear portion of the graph (red dashed line) and the intersection of the extrapolated line with the x-axis represents the bandgap  $E_g$ . The results show that the CR-39 sample exhibits a bandgap of 4.02 eV, which exceeds the single photon energy at 800nm (1.55 eV). Therefore,

multiphoton absorption is required to provide sufficient excitation energy for the ground state electron to overcome the bandgap when doing laser processing of CR-39 using 800 nm femtosecond laser. In combination with the reported three-photon absorption of CR-39 (Dreischuh et al., 2008; Rafique et al., 2010), the measured bandgap of the CR-39 sample justified the potential of using multiphoton absorption to induce laser ablation with the 800 nm femtosecond laser.

## 5.3 Effect of Focusing Depth to Ablation

The laser ablation of CR-39 was performed by focusing the laser onto the target sample at various focusing depths. To create a line ablation across the sample, the sample was translated in the y-direction with the motorized translational stage. While deciding the pulse energy for laser ablation, it is observed that even the smallest pulse energy can induce modification within the sample. However, the use of higher pulse energy had the potential to induce burning and damage to the sample while varying the scan speed and focusing depth. Therefore, to prevent unwanted damage to the sample, the pulse energy used for the experiment was controlled as the minimum achievable pulse energy of the laser writing system, which is 5 nJ. Each line was scanned once using the 5 nJ pulse at a consistent translational speed of 0.5 mm/s. A separation of 50 µm was maintained between adjacent lines to prevent any overlapping between them. The depth at which the laser was focused was adjusted, ranging from the sample surface to a depth of 280 µm beneath the sample surface. The effect of focusing depth to the laser ablated structure was observed and characterized under an optical transmission microscope.

Figure 5.2 displays the structure generated when the laser was focused at a depth exceeding 100 µm beneath the sample surface. The top view image showcases a unique pattern characterized by a sizable dark spot encircled by a ring along the laser scanning direction. To obtain the full picture of the shape of the structure, cross-sectional imaging

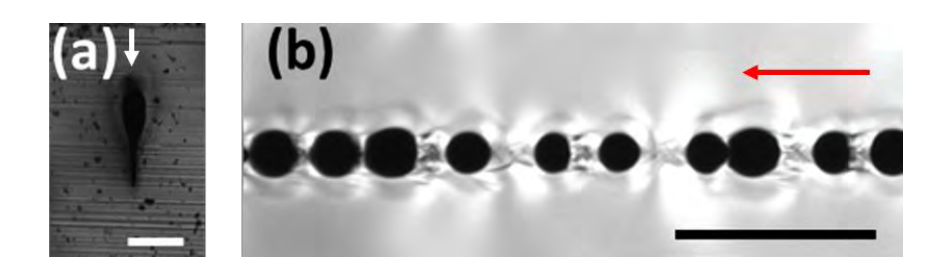


Figure 5.2. Bulk modification of CR-39 at 100  $\mu$ m focusing depth: (a) cross-section; (b) top view. Scale bar is 100  $\mu$ m. White arrow indicates the direction of the incident laser, and red arrow showing the direction of the laser writing.

was carried out, as illustrated in Figure 5.2 (a). The findings revealed that the modified structure exhibits an inverted tear-drop shape, comprising a broad upper part and a narrow lower part.

A noticeable distinction between glass writing and the present study lies in the spotto-spot modification instead of a continuous straight line. For DLW in glass, the high
energy laser could induce continuous modification within the bulk glass, creating a
straight channel waveguide. However, a periodic spot-to-spot modification was observed
instead in the present study. It is believed that the presence of heat affected zone between
the dark spots are hindering the continuous modification. As the heat-affected zone is a
temperature-dependent phenomenon, this area should be able to be minimized or
eliminated by reducing the laser fluence used for laser processing. To test this hypothesis,
an experiment was conducted by increasing the laser processing speed while maintain the
same laser writing power. This adjustment effectively reduces the fluence, F, following
the expression:

$$F = (2\omega_0 R/v)(E/\pi\omega_0^2) \tag{5.3}$$

Figure 5.3 (b) presents the cross-sectional view of the line-scanned structure at high speed. By increasing the translational speed, the laser fluence was reduced from 6.3 kJ/cm<sup>2</sup> at 5 mm/s to 0.63 kJ/cm<sup>2</sup> at 50 mm/s. The cross-section view of the structure

presented a notable trend, where the vertical length of the modified structure gradually reduces with the increases of the speed. The reduction of the length is associated with the diminishing of the broad upper part. This phenomenon is more pronounced as the speed exceeds 20 mm/s (1.6 kJ/cm<sup>2</sup>), where the upper part is totally unobservable. This observation strongly suggests that heat accumulation plays a significant role in the formation of the broad upper part of the tear-drop structure, where 1.6 kJ/cm<sup>2</sup> marked the critical threshold fluence for strong thermal accumulation. Below this threshold, photon energy was absorbed via two-photon absorption, subsequently create the narrow line structure. The strong heat accumulation came from the slow thermal diffusivity,  $\chi$  of CR-39 ranging from  $0.144 - 0.152 \text{ mm}^2/\text{s}$  (Mohammed et al., 2013). This gives rise to an approximated cooling time,  $\tau_c$  of 35-37 µs according to the expression  $\tau_c = (2\omega_0)^2/\chi$ . The laser source used in this experiment is a high repetition rate femtosecond laser with 80 MHz repetition rate. As the temporal pulse duration is 12.5 ns, the accumulated heat doesn't have sufficient time to diffuse out from the focal spot before the next pulse arrives. As the fluence increases, substantial amount of energy was absorbed by CR-39, elevating the local temperature around the laser focal spot. Consequently, the strong thermal accumulation causes collateral damage in the surrounding medium, thereby forming the broad upper part.

A rather interesting observation is the narrow line structure observed at speed higher than 20 mm/s. It was found that the size of this line structure is independent of the translational speed, maintaining at a constant dimension of 15 µm x 80 µm. It is commonly assumed that the enlarged structure is due to the spherical aberrations when laser is focused within the bulk material. However, the expected spot diameter in free space was 2 µm. A 40-folds aberration effects should drastically reduce the peak intensity to below the modification threshold. Therefore, it is more realistic to consider filamentation, a nonlinear optical Kerr effect, that creates the elongated channel.

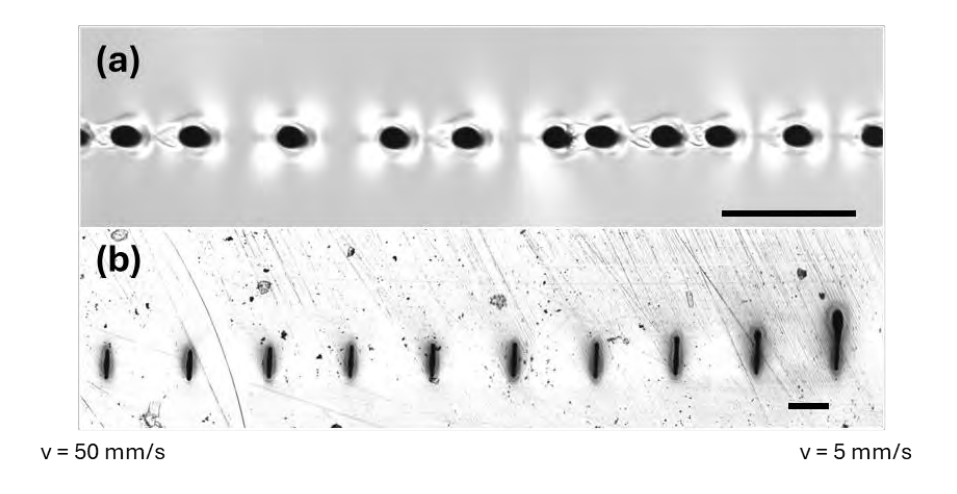


Figure 5.3. (a) Top view for line-scan at 50 mm/s, and (b) cross-sectional view of the line-scanned structure at various speed, from right (5 mm/s) to left (50 mm/s) in a step of 5 mm/s. Scale bar is 100 μm.

When intense femtosecond laser tightly focused into a transparent medium, the laser beam could excite optical Kerr effect, leading to an intensity-dependent changes of refractive index of the medium. The high peak intensity at the central of the laser beam leads to an increased refractive index, effectively focusing the laser beam. This focused laser beam then generates a high density of electron plasma at the laser focus spot through multiphoton ionization. Concurrently, the presence of plasma introduces a defocussing effect, which will then reduce the intensity of the laser beam. As the laser beam continues to propagate in the medium, the focusing-defocussing cycle will repeat for which the laser beam still carrying sufficient power to induce the nonlinear effect. The dynamic balance between this self-focusing and plasma defocussing effect give rise to the formation of the elongated narrow line structure within the bulk CR-39. This concludes that the formation mechanism of the inverted tear-drop structure is a combination of filamentation at the lower part, and heat accumulation effects at the upper part.

Although the formation mechanism of the inverted tear-drop structure is revealed, however, these explanations do not address the question of why a continuous line structure cannot be created within the bulk CR-39. Since the phenomenon cannot be

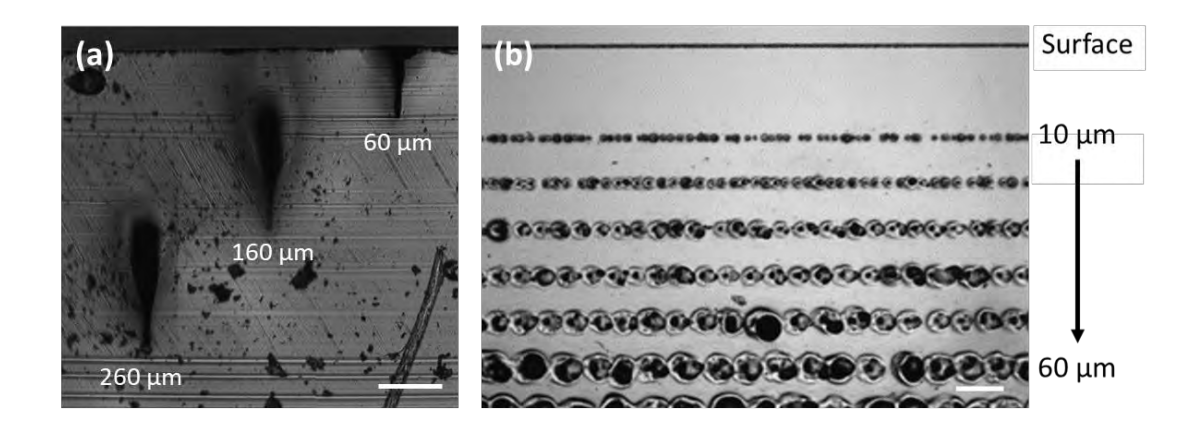


Figure 5.4. (a) Cross-sectional view and (b) top view of microscope image showing the structural variations as the laser focusing depth near the surface. The focus depth was varied with 100  $\mu$ m for (a) and 10  $\mu$ m for (b). The scale bar is 50  $\mu$ m.

explained by the optical properties of the material, it is necessary to discuss in the context of the physical properties of the material. It is important to note that, CR-39 is a type of thermoset plastics (Alauddin et al., 1995), in which thermal treatment on the material will induce chemical reactions to transform the reactive monomers into a cross-linked, much stable three-dimensional polymer matrix. Once it is cured, thermoset plastic will experience an irreversible solidification. Therefore, unlike laser processing in glasses, where the high thermal energy induces melting and the reconstruction of the glass composition, thermal energy will cause an irreversible curing of CR-39. Once it is cured, thermoset plastic will experience an irreversible solidification. In femtosecond laser processing of transparent material like glass and polymers, the typical approach involves modifying the material through melting and reshaping to create a continuous structure along the laser writing path. However, due to the inherent characteristics of thermosetting plastics, such adjustments are not possible once the curing process has occurred. Consequently, the solidification of the material during the modification process prevented the formation of a continuous structure within the bulk of CR-39.

Interestingly, the shape and size of the invert tear-drop structure was found to be independent of the focusing depth. As the laser focus spot approaches the sample surface,

the shape and size of the modified structure remained constant, as illustrated in Figure 5.4 (a). This observation indicated that the absorbed energy is the same regardless the focusing depth. Consequently, the top portion of the modified area was truncated when the focusing depth is shorter than the length of the modified area. A closer examination of the structural variation from the top observed a notable trend, as depicted in Figure 5.4 (b). Here, despite the size of the modification decreased with the focusing depth, there is a remarkable improvement in the irregularity and continuity between the spot-to-spot modification. Upon focusing the laser spot on the sample surface, a straight-line ablation was successfully attained. This observation marked a fascinating distinction in the respond of CR-39 to surface ablation compared to bulk modification. In the case where the femtosecond laser was focused within the bulk, the ablated particles were trapped and unable to escape, leading to continuous thermal energy buildup and subsequent expansion within modified region. It is clearly observed from cross-section image of the bulk modification that the size of the modified region is significantly larger than the spot diameter of the laser, indicating that the modification was primarily driven by the heat accumulation effects. The heated region was subsequently cured, created a solidified boundary hindering the formation of a continuous line. In contrast, when the laser was focused on the surface of CR-39, the ablated particles were allowed to escape into the air. The cured region was subsequently removed by the laser, facilitates the formation of a smooth and continuous line.

These findings provide an important information that continuous structural modification is only available on the surface of the CR-39 sample. The capability of forming a continuous structural modification is an important step in microfabrication as it opens up the possibility to create structure with the desired pattern. In this case, the observation implies that the formation of continuous structure in CR-39 involves the removal of material from the surface of the material. To further investigate the ablation

mechanism, the ablation depth and ablation rate under different laser processing parameters is discussed in the following section.

## 5.4 Ablation Depth and Ablation Rate

High repetition rate laser surface ablation is commonly linked to heat accumulation effects resulting from the temperature buildup caused by numerous femtosecond pulses. Therefore, it is possible to manage thermal accumulation by altering the number of pulses incident onto the surface of the sample. In this case, the number of pulses is controlled by adjusting the laser scanning speed during the ablation process. By varying the sample scanning speed, denoted as v, the number of pulses, N per irradiation spot is manipulated within the range of 1 to 8 x 10<sup>5</sup> pulses per irradiation spot at the pulse repetition rate, R, and the spot radius,  $\omega_0$ , as determined by Equation 5.4:

$$N = \frac{2\omega_0 R}{v} \tag{5.4}$$

A comprehensive list of sample translation speeds, along with the corresponding number of pulses, is provided in Table 5.1. Single-pass line ablation by each number of pulses were employed to generate straight trenches through surface ablation. A 1.5 cm long trenches were produced for each scan speed. To quantify the ablated depth and width, a surface profiler (Dektak D150) was employed in conjunction with an optical microscope (ZEISS microscope) to measure the varying dimensions of the ablated trenches. Multiple measurements were taken across the trenches, and the standard deviation of the data was obtained to improve the precision and accuracy of the measurements.

Figure 5.5 shows the effect of number of pulses per irradiation spot, N, on ablation depth, d, and the corresponding ablation rate. For better visualization of these relationships, the number of pulses per irradiation spot will be referred to as the number of pulses for the rest of the text. The variation in ablation depth across the trenches were

Table 5.1 List of sample travel speeds with the corresponding number of pulses.

Number of pulses have rounded to the nearest whole number.

Sample travel speeds (mm/s)	Number of pulses (x10 <sup>5</sup> )
1.9055	1
0.9528	2
0.6352	3
0.4764	4
0.3811	5
0.3176	6
0.2722	7
0.2382	8

depicted as error bars in the graphs. It can be seen that the onset of LA with high repetition rate laser requires heat accumulation effect generated by multiple laser pulses irradiation on the same spot. This study found that minimum  $1 \times 10^5$  pulses is necessary to achieve consistent thermal ablation on CR-39 using 5 nJ laser pulses. Below this critical threshold, surface ablation will create discontinuous line (not shown). The discontinuity is attributed to the insufficient thermal energy to induce consistent ablation across the sample. Therefore, the results marked  $1 \times 10^5$  pulses as the threshold number to induce thermal ablation.

$$\rho C_p \frac{\partial T}{\partial t} = \nabla \cdot (\mathbf{k} \cdot \nabla \mathbf{T}) + \mathbf{S}(\mathbf{x}, \mathbf{t})$$
 (5.5)

The heat transfer equation (Equation 5.5) was utilized to model the heat accumulation within the bulk CR-39 during high repetition rate femtosecond laser ablation. Here, ρ is the material density (kg/m³), C<sub>p</sub> is the specific heat capacity at constant pressure (J/kg.K), k is the thermal conductivity (W/m.K) of material, and S is the laser energy density applied to the material (W/m³). In this model, the 80 MHz laser pulses were considered as a periodic heat source, given that the timescale for each pulse interval is significantly longer than the material cooling time. Consequently, thermal energy builds up after each

pulse arrives, increasing the local temperature around the focal spot. Solving Equation 5.4 revealed that the estimate surface temperature surpasses 450 K after 1x10<sup>5</sup> pulses, exceeding the glass transition temperature of 360 K for CR-39 (Darraud-Taupiac et al., 1997)). When a material is heated to above its glass transition temperature, it undergoes phase transition from a glassy state to a rubbery state – its viscosity reduces significantly. At this stage, thermal stress builds up at the exposed region, causing surface deformation. Further increasing the temperature will lead to ablation when the threshold stress level is exceeded (Kappes et al., 2014).

Further increase the number of pulses incident on the surface of the sample leading to higher heat accumulation. This results in the effective removal of the particle near the surface, creating trenches with greater depth. The effect of number of pulses to the ablation depth will be discuss in the following section. Despite the laser ablation was performed by incident hundreds of thousands of femtosecond laser pulses on the CR-39, averaging the ablated depth over the number of pulses reveals that the contribution of each laser pulses towards the ablation was merely several picometers (pm) owing to the low energy for each pulse. It is important to note that although the ablation rate, as shown in Figure 5.5 (b), is stated as picometer per pulse, this representation simplifies the data by assuming that ablation occurs using individual pulses. In reality, ablation only begins after the first few tens of thousands of laser pulses, when sufficient thermal energy accumulates to initiate the ablation process.

A detailed examination of Figure 5.5 (a) reveals an interesting trend in the ablation process, which can be divided into two distinctive regimes: the low pulse number regime ( $N < 4 \times 10^5$ ) and the high pulse number regime ( $N > 4 \times 10^5$ ). In the low pulse number regime, as depicted in Figure 5.5 (a), the ablation depth exhibits a linear increase with the increasing pulse number, reaching a maximum ablation depth of 3  $\mu$ m (black curve). This phenomenon is a common observation for ablation of dielectric materials, as reported in

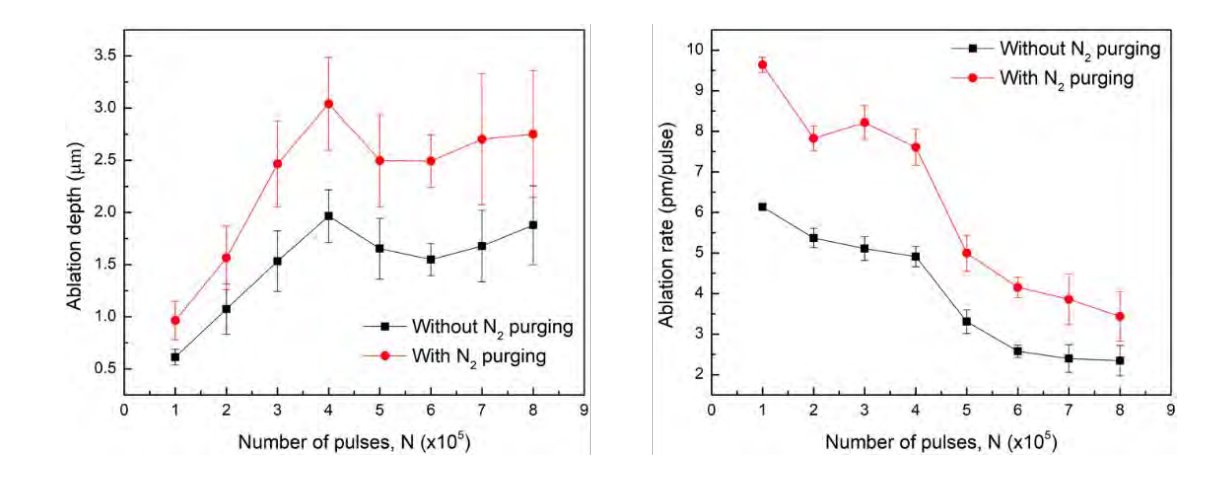


Fig. 5.5 Comparison of laser ablation depth (a), and ablation rate (b) with and without nitrogen purging. Solid symbol indicates ablation with  $N_2$  purging, while hollow symbol indicates ablation without  $N_2$  purging. Solid lines serve to guide the eyes.

reference (Kautek et al., 1996; Krüger & Kautek, 1999; Lenzner et al., 1998). The linear increase of the ablated depth is attributed to the accumulation of thermal energy around the focal spot as the number of pulses increases. Consequently, a larger amount of material is vaporized from the surface, leading to an increase in the ablation depth. The linear trend also signifies the removal of vaporized material from the ablated region without redeposition.

However, as the number of pulses continues to rise, an unexpected behaviour is observed, where the ablation depth plateaus at approximately 2.75  $\mu$ m. To gain deeper insights into the ablation mechanism, the ablation rate was plotted as a function of the pulse number as the black curve in Figure 5.5 (b). Interestingly, the ablation rate exhibits an overall negative trend, decreasing from 6.1 pm/pulse at N = 1 x 10<sup>5</sup> to 2.3 pm/pulse at N = 8 x 10<sup>5</sup>. Despite the linear increase in ablation depth at the low pulse number regime, the ablation rate is gradually reduced. This result suggests the presence of external factor hindering the ablation process. Possible assumptions include redeposition of the vaporized material at high pulse number regime, or the removed particle causes the

incident beam scattering and loses the energy. To address this, a nitrogen purging system was implemented with the goal of removing the ablated particles from the laser focus spot to enhance the ablation rate.

## 5.5 Nitrogen Purging

The sample surface was purged with nitrogen gas at 10 psi during the ablation process. The result for the ablation depth and ablation rate after purging with the nitrogen gas can be found in the red curve in Figure 5.5. It is clearly observed that the sample with nitrogen purging had significantly improved the ablation rate. Consequently, larger volume of the material is removed from the surface, resulting in an overall enhanced ablated depth. For instance, the ablated depth by  $4 \times 10^5$  pulses increased from 1.9  $\mu$ m to 3.0  $\mu$ m. The results suggests that the ablation efficiency is obstructed by a nanoparticles cloud formed by the particles removed from the sample surface(Harilal et al., 2015), which is also known as the plume. The plume who located above the target ablated area could implies a direct implication to the surface ablation, namely the plasma shielding effects (Allahyari et al., 2019). The effective energy reaching the surface of the material is greatly reduced due to scattering by the ablated material. Time-gated imaging by Pereira et al revealed that the plume generated from the laser ablation can last for 15 µs above the ablation region (Pereira et al., 2005). This is at a much longer timescale than the temporal separation between the femtosecond laser pulses used in the experiment (12 ns). Hence, the observed enhancement in ablation rate indicating that the volume of the plume is minimized by the nitrogen gas, thus enabling more photons to arrive at the sample surface unobstructed for ablation. However, saturation of ablation depth at the high pulse number regime is still observed. This suggests that plume should play a minor role in the current experimental condition.

A more probable factor that causes the saturation of ablation depth at high number of pulses is the beam profile distortion due to heat-induced deformation of the sample surface. This phenomenon can be described using the evolution of thermal ablation process at a single laser irradiation spot in 3 stages.

Stage 1: Onset of thermal ablation: At the beginning of laser irradiation, heat gradually built up at the sample surface with increasing number of pulses. With sufficient pulse irradiation, thermal energy diffuses into the laser irradiation spot and a volume of the sample is removed through thermal ablation. This indicates the onset on thermal ablation, which occurs at  $1 \times 10^5$  pulses for PADC.

Stage 2: Linear increase of ablation depth with number of pulses: Additional pulse irradiation after the onset of thermal ablation leads to larger ablation depth, which increases from  $0.96\mu m$  to  $3.04\mu m$  as the number of pulses increased from  $1x10^5$  to  $4x10^5$ .

Stage 3: Saturation of thermal ablation: When the number of pulses exceeding  $4x10^5$  per irradiation spot, excess thermal energy generated from laser irradiation leads to further heating and eventual "softening" of the sample volume around the laser irradiation spot. This changes the surface morphology of the laser irradiated sample surface, potentially distorting the focused laser beam via defocussing effect. Therefore, the laser intensity after the "softened" sample volume is greatly reduced and becomes insufficient for further thermal ablation.

The excessive accumulation of thermal energy in samples subjected to a high number of laser pulses is evident in the SEM images presents in Figure 5.6 (f) – (i), showcasing a notable smoothening of the ablated surface. It can be seen that the ablated trenches exhibit increasing smoothness with the increase in the number of pulses, particularly within the range of 5 x  $10^5$  pulses to 8 x  $10^5$  pulses. This phenomenon indicates a process known as thermal reflow, characterized by the softening and reshaping of the material volume surrounding the trenches. Thermal reflow is a process in which a material

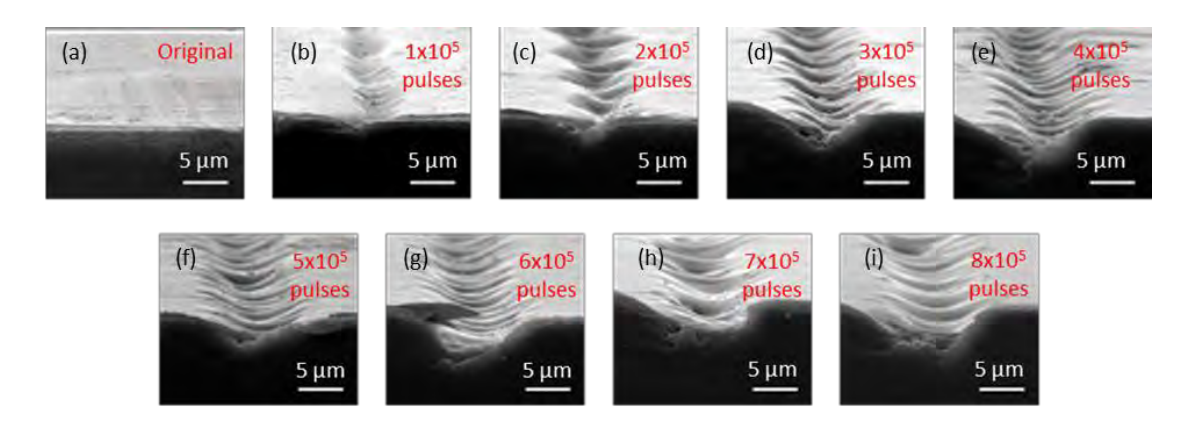


Fig. 5.6 SEM images of (a) original PADC (before ablation), and laser ablation on PADC with 5 nJ pulse energy at varying number of pulses: (b) - (h)  $1 \times 10^5$  to  $8 \times 10^5$  pulses respectively

undergoes localized melting or softening due to exposure to elevated temperature. During thermal reflow, the material in the vicinity of the laser-irradiated area experiences a transient phase change from solid state to a more fluid state, enabling softening and reshaping of the material around the laser focal spot (Kirchner & Schift, 2019). For instance, thermal reflow has been an established technique in the fabrication of polymeric micro-lens (Chidambaram et al., 2017; Kirchner et al., 2017). This technique is applied as the post-processing of the fabrication to reshaped and smoothen the surface roughness of the micro-lens fabricated by heating the resist beyond its softening point. However, in the current study, the softening of the material induced by thermal reflow during the ablation process leading to the geometrical distortion of the sample surface. Consequently, the altered surface morphology causes the deformation of the focused beam of the subsequent laser pulses. This distortion alters the laser intensity at the focal point, influencing the precision and effectiveness of the ablation process. The reshaped surface of the trenches scatters or absorbs laser energy differently, contributing to the saturation of ablation depth. As a result, the efficiency of the overall laser ablation process is impacted as subsequent laser pulse encounter a modified material surface.

This study emphasizes the need for careful manipulation of laser ablation parameters, particularly in cases where excessive thermal energy accumulation can lead to unintended consequences. While thermal reflow has proven useful in specific applications such as micro-lens fabrication, its occurrence during the ablation of CR-39 introduces challenges due to the distortion of the laser beam and alteration of the effective laser intensity on the sample surface. Understanding and mitigating thermal reflow effects become critical for maintaining the efficiency of the ablation process, ensuring consistent and controlled material removal. Further investigation and optimization of laser ablation parameters, along with the development of advanced techniques to minimize thermal reflow, are essential to enhance the precision and reliability of laser processing on CR-38 and similar materials.

#### **5.6 Conclusion**

This study investigated the surface ablation of CR-39 utilizing a low energy, high repletion rate femtosecond laser. In contrast to single pulse ablation, the use of high repetition rate femtosecond laser facilitates the heat accumulation effects, enabling surface ablation with low energy pulses. Specifically, the study presented CR-39 surface ablation by 1 x 10<sup>5</sup> femtosecond laser pulses at 5 nJ pulse energy. The size of the ablated trenches experienced a gradual expansion with the increasing number of pulses. However, the ablation depth was saturated when the laser ablation was performed with more than 4 x 10<sup>5</sup> pulses. In depth analysis suggested that the saturation of ablation depth at high pulse number regime was stemming from the disruption of laser focusing via thermal reflow. These findings provide valuable insights into the surface ablation of polymer substrates using low energy and high repetition rate lasers. Further exploration and optimization of the laser parameters are required for enhancing the efficiency of the surface ablation process.

#### **CHAPTER 6**

# SINGLE-MODE SU-8 WAVEGUIDE FABRICATION WITH ULTRAFAST DIRECT LASER WRITING.

#### 6.1 Introduction

This chapter presents a comprehensive study on direct laser writing in SU-8. First, multiple straight channel waveguide was fabricated under varying laser writing conditions i.e. pulse energy and translational speed. Optimal laser writing parameters were obtained by observing the structure of the waveguide fabricated under different laser writing conditions. A 50:50 directional coupler was subsequently fabricated by employing the optimal laser writing parameters. To further explore the potential of SU-8 in 3D fabrication, a standing waveguide was fabricated, which consists of a suspended waveguide connected with surface waveguide via a vertical S-bend. The fabrication and characterization of each waveguide was explained in detail in their respective sections.

## 6.2 Straight Channel Waveguide

Polymerized SU-8 was first observed for DLW at the laser power of 80 mW, corresponding to a laser intensity of 198 MW/cm<sup>2</sup>. However, polymerization at this power level did not occur along the entire laser scanning path, instead, incomplete/broken straight waveguide channels was found across the entire laser writing area (not shown). The same was observed when the laser power was set higher at 100 mW. Complete straight waveguide channels can be consistently produced only when the laser power was increased to 120 mW (293 MW/cm<sup>2</sup>), which falls within the intensity range reported in Ref (Teh et al., 2004; Tsutsumi, Sakamoto, et al., 2017). The waveguide width variation

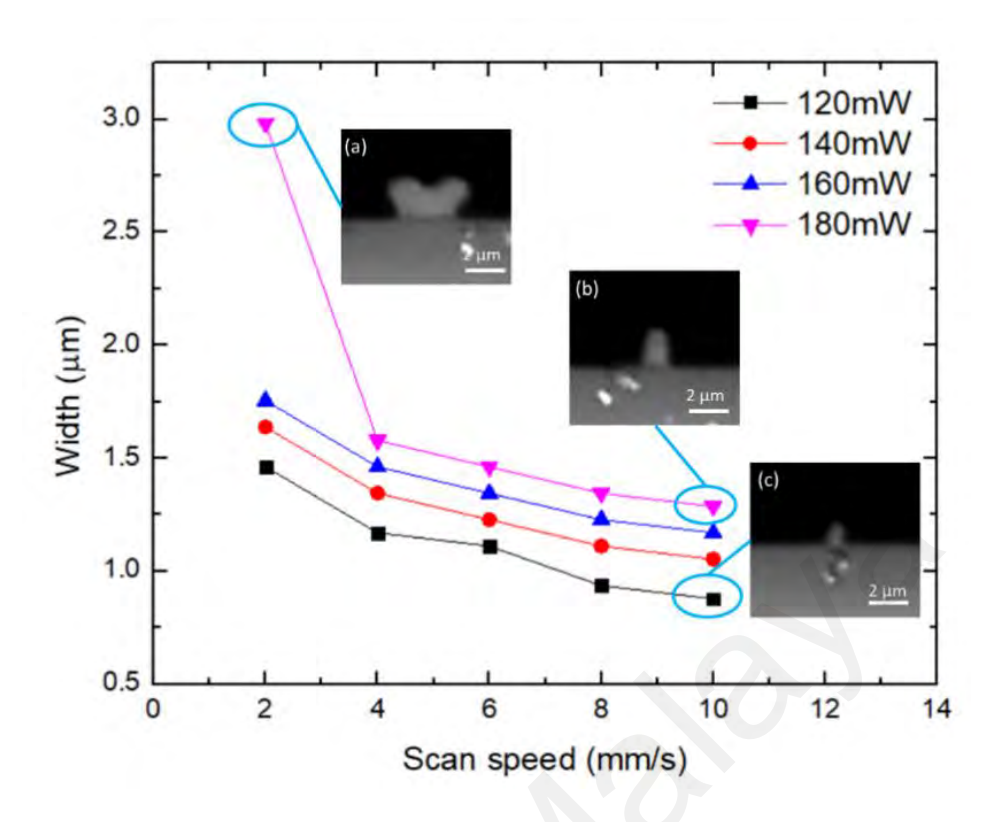


Figure 6.1. 2PP SU-8 waveguide width variation at different laser writing power and scanning speed.

at different laser power and sample scanning speed is shown in Figure 6.1. The width was measured from the cross-section of the fabricated waveguide, at full width at half maximum (FWHM). Figure 6.1(c) shows the cross-section of the SU-8 waveguide fabricated with a laser power of 120 mW and a scanning speed of 10 mm/s. Under this fabrication condition, polymerization of the SU-8 was still incomplete, creating a waveguide with a height of 1.0  $\mu$ m, which is smaller than the SU-8 coating thickness of 1.8  $\mu$ m. Together with a waveguide width of 0.9  $\mu$ m, the waveguide core size was too small for efficient light coupling with standard single mode fiber (eg. 8.2  $\mu$ m core diameter for Corning SMF-28). As scanning speed was reduced to 2 mm/s, the waveguide width was broadened to 1.5  $\mu$ m, which is a common characteristic of the photopolymerization process as the exposure time increases. A similar trend was observed while varying the laser writing power. At a scanning speed of 10 mm/s, the waveguide width increases from 0.9  $\mu$ m to 1.3  $\mu$ m when the laser power increases from 120 mW to

180 mW. In both cases, it was found that complete volumetric polymerization was achieved due to the increase in energy absorbed per unit volume of the SU-8 layer (180 mW and 10 mm/s; 120 mW and 2 mm/s), creating a waveguide with a flat top surface as shown in Figure 5.1(b). Reducing the scanning speed from 10 mm/s to 4 mm/s while maintaining laser power at 180 mW will increase the waveguide width from 1.3 μm to 1.6 μm. However, further reducing the scanning speed to 2 mm/s will result in an abrupt increase of the waveguide width to 3.0 μm, which is a result of laser induced thermal damage of the SU-8 as shown in Figure 6.1(a). A similar observation was reported by Cheong *et al*(Cheong et al., 2016).

#### **6.2.1 Effects of Fluence**

To determine the range of laser fluence that can be used to achieve complete polymerization (flat-top surface), the laser fluence,  $F_{pulse}$  as a function of laser parameters and scanning speed, v, was calculated. The laser fluence per pulse is expressed as,

$$F_{pulse} = 2P_{avg}/R\pi\omega_0^2 \tag{6.1}$$

where  $P_{avg}$  is the average laser power in mW, R is the pulse repetition rate, and  $\omega_{\theta}$  is the beam radius at  $1/e^2$ . The total number of pulses irradiated per spot is in turn,

$$N = 2\omega_0 R/v \tag{6.2}$$

where v is the scanning speed in mm/s. The total fluence irradiated per spot can be obtained by taking the product of Equation (6.1) & (6.2),

$$F_{total} = NF_{pulse} \tag{6.3}$$

The variation of total fluence at each laser power and scan speed combination is shown in Figure 6.2. Here, the polymerization state of SU-8 can be categorized into incomplete polymerization (grey bar), complete polymerization (blue bar), and damaged (red bar).

Complete polymerization is defined as the waveguide with a flat top surface, and the height of the waveguide is  $\pm$  0.1 µm from the thickness of the SU-8 film (1.8 µm), while any other waveguide height lower than this value is defined as incomplete polymerization. Figure 6.2 shows that laser fluence of < 1.8 kJ/cm² is insufficient to achieve complete polymerization. At this fluence level, the fabricated waveguide has a round top surface, which follows the Gaussian beam intensity profile. When the laser fluence increased to >1.8 kJ/cm², a flat top surface waveguide can be fabricated, and the waveguide width increases linearly with laser fluence as discussed in the previous section. Thermal damage occurs when the laser fluence is > 10 kJ/cm². Thus, complete polymerization of the SU-8 thin film can be achieved by using combinations of laser power and scanning speed that produce laser fluence between 1.8 kJ/cm² and 10 kJ/cm².

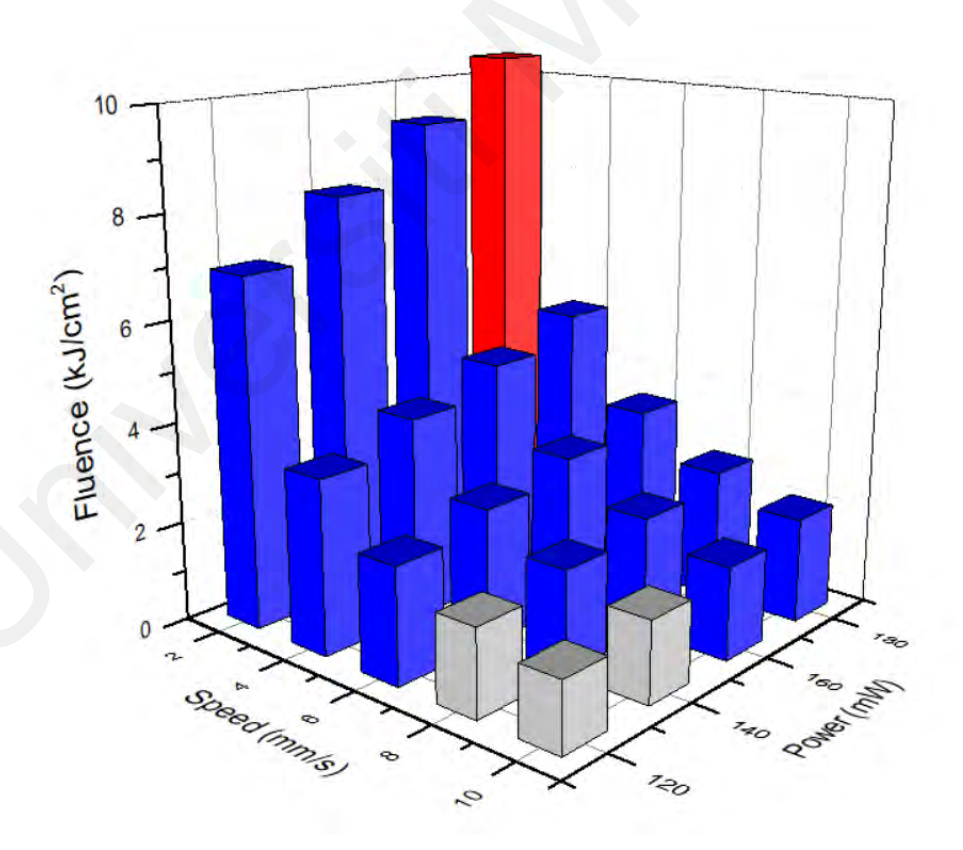


Figure 6.2. Bar chart showing the effect of laser fluence to the SU-8 modification state. Grey, blue, and red bar each indicate the state of SU-8 polymerization: incomplete polymerization, complete polymerization, and thermal damage.

## 6.2.2 Waveguide Loss

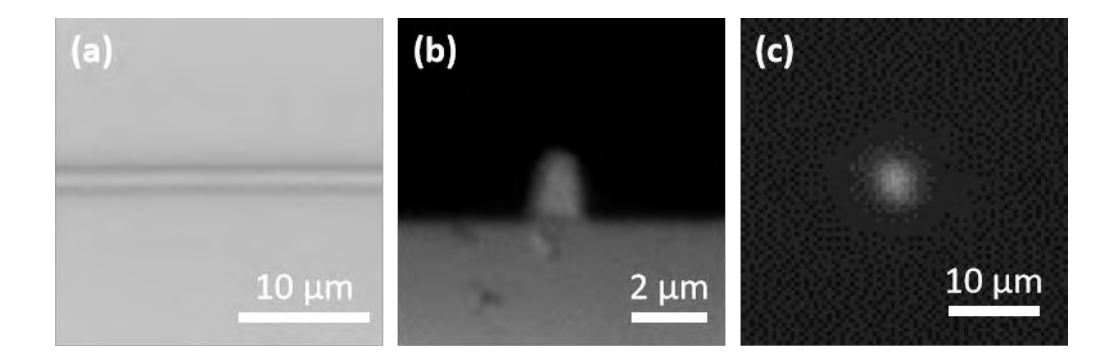


Figure 6.3. Microscope image of 2PP SU-8 waveguides produced using single-scan (a) top view, (b) side view, and (c) the respective near field image coupled with UHNA at 1550nm.

The microscope images of the waveguide fabricated using laser power of 180 mW and a scan speed of 8 mm/s are shown in Figure 6.3. The top view image in Figure 6.3(a) shows that the straight waveguide exhibits good uniformity along the waveguide axis. The cross-section of the input facet of the same waveguide is shown in Figure .3(b). It is observed that the height of the waveguide follows the thickness of the spin-coated SU-8 layer (1.8  $\mu$ m), whereas the width is 1.3  $\mu$ m with a side wall angle of ~70°. Insertion loss measurement was carried out to assess the performance of the waveguide. A 1550 nm continuous wave laser was butt-coupled into the waveguide (n<sub>core</sub> = 1.58) using ultrahigh-numerical-aperture (Nufern UHNA4) fibers. An objective lens (0.65 NA) was used at the waveguide output facets to collect the output power to an optical power meter. It is found that the straight waveguide exhibited high insertion loss at 14.5 dB. The majority of the coupling loss was attributed to the core diameter mismatch and NA mismatch, which is approximately 10 dB. Assuming an extra 2dB loss is due to the unpolished surface of the cleaved polymer surface at the input/output facets (Wu et al., 2016), the propagation loss of the waveguide is approximately 1.6 dB/cm, which is comparable to the SU-8 waveguide fabricated using the conventional UV-lithography method (Hamid et al., 2015).

### 6.2.3 Double-Scan Waveguide Writing

High waveguide loss was attributed to the core diameter and NA mismatch losses at the fiber-waveguide coupling. The coupling fiber has a core diameter of 2.2  $\mu$ m, which is about 2-fold larger than the waveguide width (1.3  $\mu$ m). Therefore, the waveguide width was enlarged by employing a double-scan technique. Double-scan or multiple-scan is an established waveguide fabrication technique for waveguide shaping in polymer and dielectric glasses (Liu et al., 2004; Nasu et al., 2005; Psaila et al., 2006; Suriano et al., 2011). This technique involves repeating the laser translation along the same scanning path, with slight lateral displacement if necessary. It is important to study the optimal center-to-center distance, d, between the waveguides to obtain the optimum displacement for enlarging the waveguide. A small displacement will not have significant increment in the waveguide dimensions, whereas large displacement might cause the separation of the waveguides. Therefore, an experiment has been carried out by increasing d from 0.2  $\mu$ m to 3.0  $\mu$ m to investigate the optimal displacement for creating waveguide with minimal coupling loss.

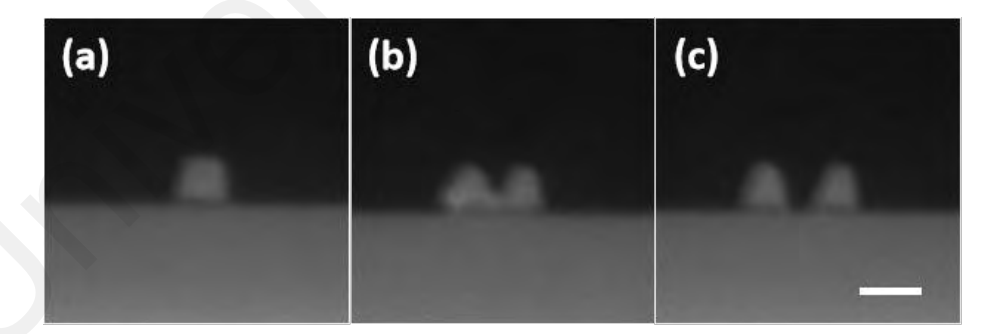


Figure 6.4. Double scan waveguide with center-to-center spacing of (a) 0.4, (b) 2.2, and (c) 2.6  $\mu$ m. The scale bar is 2  $\mu$ m.

The microscope images of the double-scanned waveguide are illustrated in Figure 6.4. It is shown in Figure 6.4 (a) that the waveguide width has slightly expanded to around 1.5 µm by employing double-scan technique with a spacing of 0.4 µm. However, when the waveguide spacing was increased to 2.2 µm, the double-scanned waveguide began to

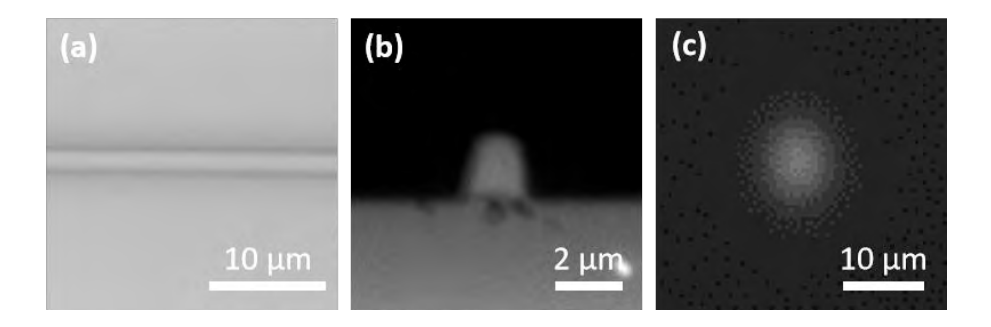


Figure 6.5. Double scanned waveguide with a center-to-center spacing of 0.8 μm. (a) Top view, (b) cross-section, and (c) the near field images near field image obtained when coupled with UHNA at 1550nm.

exhibit a sign of splitting. The splitting became more pronounced as the spacing was further increased, and the waveguides completely separated from each other when the center-to-center spacing increased to 2.6 µm.

Insertion loss measurements revealed that waveguide fabricated with  $d=0.8~\mu m$  exhibits the minimal optical loss. With this value of d, the waveguide width increased from 1.3  $\mu m$  to 1.8  $\mu m$  resulting in a reduction of the total coupling loss to 7.1 dB. Consequently, the insertion loss and propagation loss of the SU-8 waveguide fabricated using the double-scan technique improved to 11 dB and 1.27 dB/cm, respectively. Notably that the large excess loss is mainly due to NA mismatch as the current SU-8 waveguide structure is surrounded by air on its top and sides, resulting in a high NA value of approximately 1.2. This is not an issue in actual device fabrication such as photonics integrated circuits where individual device circuits are connected by the same waveguide structures and the waveguides are covered with cladding – instead of air - that will result in significantly improved NA mismatch loss.

To verify that the SU-8 waveguides produced only support the fundamental spatial mode at 1550 nm, the near field image of the waveguide output is projected to an IR CCD (Electrophysics Microviewer 7290A) using an objective lens (0.65 NA). The input

coupling fiber is then slightly misaligned in the horizontal and vertical axes in an attempt to excite higher order spatial modes. Figure 6.3 (c) and Figure 6.5 (c) show the near-field image of waveguide written using both single-scan and double-scan technique. It is clearly observed that both single-scan and double-scan waveguide will only excite fundamental at 1550 nm, showing that the fabricated waveguide is a single-mode waveguide.

## **6.3 Directional Couplers**

To demonstrate the viability of laser direct written single mode SU-8 waveguide in device application, a directional coupler (DC) structure has been fabricated. An optical DC is typically made by combining two or more individual optical waveguides. In general, the design of an optical DC includes input waveguides, a coupling region, and the output waveguides. Optical signals can be coupled into the device through one of the input waveguides, following an S-bend structure to the coupling region. In the coupling region, the input waveguide is positioned closely to another waveguide, allowing the optical power transfer between them. Depending on the coupling efficiency, the input signal will be divided into the output ports in a predetermined ratio. There are various designs for the directional coupler such as X-coupler, Y-coupler, or the combination of both, resulting in a complex coupler with multiple input and output ports. In this work, the basic X-shaped directional coupler is fabricated, which provides a 50-50 coupling ratio. The schematic diagram of the DC structure can be found in Figure 6.7.

#### 6.3.1 S-bend Simulation

S-bend serves as a critical component within a directional coupler, playing a pivotal role in guiding light either towards or away from the coupling region, while maintaining

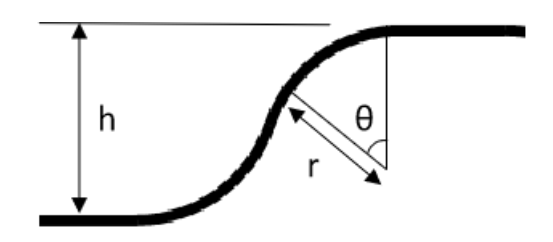


Figure 6.6. S-bend.

a reasonable separation between individual waveguides to prevent unintended coupling. Typically, the S-bend structure consists of two connected curves bending in opposite directions. Key parameters for characterizing the S-bend design include the bending radius, r, and bending angle,  $\theta$ , which directly influence the bending loss, L.

To optimize the S-bend design and minimize the bending loss, a simulation was performed using Rsoft, a widely used software that employs the Beam Propagation Method (BPM) to simulate optical waveguides. By adjusting the values of r and  $\theta$ , it is possible to determine the obtain the optimal parameters to fabricate an S-bend with minimal optical loss. The separation distance, h between the input and output waveguides can be expressed as  $h = r(1 - \cos \theta)$ . In this study, the value of h was maintained at 50  $\mu$ m. This is to ensure that the distance between the input waveguides in the final design remains fixed at 100  $\mu$ m.

The simulation results have provided valuable insights into the relationship between the bending loss and the radius of curvature. As illustrated in Figure 6.7, the findings demonstrate a consistent trend: as the bending radius increases, the bending loss significantly decreases. Notably, the bending loss reaches its minimum at approximately 300 µm bending radius. This phenomenon can be attributed to the fundamental optical principle called "total internal reflection". When a waveguide undergoes bending with a small radius, the curvature causes the incident angle at the interface between the core and cladding to approach or exceed the critical angle. At this point, the optical signal can no longer be entirely confined within the core, resulting in partial or complete loss of the

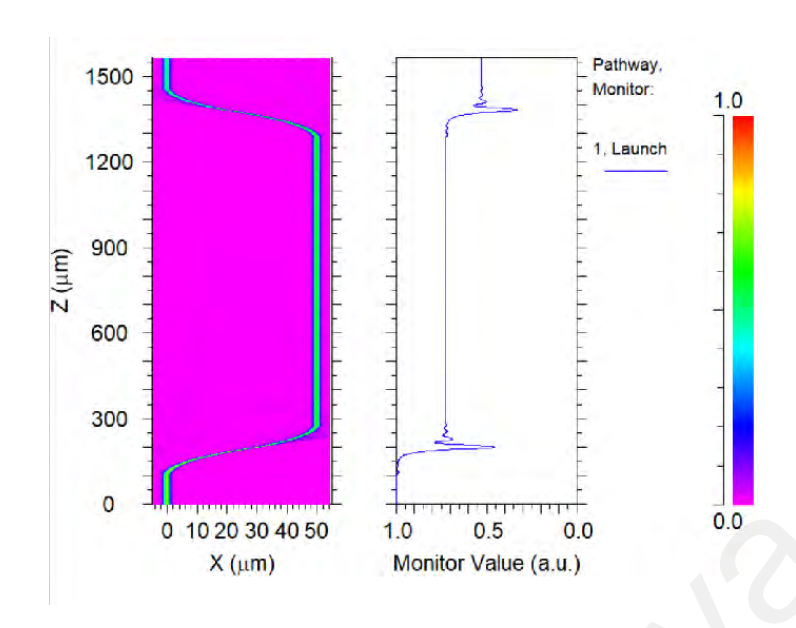


Figure 6.7. Bending loss simulation with Rsoft at  $r=200~\mu m$  and  $\theta=28.95^{\circ}$ . The monitoring graph on the right showing the S-bend exhibits a 50% bending loss.

signal as it leaks into the cladding. Conversely, when the bending radius is increased, the curvature becomes less pronounced. This ensures that the incident angle remains below the critical angle, allowing total internal reflection to be preserved. In the current study, this effect is particularly pronounced when the bending radius exceeds 300 µm (Figure 6.8). Consequently, the optical waveguide experienced a significant reduction in bending loss, revealing the threshold radius for minimizing the bending loss of the waveguide.

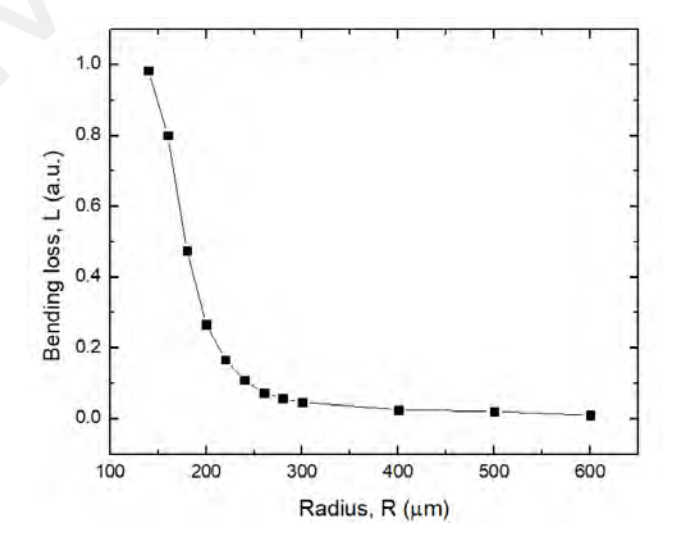


Figure 6.8. Simulation results showing the effects of bending radius to the bending loss of the S-bend. Waveguide width and height were 1.9  $\mu$ m and 1.7  $\mu$ m respectively.

## 6.3.2 Directional Coupler Simulation

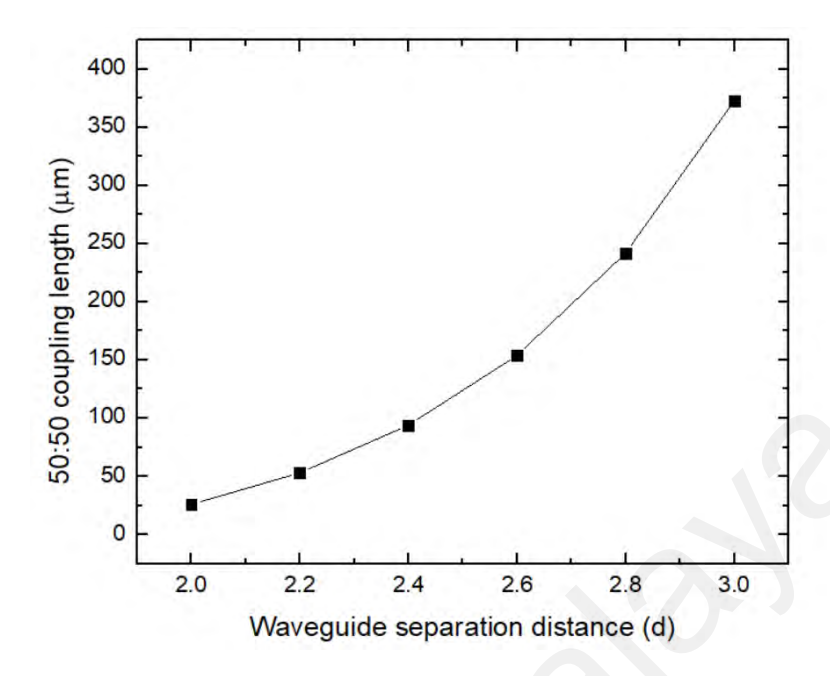


Figure 6.9. Variation of coupling length with the separation between two waveguides of a 50:50 directional coupler.

A directional coupler was designed and simulated using Rsoft to investigate the influence of waveguide separation distance on the coupling ratio (Figure 6.9). In a directional coupler, the transfer of optical power relies on the interaction of the evanescent fields of one waveguide with an adjacent neighboring waveguide. The distance between these waveguides directly affects the strength of this evanescent field interaction. When the waveguides are positioned closely, it leads to a stronger evanescent coupling, while greater separation weakens this interaction. Therefore, precise control over distance between the coupling waveguide is critical as it significantly impacts the coupling ratio.

The primary objective of this study was to design a DC that could achieve a 50:50 coupling ratio. To accomplish this required careful adjustments in two key aspects: the separation between the waveguides and the coupling length, which specifies the distance over which coupling occurs. In this work, the target for the coupling length was set at approximately 2.5 mm. This particular length was selected is to provide an interaction

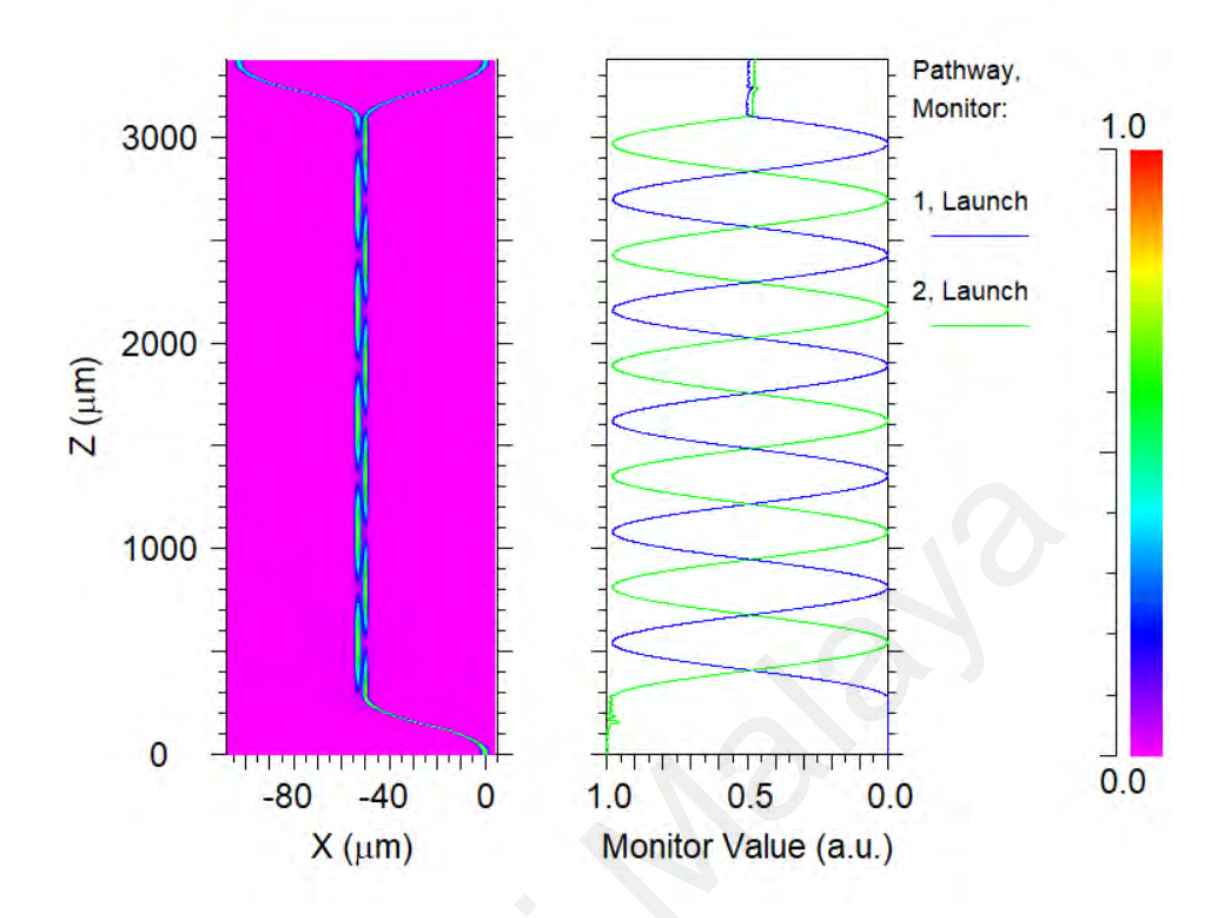


Figure 6.10. Simulation results for a 50:50 directional coupler. Coupling length: 2.6 mm, waveguide separation distance: 2.8  $\mu$ m; waveguide width: 1.9  $\mu$ m, waveguide height: 1.7  $\mu$ m.

distance that would be suitable for a range of applications. One of the applications of interest was the incorporation of nonlinear materials onto the DC structure to create a passive optical waveguide. This is significant because the interaction length plays a crucial role in the performance of such devices for application like signal processing and nonlinear optical effects. By taking into account of all the considerations, a 50:50 DC with an coupling length of 2.6 mm at a waveguide separation of 2.8 µm was simulated (Figure 6.10). This design aimed to provide the desire balance in power coupling between the waveguides, making it well-suited for application that require equal division of optical power.

### 6.3.3 Directional Coupler fabrication.

Following the simulation parameters, an actual DC was fabricated. The fabrication process was carried out using a computer-controlled 2-axis translational stage (Newmark). The stage motion was predefined with a self-written programming code using the DMC language by GalilTools. The design of the directional coupler was based on the simulation results (Table 1) and encoded into the programming code. The stage will follow in the programmed path, allowing femtosecond laser to induce photopolymerization in the SU-8 thin film for the creation of the DC structure. The waveguide fabrication employed the optimal laser writing parameters from the planar waveguide fabrication, in which the laser power and sample scanning speed employed were 180 mW and 10 mm/s, respectively.

Table 6.1. Directional coupler design parameters.

Design parameters	Value
Bending radius	400 μm
Bending angle	$20^{\circ}$
Coupling length	2600 μm
Waveguide separation distance	2.8 μm

Figure 6.11 presents the microscope image of the output branching of the fabricated DC structure. The actual fabricated DC features a core width and height of 1.9  $\mu$ m and 1.7  $\mu$ m, respectively. To assess the performance of the DC, coupling ratio has been calculated. Coupling ratio is a measure of how power is distributed within the DC. It is defined as the power at the through-port  $P_2$ , normalized to the total power of port  $P_2$  and  $P_3$ ,  $CR = P_2/(P_2 + P_3)$ . The "through-port" refers to the waveguide port through which the light or signals are transmitted without being coupled to the other port or known as the "cross-port". The cross-port coupling ratio can be obtained by the relation of (1 - CR), showing how much of the light signals are coupled to the other ports.

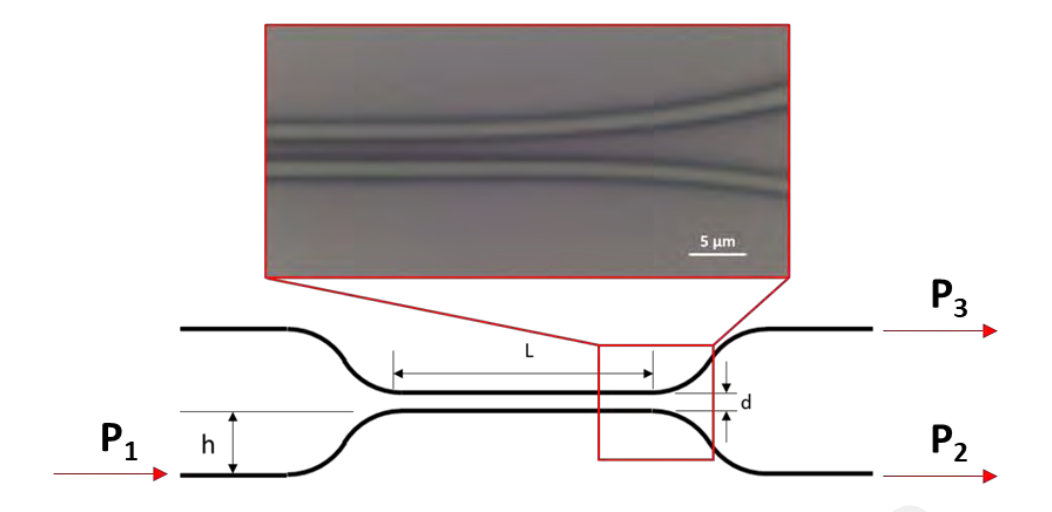


Figure 6.11. Schematic diagram of the design of the directional coupler, and the microscopic image of the direct laser written directional coupler. Symbol L, d, and h indicate the coupling length, waveguide gap distance, and the center to branching distance. In the experiment, L, d, and h are set to 2600 $\mu$ m, 2.8 $\mu$ m, and 50 $\mu$ m respectively.

It was found that at a waveguide gap distance of 2.8  $\mu$ m, the coupling ratio of the through port and cross port was measured to be ~47% and ~53%, respectively. These numbers indicate that the power is evenly distributed between the two ports of the directional coupler, allowing the application for 50:50 coupler. It is notable that these experimental results closely match the theoretical simulation results which suggested a 50:50 power splitting ratio, indicating that the device is performing as expected based on the theoretical model.

## **6.4 3D Standing Waveguide**

Another advantage of DLW is it offers a significant advantage in the creation of 3-dimensional (3D) micro-structured waveguides, expanding the potential for waveguide applications. This capability to work in three dimensions unlocks various possibilities, one of which is the development of vertical or suspended waveguides. These specialized

waveguides allow specific sections of the waveguide to engage with their surroundings environment. In this particular section of the waveguide writing in SU-8 photoresist, the fabrication of a suspended waveguide has been presented. These standing waveguides have a unique feature where the middle part of the waveguide is elevated, in this work, 10 µm above the substrate's surface. This elevation serves to isolate the suspended waveguide from the surface's waveguide, facilitating individualized interactions between the suspended waveguide and their surroundings within the selected region. The ability to control the length of these suspended waveguides opens up opportunities for application where precise interaction length with the material is of paramount importance.

# 6.4.1 3D standing waveguide design



Figure 6.12. Schematic diagram for the standing waveguide design.

Figure 6.12 presents the proposed design for the 3D standing waveguide, which consists of 2 parts: the surface waveguide and the suspended waveguide. The elevated or suspended section of the waveguide is connected to the surface waveguide through the implementation of a vertical S-bend structure. This elevation of the suspended waveguide is achieved through the creation of supporting pillars, which can be produced using the vertical writing technique. These supporting pillars are strategically positioned at the junction where the suspended waveguide and the S-bend structure meet. The precise placement of these pillars is of utmost importance as any misalignment could result in the collapse of the suspended waveguide (Figure 6.13). Another scenario that can result in the collapse of the suspended waveguide is if the heigh of the support pillars does not

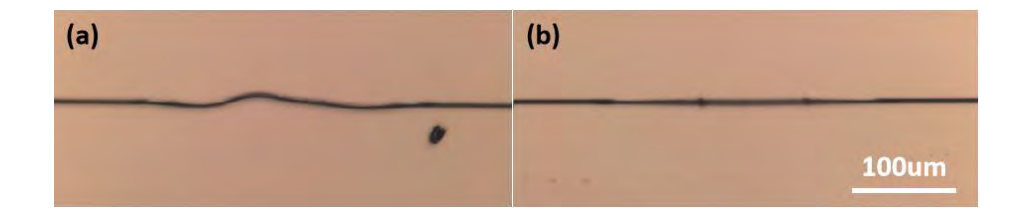


Figure 6.13. Top view of the fabricated suspended waveguide: (a) The suspended waveguide collapses due to the absence of the supporting pillars, (b) the waveguide is nicely suspended between the S-bend with the help of supporting pillars.

reach the same level as the suspended waveguide. Therefore, ensuring accurate alignment and positioning of these pillars is essential to maintain the structural integrity and functionality of the suspended waveguide.

#### 6.4.2 Fabrication

To accommodate the required height of the 3D structure, a thicker film was necessary. In this case, SU-8 2010 was used instead of SU-8 2002. The reason for this choice was the higher viscosity of SU-8 2010 allowed for the formation of a film that was 15 μm thick. Due to this increased film thickness, the process of soft-baking and pose-exposure bake for this sample required a longer duration compared to the thinner films. The baking procedure involved 15 minutes at 65°C, followed by an additional of 30 minutes at 95°C. Touch the edge of the substrate after baking the sample to check for stickiness. A sticky resist is an indication that it is under-baked, and it is required to extend the baking time.

The laser writing process for creating the suspended waveguide was similar to the fabrication of the planar waveguide, but with some notable differences. In this case, the standard objective lens was replaced with an aspheric objective lens that had a higher focusing power (40x, 0.65 NA). The use of a higher NA objective lens was essential to reduce the size of the voxel. A larger voxel would result in the formation of the suspended

waveguide being larger than the intended dimensions. Therefore, by using a high NA lens, the laser spot could be more precisely controlled, ensuring the waveguide's dimensions met the desired specifications. In this case, the spot diameter is 1.4 µm in free space. In addition, the translational stage employed in this work was substituted with a 3-axis translational stage by Vexta. This 3D translational stage allowed for precise 3D motion during the creation of the suspended waveguide. The stage was controlled by a steppermotor controller (D220), where the motion path was pre-programmed by using Labview. Detailed information about the experimental setup can be found in Chapter 3.

### 6.4.3 Characterization and Analysis

The fabrication parameters were based on the optimal parameters obtained from the planar waveguide writing in Section 6.3, where the laser power was set to 180 mW and 2 mm/s translational speed. The surface waveguide fabricated by focusing the laser on the substrate, then the focal spot gradually moves away from the substrate surface to create the suspended waveguide. It was found that the surface waveguide exhibits a similar dimension with the one obtained in the previous experiment. However, as the focal spot moved closer to the surface of the photo resist film, the photoresist was burnt and induced collateral damage to the surrounding. The experiment was repeated by reducing the laser power while keeping the same translational speed. As a result, it was found that the damage during suspended waveguide writing occurred at laser power higher than 50 mW (Figure 6.14). The outcome of this experiment presented a different trend with the threshold fluence obtained in the previous experiment.

To investigate this phenomenon, two possible reasons were evaluated to justify the observation. While the first possibilities take into account the depth-dependent spherical aberrations, and the second one considers the beam truncation of the focus spot. It is



Figure 6.14. Laser induced-damage during suspended waveguide writing.

commonly known that spherical aberrations will occur when light focused from one medium into another medium of different refractive index. The difference in the angle of refraction between the marginal rays and paraxial light rays at the interface between two mediums will cause a shift in the focal position, thereby creating a focal spot that elongates along the optical axis. Spherical aberrations not only distort the pulse shape, but also distort the intensity distribution of the focused laser beam. Huang et al presented a 60% drop in the focal intensity when the laser beam is focused to a depth of 400 μm. This implies that the modification threshold power is a variable that changes with the focus depth. Higher power is required to induce modification at a greater depth to compensate for the reduction in the peak intensity due to spherical aberrations. Employing the explanation to the current study will find that the threshold fluence for surface waveguide and suspended waveguide writing are potentially different. Therefore, the fluence used for surface waveguide writing could exceed the damage threshold for suspended waveguide writing, consequently damaging the photoresist. However, from the same report it can be seen that spherical aberrations effect only become significant when the focusing depth is greater than 50  $\mu$ m when focusing with high NA (>0.5) objective lens. Therefore, it is believed that spherical aberrations play a small or insignificant role for the current observation.

It is believed that beam truncation is a more accurate explanation when discussing the variation of the threshold fluence at different focus depth. Sun *et al* reported an interesting

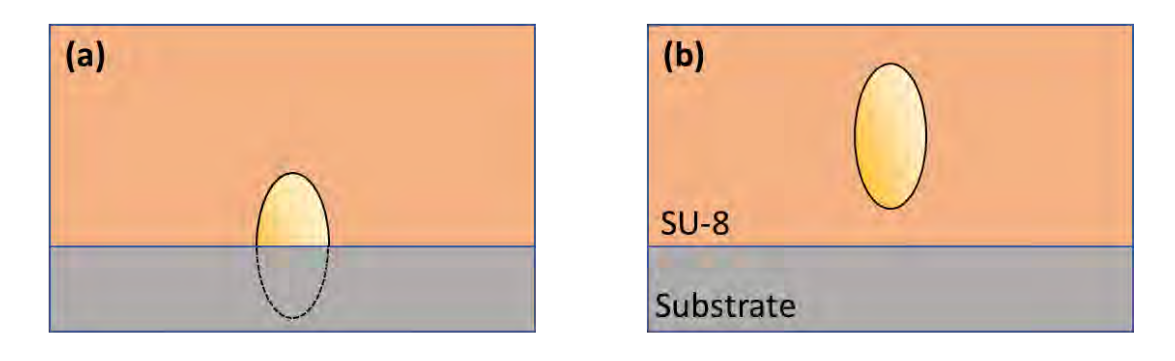


Figure 6.15. Schematic diagram of the voxel shape and size variation when focusing on (a) surface of the silicon wafer, and (b) in the SU-8 film.

phenomenon by ascending the center of the laser voxel from the below to above the surface of the substrate during the 2PP process (Sun & Kawata, 2003). They showed that the dimension of the voxel increases as the center position of the voxel is located about the substrate surface, demonstrating that beam truncation plays an important role in controlling the shape and size for 2PP at the material interface. Back to the current study, the laser beam is focused on the silica-SU-8 during the surface waveguide writing. At this point, the lower part of the focal spot overlaps with the substrate, whereas the top part is exposed to the photoresist as shown in Figure 6.15. Consequently, the effective fluence for polymerization is greatly reduced. As the focus spot moves away from the surface, the volume of the voxel interacting with the photoresist gradually increases, eventually reaching to the maximum fluence as the entire voxel emerged into the photoresist (Figure 6.15 (b)). Therefore, the effective fluence appeared differently in both cases due to the position of the focal spot. When the laser focal spot is near to the surface of the substrate, the effective fluence is significantly reduced, enabling stable 2PP process without damage. Conversely, the effective fluence gradually increases by reducing the focus depth, leading to a greater amount of energy being deposited into the photoresist. As the energy absorbed exceeds the damage threshold, the strong optical absorption leads to a significant accumulation of thermal energy, ultimately damaging the photoresist.

From here, it can conclude that effective fluence is a more accurate description than the spot fluence when discussing modification threshold at different focus depth. However, it is challenging to accurately quantify the effective fluence as the overlapping condition between the voxel and the substrate cannot be precisely determined. A rough estimation of the effective fluence,  $F_{eff}$  can be obtained by taking the product of the total fluence, NF with the remaining portion of the truncated focus spot, k. For instance, assuming only the top half of the focal spot (k = 0.5) was interacting with the SU-8 during surface waveguide writing, the effective fluence is then evaluated as 0.5 NF. However, it is important to note that it is challenging to accurately quantify the effective fluence as the value for k cannot be precisely determined. The measurement required high resolution laser beam alignment and focal spot imaging system to qualitatively analyze the shape and size of the focused laser beam. As for this thesis, both effective fluence and total fluence will be described as "fluence" for simplicity.

To prevent damage during the suspended waveguide writing, it is essential to utilize a significantly reduced laser power during the laser processing. To compensate for the decrease in laser power, the translational speed was concurrently reduced while maintaining a sufficient laser fluence for 2PP. By systematically adjusting both parameters, it was found that the suspended waveguide can be fabricated when the laser processing power is reduced to below 40 mW. When the laser writing power is higher than 50 mW, the SU-8 is easily damaged across the range of translational speed tested in the experiment (0.5 mm/s - 2 mm/s). To account for the reduced laser power, the translational speed is concurrently reduced to 50  $\mu$ m/s to maintain sufficient fluence for complete 2PP process. Increasing the speed will give rise to lower fluence for 2PP, while lowering down the speed will induce damage during the suspended waveguide writing. Therefore, there is a narrow processing window in order to balance the fabrication for both surface and suspended waveguide.

The standing waveguide structure was presented in Figure 6.16. The SEM image was taken from an inclined angle to observe the side view of the structure. In the figure consists of 5 standing waveguides that was fabricated under the same fabrication parameters. The overall view of the standing waveguide can be found in Figure 6.16 (a). The elevation of the surface waveguide into the suspended waveguide can be clearly observed in the figure, with a slanted structure connecting both waveguides which is the S-bend. A closer look at the suspended waveguide revealed that it is lifted from the surface by approximately 5 µm above the substrate surface, with the help of two supporting pillars.

To further characterize the fabricated structure, the dimensions of the suspended waveguide were measured. The width of the suspended waveguide was approximately 2  $\mu$ m, which is similar with the width of the surface waveguide. This implies that the lateral size of the voxel is consistent and independent within the range of focal depth involved in this experiment. On the other hand, the height of the suspended waveguide achieved 15  $\mu$ m, which is 10-folds larger than the expected focal spot diameter (1.4  $\mu$ m). It was explained previously that spherical aberrations play an insignificant role in this work due to the shallow focusing depth. Therefore, it is more realistic to consider heat accumulation effects as the primary factor that causes the enlarged dimensions.

Heat accumulation effect is a common phenomenon when doing laser processing with high repetition rate laser. It occurs when the temporal distance between successive pulses is shorter than the material cooling time, therefore the thermal energy does not have sufficient time to escape from the focal spot before the arrival of the subsequent pulses. Material cooling time,  $\tau_c$  can be evaluated with  $(2\omega_0)^2/\chi$ , where  $\chi$  is defined as the material diffusivity. Assuming the heat diffusivity of this study is similar to the reported value in the literature, the value for  $\chi$  of SU-8 falls within the range of 0.11 – 0.16 mm<sup>2</sup>/s (Erfantalab et al., 2022). This implies that SU-8 exhibits a long cooling time of 14-20  $\mu$ s. As the temporal distance for an 80 MHz pulsed laser is 12.5 nJ, this implies that over

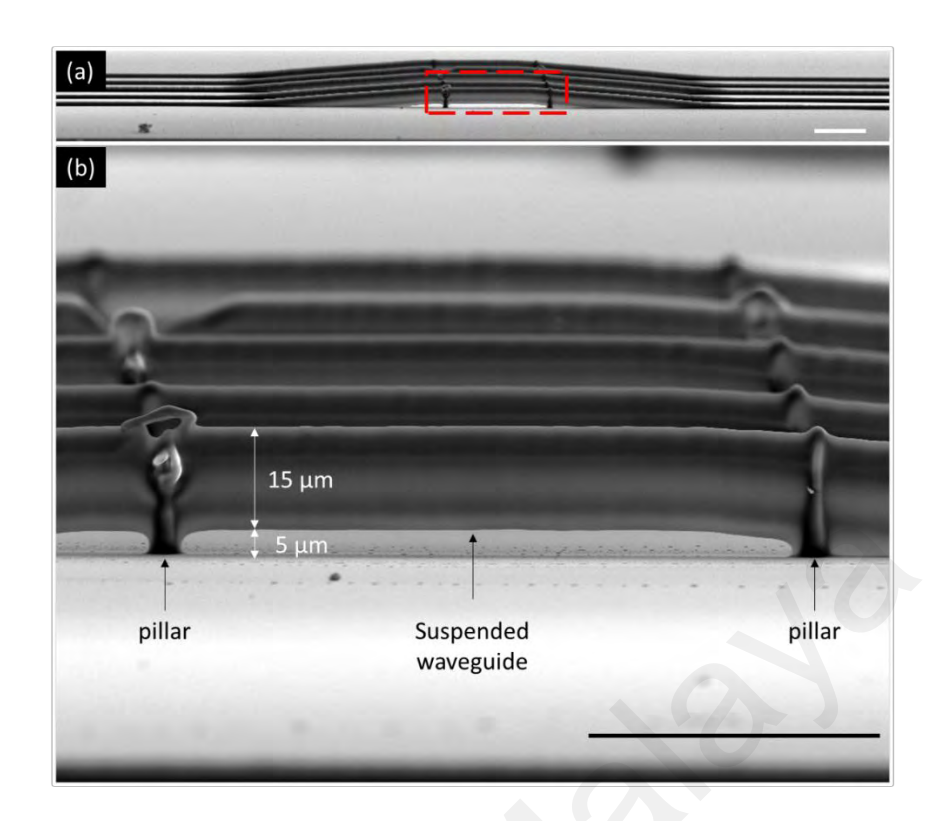


Figure 6.16. SEM images of the air-suspended waveguide (a) overview, and (b) close-up image of the area indicated by the red square in (a). The scale bar is  $50 \mu m$ .

According to the simulation result of Ijppal *et al*, the increased in local temperature enhances the decomposition of photoinitiator into the free radicals. During the polymerization reaction, the free radicals then diffuse out from the focal spot to combine with other monomers to form a larger polymer molecule. The radical diffusion direction and the covered volume will then define the size of the polymerized voxel. Therefore, the final dimension of the voxel will tend to be larger than the initial focal spot diameter.

With that, it is intuitive that the dimensions of the waveguide can be easily manipulated by varying the laser power or the fluence. However, variation in the laser writing conditions would affect the dimensions of the surface waveguide. Therefore, the laser writing power and the scanning speed should be adjusted with the focus depth during the laser writing process to obtain a homogenous dimension for the entire standing waveguide structure. Unfortunately, the current laser writing system does not exhibit such technology.

The laser power controller cannot be synchronized with the moving stage, thus the laser power cannot be precisely manipulated with the focus depth. On the other hand, high scanning speed will result in the deformation of the structure due to the stage overshooting while moving at high speed. With all technical limitations, the waveguide structure cannot be further improved until the writing system is upgraded.

# 6.4.4 Optical Characteristics of Suspended Waveguide

Although the standing waveguide structure is not optimized, optical characterization was conducted to investigate the performance of the structure in its current form. By employing similar measurements technique as the previous experiment, the insertion loss of the standing waveguide was evaluated. Insertion loss of the suspended waveguide was measured to be around 16 dB, which is 5 dB higher than the straight waveguides. The excess insertion loss in the suspended waveguides can be attributed to the waveguide dimension mismatches at the two supporting pillars and between the surface waveguide and the suspended waveguide section. It can be observed in Figure 6.16 (b) that the width of the waveguide at the intersections between the pillars and waveguide is significantly enlarged due to the multiple exposures at these regions during the waveguide writing. The height mismatch between the surface waveguide (3.6 µm) and suspended waveguide (15 μm) also gives rise to the mode mismatch when the light propagates in the waveguide. The dimensional mismatch can be improved using automated laser power and translational speed variation during the suspended waveguide writing. To obtain a suspended waveguide with smaller dimensions that match the surface waveguides, an objective lens with higher NA together with automated laser power and variable translation speed can be used.

These results show that the proposed 2PP fabrication technique can be used to create a 3D optical waveguide, where at the same time as an alternative for suspended waveguide fabrication. In the previous report, suspended waveguide fabrication usually involves a complicated fabrication process i.e., stamp transfer and plasma etching. Christoph et al presented a single-mode air-suspended rib waveguide by sealing the air cavity on KMPR using a SU-8 thin film transferred from a PDMS stamp (Prokop et al., 2015). By using a similar approach, they successfully fabricated an air-suspended waveguide grating with a coupling loss of 8 dB with the single-mode fiber (Prokop et al., 2016). Aleksandrs M. et al demonstrated high refractive index contrast air-suspended SU-8 waveguide by plasma etching. The free-standing SU-8 waveguide was supported by thin pillars, where the SiO<sub>2</sub> underneath was removed by plasma etching (Marinins et al., 2016). These methods are indeed promising, however, the process is complicated and requires high accuracy in sample positioning. Femtosecond laser direct writing, on the other hand, allows in-situ rapid fabrication of complicated 2D/3D waveguide with computer-controlled waveguide design. Therefore, the current work demonstrated femtosecond laser writing as a potential approach to creating air-suspended waveguides for high-level 3D optical devices.

## 6.5 Conclusion

Single mode SU-8 waveguides were fabricated via 2PP using 780nm femtosecond laser writing. It was found that the laser fluence required to polymerize SU-8 varied between 1.8 kJ/cm² and 10 kJ/cm², whereas complete polymerization to create a flat top surface waveguide is dependent on the thickness of the SU-8 film. In our work, 2.5 kJ/cm² was the optimized laser fluence for creating a flat top surface waveguide for a 1.8 μm thick SU-8. The insertion loss of the waveguide is 14.5 dB with an estimated propagation loss of about 1.6 dB/cm when coupled with UHNA at 1550 nm. The waveguide losses were

able to be reduced using the double scan technique during the fabrication process, where the optimized waveguide has an insertion loss and propagation loss of 11 dB and 1.27 dB/cm at 1550nm, respectively. Using similar fabrication parameters, a directional coupler was fabricated. The coupling ratio of the fabricated directional couple was 47% and 53% for each output port, which agrees well with the theoretical value. To further showcase the potential of creating a complex waveguide structure in SU-8 using the femtosecond laser direct writing technique, a suspended waveguide had been fabricated, where a straight channel waveguide resting on top of multiple supporting pillars. Despite still having a high insertion loss of 16 dB, the suspended waveguide is the best proof of concept in realizing 3-D optical waveguide for high-level photonics integrated circuits. The high insertion loss is attributed to the non-optimized coupling between the surface waveguides and the suspended waveguide, which could be improved with a high NA objective lens, automated laser power and translation speed variation during the laser writing process. The outcome of this work can be used to extend the application of DLW SU-8 via 2PP to the fabrication of 2.5D and 3D multifunctional waveguide structures(Gehring et al., 2019; Schumann, Bückmann, et al., 2014b; Xu et al., 2018a).

# **CHAPTER 7**

#### CONCLUSION AND FUTURE WORKS

#### 7.1 Conclusion

The investigation into the interaction of intense femtosecond lasers with transparent materials has been ongoing since the emergence of ultrafast femtosecond lasers. Despite the considerable research in this field, many aspects of the laser-matter interaction fundamentals remain unknown, leading to the primary objective of this thesis: gaining a comprehensive understanding of laser interactions with various transparent materials. In this concluding chapter, several key findings from the thesis will be reviewed and discussed, in combination with the potential future research directions.

Since the primary objective of this research is to investigate the nonlinear interactions between high repetition rate femtosecond with various transparent material, three materials have been studied, namely soda-lime glass, CR-39, and SU-8, in Chapter 4, 5 and 6, respectively. The use of high repetition rate for material modification had resulted in rapid and intense heat accumulation at the laser voxel, which affects the quality of micro-processing in these materials in many ways. Expansion or the enlargement of the modification area due to heat accumulation effects had been observed during DLW in these materials. This phenomenon will result in the poor fabrication resolution. On top of that, heat accumulation effects could also induce irreversible thermal damage in the material if it is not carefully controlled. Therefore, the main outcome of this research showed that heat accumulation effect is one of the biggest challenges when carrying out DLW using high repetition rate laser, and it is important to precisely control the laser processing parameters i.e. laser power and sample scanning speed to produce the desired structure, improving the fabrication quality, and preventing the unwanted damage to the material. Understanding the optimal laser writing parameter resulted in the fabrication of

optical waveguide with high repetition rate laser without inducing any damage to the material. The results are presented in Chapter 4 - 6 in the thesis.

Chapter 4 presented a thorough study of DLW in soda-lime glass to establish the foundation of this laser processing technique. Soda-lime glass waveguide was fabricated by tightly focused 515 nm femtosecond laser within the bulk glass. Several laser parameters were varied during the laser writing process including the pulse energy and sample scanning speed. Cross-section imaging revealed that the modified structure exhibited an inverted tear-drop structure, where a large transparent region located above a narrow-damaged line. The formation mechanism of this structure was explained by the ion migration due to the thermal gradient created by the high energy pulse laser during the laser writing process. The experiment found that the heat accumulation effect was a complex interplay between the pulse energy and the sample scanning speed. For instance, strong heat accumulation effects were only observed when the pulse energy is above 3 µJ and the sample scanning speed is below 0.5 mm/s. The outcome of this research provides a valuable insight where careful control of the laser writing parameters could minimize the thermal accumulation, thereby creating a more localized modification in soda-lime glass.

Several optical characterization approaches have been used to study the optical performance of the soda-lime glass waveguide. With the help of beam profile analysis and several mathematical calculations, it is found that the waveguide core achieved a high index contrast of 4.7 x 10<sup>-3</sup>, together with a high NA of 0.148. Despite having high CTE value which is usually avoided in the DLW experiment, the outcome of this work showcased the potential of soda lime glass for its application as optical waveguide. However, the reason behind the high index contrast as compared to other reported work remains unknown. A possible reason is the interaction between the glass composition to the writing wavelength, however, the current facilities in the laboratory don't have

another femtosecond laser at other wavelengths with similar pulse energy level. Therefore, the investigation on the effects of wavelength to the direct laser writing is not possible at the moment.

On the other hand, the soda-lime glass waveguide facilitates high propagation loss and coupling loss. The reason of the high coupling loss was found to be the elliptical mismatch between the coupling fiber and the fabricated waveguide. To solve this problem, the voxel of the writing laser has to be reshaped by using slit beam shaping method, to create a more spherical waveguide core. In contrast, the high propagation loss is attributed to the inhomogeneity of the glass components. Soda-lime glass consists of several components such as K, Na, Ca, and etc. The migration and redistribution of these ions helps in the formation of the high index waveguide core as discussed in the chapter, however, the accumulation of the ions creates scattering point where the light propagated within the waveguide core will be scattered, resulting in the high propagation loss. In the future, the research should be repeated with soda-lime glass of different doping levels for each ion, to find out the contribution of each ion towards the scattering. By comparing the effects of each ion to the performance of the waveguide, soda-lime glass could be a cheaper alternative than fused silica in the application of optical waveguide fabrication.

Laser processing in thermoset plastics was presented in Chapter 5. With the aim of investigating the modification characteristics of CR-39 with high repetition rate laser, a high repetition rate femtosecond laser was employed to induce modification within bulk CR-39 at varying focus depth. It was found that laser processing in CR-39 couldn't induce continuous modification due to the irreversible curing of thermoset plastics. When the laser focused within the bulk, the strong heat accumulation effects cause expansion of the material, inducing a large heat affected zone. As the laser focus moves to the surface of the material, however, the melted material at the laser focus spot can now escape to the air, leaving behind a void/trench on the surface. In this case, a continuous structure was

created, which is a phenomenon not observable when the laser is focused within the bulk. The outcome of this research provides a valuable insight where the material modification could exhibit different behavior with the variation of the laser focus depth. By carefully controlling the focusing depth, the material could be functionalized to the desire applications. For instance, bulk modification of CR-39 could be applied as a memory device, owing to the spot-by-spot modification structure, whereas surface ablation of CR-39 could find applications in microfluidies.

Following that, an experiment was conducted to investigate the existence of plasma shielding during surface ablation. By employing nitrogen purging techniques, the ablation efficiency was successfully enhanced by removing the plume in front of the laser focus spot. However, it was found that the ablation depth saturated when the pulse number increases up to 4 x 10<sup>5</sup>, indicating that plasma shielding wasn't the only reason of the low ablation efficiency. Further investigation with SEM found that it was thermal reflow around the ablated region that causes the light scattering, thereby reducing the effective laser intensity for further ablation. Due to the phase changes of the target surface, the beam profile of the focused laser beam was distorted, resulting in the reduced ablation effect. This effect was not a significant factor in the work described in this thesis, as surface ablation wasn't the main concern. However, any future work that relies on surface ablation may require an in-depth study to enhance the ablation depth and ablation rate.

It was shown in the previous chapter the implications of manipulating each laser processing parameter during laser writing to the structure and performance of the end product. In Chapter 6, the knowledge will be combined with the goal of fabricating a 3-dimensional waveguide. The chapter started with a basic straight channel waveguide writing. In this part of the experiment, a 2-D optical waveguide was fabricated using the SU-8 photoresist. The waveguide dimensions were controlled by manipulating the pulse energy, sample scanning speed, together with a newly introduced double scan technique.

By systematically varied the pulse energy and sample scanning speed, it was found that accumulated fluence plays an important role in two photon polymerizations. Below 1.8 kJ/cm<sup>2</sup> the laser fluence is inadequate to achieve complete polymerization, whereas above 10 kJ/cm<sup>2</sup> thermal damage occurs. Therefore, the outcome of this work provided the upper and lower limit of the laser fluence for doing laser processing in SU-8.

Next, a 3-D standing waveguide was fabricated. The standing waveguide structure consists of three different sections, namely the surface waveguide, suspended waveguide, and the supporting pillars. The realization of this structure is achieved by controlling the focusing depth of the laser during the laser writing process, where the laser focal spot is elevated from the substrate surface to create the suspended waveguide. Similar to the work presented in Chapter 5, elevating the laser focusing depth near to the surface of the SU-8 thin film will induce ablation, causing damage to the photoresist. In order to avoid damage, the focusing voxel was kept at a reasonable distance from the surface of the SU-8 film. The laser fluence was lowered down by adjusting the writing power to 40 mW and 50 μm/s sample scanning speed, while maintaining a sufficient laser fluence for complete polymerization. With these, a standing waveguide was successfully created. The middle section of the waveguide is lifted from the surface of the silicon substrate, with the help of two supporting pillars. It is found that there is an obvious dimensional mismatch between the suspended waveguide and the surface waveguide, which is attributed to the spherical aberrations. Due to the technical limitations, the dimensions mismatch wasn't able to be solved, leaving the waveguide with a high insertion loss of 16 dB. Despite the technical limitations, the outcome of this work demonstrated the potential application of DLW in creating 3D waveguide. Further work is definitely needed with better facilities such as a laser pulse energy controller with faster response.

#### 7.2 Future works

There are several future works that can be done for each experiment presented in Chapter 4 - 6. For the soda-lime glass waveguide writing, it was mentioned that the formation of the waveguide structure is due to the migration of ions that exist in the glass itself. The high propagation loss measured from the produced waveguide is due to the inhomogeneous ion distribution of the soda lime glass used. This can be improved by using soda-lime glass materials that have a more homogeneous distribution of the ions/impurities. The homogeneous ions/impurities distribution in the material will result in a uniform ion redistribution during DLW and therefore reduces the high propagation loss of the current waveguide.

For CR-39 laser processing, it will be interesting to further the study on the effect of laser writing directions on the produced structures. The current direct laser writing was done with transverse scanning, where the optical axis of the writing laser is perpendicular to the writing direction. In the future, the experiment could be repeated with longitudinal laser writing, where the optical axis of the laser is parallel to the laser writing direction. With this modification, the ablation depth should be able to significantly improve. Deeper ablation allows for more precise control over the depth and shape of the structure that could be used to create several applications. For example, ablation of two deep trenches with a spacing of few µm could potentially create a type II optical waveguide, where the waveguide mode is guided in between the trenches. On the other hand, by precisely shaping the trenches, it could be applied for microfluidic channel as well. Therefore, the capabilities to precisely control the depth and structure will definitely open up new possibilities for CR-39 in the fabrication of optical devices.

Lastly, for the standing waveguide fabrication experiment in SU-8, there are a few things that can be done to improve the structure. Variable laser power and scan speed can be used during the fabrication of different parts of the waveguide. This method will significantly improve the structure dimensions and minimize the current dimensional mismatch between the surface and suspended waveguide. The pillar spacing can also be optimized to better support the suspended waveguide. Once the fabrication process is optimized, complex 3D waveguide structures can be designed and fabricated using this method.

The results presented in this thesis contribute invaluable insights into laser-matter interactions and the optimization of laser processing parameters for the optical materials under study. While addressing specific challenges, it opens up possibilities for further research to enhance the understanding and application of femtosecond laser interactions in diverse fields.

#### REFERENCES

- Abou Khalil, A., Bérubé, J.-P., Danto, S., Desmoulin, J.-C., Cardinal, T., Petit, Y., . . . Canioni, L. J. S. r. (2017). Direct laser writing of a new type of waveguides in silver containing glasses. 7(1), 1-9.
- Adams, C. M., Hardway, G. A. J. I. T. o. I., & Applications, G. (1965). Fundamentals of laser beam machining and drilling. (2), 90-96.
- Adão, R. M., Alves, T. L., Maibohm, C., Romeira, B., & Nieder, J. B. J. O. E. (2022). Two-photon polymerization simulation and fabrication of 3D microprinted suspended waveguides for on-chip optical interconnects. 30(6), 9623-9642.
- Alauddin, M., Choudhury, I., El Baradie, M., & Hashmi, M. J. J. o. M. P. T. (1995). Plastics and their machining: a review. *54*(1-4), 40-46.
- Ali, A. S., Abdalla, M. D., & Adam, M. J. I. J. o. p. (2018). A study Optical and Physical Properties of Soda Lime Silica Glass Doped with ZnO. 6, 53-56.
- Ali, M. A., Rajabi, M., & Sali, S. S. J. C. O. i. C. E. (2020). Additive manufacturing potential for medical devices and technology. 28, 127-133.
- Allahyari, E., Nivas, J. J., Valadan, M., Fittipaldi, R., Vecchione, A., Parlato, L., . . . Amoruso, S. J. A. S. S. (2019). Plume shielding effects in ultrafast laser surface texturing of silicon at high repetition rate in air. 488, 128-133.
- Ams, M., Little, D., & Withford, M. (2012). Femtosecond-laser-induced refractive index modifications for photonic device processing. In *Laser Growth and Processing of Photonic Devices* (pp. 305-332). Elsevier.
- Andrásik, A., Flender, R., Budai, J., Szörényi, T., & Hopp, B. J. A. P. A. (2020). Processing of optical glasses by single, 34 fs pulses in the strong field ionization domain: ablation characteristics and crater morphology. *126*, 1-8.
- Archbold, E., Harper, D., & Hughes, T. J. B. J. o. A. P. (1964). Time-resolved spectroscopy of laser-generated microplasmas. *I5*(11), 1321.
- Ayoib, A., Hashim, U., Arshad, M. M., & Thivina, V. (2016). Soft lithography of microfluidics channels using SU-8 mould on glass substrate for low cost fabrication. 2016 IEEE EMBS Conference on Biomedical Engineering and Sciences (IECBES),
- Baghdasaryan, T., Vanmol, K., Thienpont, H., Berghmans, F., Geernaert, T., & Van Erps, J. J. J. o. P. P. (2021). Design and two-photon direct laser writing of low-loss waveguides, tapers and S-bends. *3*(4), 045001.

- Balena, A., Bianco, M., Pisanello, F., & De Vittorio, M. J. A. F. M. (2023). Recent Advances on High-Speed and Holographic Two-Photon Direct Laser Writing. 2211773.
- Baudach, S., Bonse, J., Krüger, J., & Kautek, W. J. A. s. s. (2000). Ultrashort pulse laser ablation of polycarbonate and polymethylmethacrylate. *154*, 555-560.
- Belaud, V., Valette, S., Stremsdoerfer, G., Beaugiraud, B., Audouard, E., & Benayoun, S. (2014). Femtosecond laser ablation of polypropylene: A statistical approach of morphological data. *Scanning*, *36*(2), 209-217. <a href="https://doi.org/10.1002/sca.21090">https://doi.org/10.1002/sca.21090</a>
- Bellec, M., Canioni, L., Royon, A., Bousquet, B., & Cardinal, T. (2008). 3D optical data storage using third-harmonic generation in silver zinc phosphate glass. 2008 Conference on Lasers and Electro-Optics and 2008 Conference on Quantum Electronics and Laser Science,
- Bhardwaj, V. R., Simova, E., Corkum, P., Rayner, D., Hnatovsky, C., Taylor, R., . . . Zimmer, J. J. J. o. a. p. (2005). Femtosecond laser-induced refractive index modification in multicomponent glasses. *97*(8), 083102.
- Biswas, S., Karthikeyan, A., & Kietzig, A. M. (2016). Effect of Repetition Rate on Femtosecond Laser-Induced Homogenous Microstructures. *Materials (Basel)*, 9(12). https://doi.org/10.3390/ma9121023
- Blömer, D., Szameit, A., Dreisow, F., Schreiber, T., Nolte, S., & Tünnermann, A. J. O. e. (2006). Nonlinear refractive index of fs-laser-written waveguides in fused silica. *14*(6), 2151-2157.
- Boudebs, G., & Fedus, K. J. J. o. A. P. (2009). Absolute measurement of the nonlinear refractive indices of reference materials. *105*(10).
- Bouras, N., Madjoubi, M., Kolli, M., Benterki, S., & Hamidouche, M. J. P. P. (2009). Thermal and mechanical characterization of borosilicate glass. *2*(3), 1135-1140.
- Brown, F., Parks, R. E., & Sleeper, A. M. J. P. R. L. (1965). Nonlinear optical reflection from a metallic boundary. *14*(25), 1029.
- Brown, M. A., Zappitelli, K. M., Singh, L., Yuan, R. C., Bemrose, M., Brogden, V., . . . Gardner, T. J. J. N. C. (2023). Direct laser writing of 3D electrodes on flexible substrates. *14*(1), 3610.
- Burakov, I. M., Bulgakova, N. M., Stoian, R., Mermillod-Blondin, A., Audouard, E., Rosenfeld, A., . . . Hertel, I. V. J. J. o. A. P. (2007). Spatial distribution of refractive index variations induced in bulk fused silica by single ultrashort and short laser pulses. *101*(4), 043506.

- Cao, C., Shen, X., Chen, S., He, M., Wang, H., Ding, C., . . . Interfaces. (2023). High-precision and rapid direct laser writing using a liquid two-photon polymerization initiator. *15*(25), 30870-30879.
- Chan, J. W., Huser, T. R., Risbud, S., & Krol, D. J. A. P. A. (2003). Modification of the fused silica glass network associated with waveguide fabrication using femtosecond laser pulses. *76*, 367-372.
- Chandrinos, A. J. J. o. M. S. R., & Reviews. (2021). A Review of Polymers and Plastic High Index Optical Materials. 7(4), 1-14.
- Chen, G. Y., Piantedosi, F., Otten, D., Kang, Y. Q., Zhang, W. Q., Zhou, X., . . . Lancaster, D. G. J. S. r. (2018). Femtosecond-laser-written microstructured waveguides in BK7 glass. 8(1), 10377.
- Cheng, G., Lin, L., Mishchik, K., & Stoian, R. J. M. (2022). Polarization-Dependent Scattering of Nanogratings in Femtosecond Laser Photowritten Waveguides in Fused Silica. *15*(16), 5698.
- Cheong, Y., Lim, W., Lee, S., Pua, C., Chong, W., & Ahmad, H. (2016). 405 nm laser processing of thin SU-8 polymer film. *J Optik*, *127*(4), 1651-1655.
- Chichkov, B. N., Momma, C., Nolte, S., Von Alvensleben, F., & Tünnermann, A. J. A. P. A. (1996). Femtosecond, picosecond and nanosecond laser ablation of solids. 63(2), 109-115.
- Chidambaram, N., Kirchner, R., Fallica, R., Yu, L., Altana, M., & Schift, H. J. A. M. T. (2017). Selective surface smoothening of polymer microlenses by depth confined softening. *2*(5), 1700018.
- Dannemann, K. A., Anderson Jr, C. E., Chocron, S., & Spencer, J. F. J. J. o. t. A. C. S. (2012). Damage development in confined borosilicate and soda-lime glasses. *95*(2), 721-729.
- Darraud-Taupiac, C., Bennamane, B., Decossas, J., Vareille, J. J. N. I., Materials, M. i. P. R. S. B. B. I. w., & Atoms. (1997). CR-39 (poly (diethylene glycol bis (allyl carbonate))) under γ-rays and proton beams. *131*(1-4), 198-204.
- Davis, K. M., Miura, K., Sugimoto, N., & Hirao, K. J. O. l. (1996). Writing waveguides in glass with a femtosecond laser. 21(21), 1729-1731.
- Day, D., & Gu, M. J. O. e. (2005). Microchannel fabrication in PMMA based on localized heating by nanojoule high repetition rate femtosecond pulses. *13*(16), 5939-5946.
- De Marco, C., Eaton, S. M., Suriano, R., Turri, S., Levi, M., Ramponi, R., . . . Osellame, R. (2010). Surface Properties of Femtosecond Laser Ablated PMMA. *ACS Applied Materials & Interfaces*, 2(8), 2377-2384. <a href="https://doi.org/10.1021/am100393e">https://doi.org/10.1021/am100393e</a>

- De Marco, C., Eaton, S. M., Suriano, R., Turri, S., Levi, M., Ramponi, R., . . . interfaces. (2010). Surface properties of femtosecond laser ablated PMMA. 2(8), 2377-2384.
- De Michele, V., Royon, M., Marin, E., Alessi, A., Morana, A., Boukenter, A., . . . Ouerdane, Y. J. O. M. E. (2019). Near-IR-and UV-femtosecond laser waveguide inscription in silica glasses. *9*(12), 4624-4633.
- Dharmadhikari, J., Dharmadhikari, A., Bhatnagar, A., Mallik, A., Singh, P. C., Dhaman, R. K., . . . Mathur, D. J. O. c. (2011). Writing low-loss waveguides in borosilicate (BK7) glass with a low-repetition-rate femtosecond laser. *284*(2), 630-634.
- Dias, A., Muñoz, F., Alvarez, A., Moreno-Zárate, P., Atienzar, J., Urbieta, A., . . . Solis, J. J. O. L. (2018). Femtosecond laser writing of photonic devices in borate glasses compositionally designed to be laser writable. *43*(11), 2523-2526.
- DiStefano, T., & Eastman, D. J. P. R. L. (1971). Photoemission Measurements of the Valence Levels of Amorphous Si O 2. 27(23), 1560.
- Dreischuh, T., Ajami, A., Taskova, E., Rafique, M. S., Pucher, N., Borisova, E., . . . Lüftenegger, S. (2008). *Z-scan measurements of two-photon absorption for ultrashort laser radiation* 15th International School on Quantum Electronics: Laser Physics and Applications,
- Dyakonov, I., Kalinkin, A., Saygin, M. Y., Abroskin, A., Radchenko, I., Straupe, S., & Kulik, S. J. A. P. B. (2016). Low-loss single-mode integrated waveguides in soda-lime glass. *122*(9), 1-7.
- Eaton, S. M., Ng, M. L., Bonse, J., Mermillod-Blondin, A., Zhang, H., Rosenfeld, A., & Herman, P. R. J. A. o. (2008). Low-loss waveguides fabricated in BK7 glass by high repetition rate femtosecond fiber laser. 47(12), 2098-2102.
- Eaton, S. M., Ng, M. L., Osellame, R., & Herman, P. R. (2011). High refractive index contrast in fused silica waveguides by tightly focused, high-repetition rate femtosecond laser. *Journal of Non-Crystalline Solids*, 357(11-13), 2387-2391. <a href="https://doi.org/10.1016/j.jnoncrysol.2010.11.082">https://doi.org/10.1016/j.jnoncrysol.2010.11.082</a>
- Eaton, S. M., Ng, M. L., Osellame, R., & Herman, P. R. J. J. o. N.-C. S. (2011). High refractive index contrast in fused silica waveguides by tightly focused, high-repetition rate femtosecond laser. *357*(11-13), 2387-2391.
- Eaton, S. M., Zhang, H., Herman, P. R., Yoshino, F., Shah, L., Bovatsek, J., & Arai, A. Y. J. O. e. (2005). Heat accumulation effects in femtosecond laser-written waveguides with variable repetition rate. *13*(12), 4708-4716.
- Eaton, S. M., Zhang, H., Ng, M. L., Li, J., Chen, W.-J., Ho, S., & Herman, P. R. J. O. e. (2008). Transition from thermal diffusion to heat accumulation in high repetition rate femtosecond laser writing of buried optical waveguides. *16*(13), 9443-9458.

- Ehrt, D., Kittel, T., Will, M., Nolte, S., & Tünnermann, A. J. J. o. n.-c. s. (2004). Femtosecond-laser-writing in various glasses. *345*, 332-337.
- El Ghazaly, M., & Hassan, H. E. (2014). Spectroscopic studies on alpha particle-irradiated PADC (CR-39 detector). *Results in Physics*, *4*, 40-43. <a href="https://doi.org/10.1016/j.rinp.2014.04.001">https://doi.org/10.1016/j.rinp.2014.04.001</a>
- Erfantalab, S., Parish, G., Keating, A. J. I. J. o. H., & Transfer, M. (2022). Determination of thermal conductivity, thermal diffusivity and specific heat capacity of porous silicon thin films using the 3ω method. *184*, 122346.
- Esinesco, D., Psoma, S., Kusco, M., Schneider, A., & Muller, R. (2005). SU-8 microbiosensor based on Mach-Zehnder interferometer. *J Reviews on Advanced Materials Science*, 10(4), 295-299.
- Faraji Rad, Z., Prewett, P. D., Davies, G. J. J. M., & Nanoengineering. (2021). High-resolution two-photon polymerization: The most versatile technique for the fabrication of microneedle arrays. 7(1), 71.
- Fatkullin, N., Ikehara, T., Jinnai, H., Kawata, S., Kimmich, R., Nishi, T., . . . Kawata, S. J. N. D. A. P. (2004). Two-photon photopolymerization and 3D lithographic microfabrication. 169-273.
- Fischer, J., Wegener, M. J. L., & Reviews, P. (2013). Three-dimensional optical laser lithography beyond the diffraction limit. 7(1), 22-44.
- Fletcher, L. B., Witcher, J. J., Troy, N., Reis, S. T., Brow, R. K., Vazquez, R. M., . . . Krol, D. M. J. O. M. E. (2011). Femtosecond laser writing of waveguides in zinc phosphate glasses. *I*(5), 845-855.
- Freund, I. J. A. P. L. (1968). SELF-Q-SWITCHING IN RUBY LASERS. *12*(11), 388-390.
- Gallais, L., Douti, D.-B., Commandre, M., Batavičiūtė, G., Pupka, E., Ščiuka, M., . . . Melninkaitis, A. J. J. o. A. P. (2015). Wavelength dependence of femtosecond laser-induced damage threshold of optical materials. *117*(22).
- Gamaly, E. G., Rode, A. V., & Luther-Davies, B. (2006). Ultrafast Laser Ablation and Film Deposition. In *Pulsed Laser Deposition of Thin Films* (pp. 99-129). <a href="https://doi.org/10.1002/9780470052129.ch5">https://doi.org/10.1002/9780470052129.ch5</a>
- Gamaly, E. G., Rode, A. V., Luther-Davies, B., & Tikhonchuk, V. T. (2002). Ablation of solids by femtosecond lasers: Ablation mechanism and ablation thresholds for metals and dielectrics. *Physics of Plasmas*, *9*(3), 949-957. <a href="https://doi.org/10.1063/1.1447555">https://doi.org/10.1063/1.1447555</a>
- Gao, H., Chen, G. F., Xing, P., Choi, J. W., Low, H. Y., & Tan, D. T. J. A. O. M. (2020). High-resolution 3D printed photonic waveguide devices. 8(18), 2000613.

- Garcia, C., Lang, W., Schomacker, A., Klarholz, I., & Harms, C. (2009). B3. 3-Fabrication of Microfluidic Devices Using SU-8 for Detection and Analysis of Viruses. *J Proceedings SENSOR*, *Volume I*, 193-197.
- Gašo, P., Pudiš, D., Seyringer, D., Kuzma, A., Gajdošová, L., Mizera, T., & Goraus, M. J. J. o. L. T. (2020). 3D polymer based 1x4 beam splitter. 39(1), 154-161.
- Gehring, H., Blaicher, M., Hartmann, W., Varytis, P., Busch, K., Wegener, M., & Pernice, W. (2019). Low-loss fiber-to-chip couplers with ultrawide optical bandwidth. *J APL Photonics*, 4(1), 010801.
- Goldman, L., Blaney, D. J., Kindel, D., & Franke, E. K. J. J. I. D. (1963). Effect of the laser beam on the skin. 40(121), 2.
- Goldman, L., Blaney, D. J., Kindel, D. J., Richfield, D., & Franke, E. K. J. N. (1963). Pathology of the effect of the laser beam on the skin. *197*(4870), 912-914.
- Goldman, L., & Rockwell, R. J. J. (1966). Laser action at the cellular level. *198*(6), 641-644.
- Göppert-Mayer, M. J. A. d. P. (1931). Über elementarakte mit zwei quantensprüngen. 401(3), 273-294.
- Goraus, M., Pudis, D., Urbancova, P., Martincek, I., & Gaso, P. J. A. S. S. (2018). Surface-relief Bragg grating waveguides based on IP-Dip polymer for photonic applications. *461*, 113-116.
- Grabulosa, A., Moughames, J., Porte, X., Kadic, M., & Brunner, D. J. N. (2023). Additive 3D photonic integration that is CMOS compatible. *34*(32), 322002.
- Groh, G. J. J. o. A. P. (1968). Vacuum deposition of thin films by means of a CO2 laser. 39(12), 5804-5805.
- Grojo, D., Leyder, S., Delaporte, P., Marine, W., Sentis, M., & Utéza, O. J. P. R. B. (2013). Long-wavelength multiphoton ionization inside band-gap solids. 88(19), 195135.
- Gross, S., & Withford, M. J. N. (2015). Ultrafast-laser-inscribed 3D integrated photonics: challenges and emerging applications. *4*(3), 332-352.
- Guan, J., Liu, X., Salter, P. S., & Booth, M. J. J. O. e. (2017). Hybrid laser written waveguides in fused silica for low loss and polarization independence. *25*(5), 4845-4859.
- Hamid, H. H., Fickenscher, T., & Thiel, D. V. (2015). Experimental assessment of SU-8 optical waveguides buried in plastic substrate for optical interconnections. *J Applied optics*, 54(22), 6623-6631.

- Harilal, S., Diwakar, P., Polek, M., & Phillips, M. J. O. e. (2015). Morphological changes in ultrafast laser ablation plumes with varying spot size. *23*(12), 15608-15615.
- He, F., Ni, J., Zeng, B., Cheng, Y., & Sugioka, K. (2015). Spatiotemporal manipulation of ultrashort pulses for three-dimensional (3-D) laser processing in glass materials. In *Laser Surface Engineering* (pp. 383-404). Elsevier.
- Hernandez-Rueda, J., Clarijs, J., van Oosten, D., & Krol, D. M. J. A. P. L. (2017a). The influence of femtosecond laser wavelength on waveguide fabrication inside fused silica. *110*(16), 161109.
- Hernandez-Rueda, J., Clarijs, J., van Oosten, D., & Krol, D. M. J. A. P. L. (2017b). The influence of femtosecond laser wavelength on waveguide fabrication inside fused silica. *110*(16).
- Hnatovsky, C., Taylor, R., Simova, E., Bhardwaj, V., Rayner, D., & Corkum, P. J. J. o. a. p. (2005). High-resolution study of photoinduced modification in fused silica produced by a tightly focused femtosecond laser beam in the presence of aberrations. *98*(1), 013517.
- Houldcroft, P. T. (1967). Welding processes. CUP Archive.
- Hsieh, Y. K., Chen, S. C., Huang, W. L., Hsu, K. P., Gorday, K. A. V., Wang, T., & Wang, J. (2017). Direct Micromachining of Microfluidic Channels on Biodegradable Materials Using Laser Ablation. *Polymers (Basel)*, 9(7). <a href="https://doi.org/10.3390/polym9070242">https://doi.org/10.3390/polym9070242</a>
- Huang, H., Yang, L.-M., & Liu, J. (2011a). Femtosecond fiber laser direct writing of optical waveguide in glasses. Nanophotonics and Macrophotonics for Space Environments V,
- Huang, H., Yang, L.-M., & Liu, J. (2011b). Femtosecond fiber laser direct writing of optical waveguide in glasses. Nanophotonics and Macrophotonics for Space Environments V,
- Huang, L., Salter, P., Payne, F., & Booth, M. J. O. E. (2016). Aberration correction for direct laser written waveguides in a transverse geometry. 24(10), 10565-10574.
- Hughes, M., Yang, W., & Hewak, D. J. A. P. L. (2007). Fabrication and characterization of femtosecond laser written waveguides in chalcogenide glass. *90*(13), 131113.
- Huot, N., Stoian, R., Mermillod-Blondin, A., Mauclair, C., & Audouard, E. J. O. e. (2007). Analysis of the effects of spherical aberration on ultrafast laser-induced refractive index variation in glass. *15*(19), 12395-12408.
- Ihlemann, J. J. A. s. s. (1992). Excimer laser ablation of fused silica. 54, 193-200.

- Jamshidi-Ghaleh, K., Masalehdan, H. J. O., & electronics, q. (2009). Modeling of nonlinear responses in BK7 glass under irradiation of femtosecond laser pulses. *41*(1), 47-53.
- Jamshidi-Ghaleh, K., Namdar, A., & Mansour, N. J. L. p. (2005). Nonlinear optical properties of soda-lime glass at 800-nm femtosecond irradiation. *15*(12), 1714-1717.
- Jia, C.-L., Tang, W.-J., Liu, K., & Liao, Y. J. O. M. (2023). Transparent Ho, Yb: YAG crystal waveguide inscribed by direct femtosecond laser writing. *135*, 113314.
- Jia, T., Chen, H., Huang, M., Zhao, F., Li, X., Xu, S., . . . Wang, X. J. P. R. B. (2006). Ultraviolet-infrared femtosecond laser-induced damage in fused silica and CaF 2 crystals. 73(5), 054105.
- Jia, Y., Wang, S., & Chen, F. J. O.-E. A. (2020). Femtosecond laser direct writing of flexibly configured waveguide geometries in optical crystals: fabrication and application. *3*(10), 190042-190041-190042-190012.
- Jiang, L. J., Maruo, S., Osellame, R., Xiong, W., Campbell, J. H., & Lu, Y. F. J. M. B. (2016). Femtosecond laser direct writing in transparent materials based on nonlinear absorption. 41(12), 975-983.
- Jones, S. C., Braunlich, P., Casper, R. T., Shen, X.-A., & Kelly, P. J. O. E. (1989). Recent progress on laser-induced modifications and intrinsic bulk damage of wide-gap optical materials. 28(10), 1039-1068.
- Kamata, M., Obara, M., Gattass, R. R., Cerami, L. R., & Mazur, E. J. A. P. L. (2005). Optical vibration sensor fabricated by femtosecond laser micromachining. 87(5), 051106.
- Kanehira, S., Miura, K., & Hirao, K. J. A. P. L. (2008). Ion exchange in glass using femtosecond laser irradiation. *93*(2), 023112.
- Kappes, R. S., Schönfeld, F., Li, C., Golriz, A. A., Nagel, M., Lippert, T., . . . Gutmann, J. S. J. S. (2014). A study of photothermal laser ablation of various polymers on microsecond time scales. *3*, 1-15.
- Kautek, W., Krüger, J., Lenzner, M., Sartania, S., Spielmann, C., & Krausz, F. (1996). Laser ablation of dielectrics with pulse durations between 20 fs and 3 ps. *Applied Physics Letters*, 69(21), 3146-3148. <a href="https://doi.org/10.1063/1.116810">https://doi.org/10.1063/1.116810</a>
- Kedia, S., Deo, M., & Sinha, S. J. A. O. M. (2015). Micro-modification in borosilicate glass using femtosecond laser. *3*, 1-6.
- Keldysh, L. J. S. P. J. (1965). Ionization in the field of a strong electromagnetic wave. 20(5), 1307-1314.

- Kelemen, L., Lepera, E., Horváth, B., Ormos, P., Osellame, R., & Vázquez, R. M. J. L. o. a. C. (2019). Direct writing of optical microresonators in a lab-on-a-chip for label-free biosensing. *19*(11), 1985-1990.
- Kim, J., & Xu, X. J. J. o. L. A. (2003). Excimer laser fabrication of polymer microfluidic devices. *15*(4), 255-260.
- Kirchner, R., Chidambaram, N., Altana, M., & Schift, H. (2017). How post-processing by selective thermal reflow can reduce the roughness of 3D lithography in micro-optical lenses. Laser 3D Manufacturing IV,
- Kirchner, R., & Schift, H. J. M. S. i. S. P. (2019). Thermal reflow of polymers for innovative and smart 3D structures: A review. *92*, 58-72.
- Kostovski, G., Stoddart, P. R., & Mitchell, A. J. A. M. (2014). The optical fiber tip: an inherently light-coupled microscopic platform for micro-and nanotechnologies. *26*(23), 3798-3820.
- Kowalevicz, A., Sharma, V., Ippen, E., Fujimoto, J. G., & Minoshima, K. J. O. l. (2005). Three-dimensional photonic devices fabricated in glass by use of a femtosecond laser oscillator. *30*(9), 1060-1062.
- Krüger, J., & Kautek, W. J. L. p. (1999). The femtosecond pulse laser: a new tool for micromachining. (9, 1), 30-40.
- Krüger, J., Martin, S., Mädebach, H., Urech, L., Lippert, T., Wokaun, A., & Kautek, W. J. A. s. s. (2005). Femto-and nanosecond laser treatment of doped polymethylmethacrylate. *247*(1-4), 406-411.
- Kumagai, H., Midorikawa, K., Toyoda, K., Nakamura, S., Okamoto, T., & Obara, M. J. A. p. l. (1994). Ablation of polymer films by a femtosecond high-peak-power Ti: sapphire laser at 798 nm. *65*(14), 1850-1852.
- Küper, S., & Stuke, M. J. A. P. B. (1987). Femtosecond UV excimer laser ablation. 44, 199-204.
- Lafleur, S. S., Shen, L., Kamphuis, E. J., Houben, S. J., Balzano, L., Severn, J. R., . . . Bastiaansen, C. W. J. M. R. C. (2019). Optical Patterns on Drawn Polyethylene by Direct Laser Writing. 40(9), 1800811.
- Lancry, M., & Poumellec, B. (2006). Multiphoton absorption processes & UV laser processing of silica-based materials. Proceedings of the 1st International Workshop on Multiphoton Processes in Glass and Glassy Materials, J. Canning, Ed., Sydney, Australia,
- Landowski, A., Zepp, D., Wingerter, S., von Freymann, G., & Widera, A. J. A. P. (2017). Direct laser written polymer waveguides with out of plane couplers for optical chips. 2(10), 106102.

- Lei, Y., Wang, H., Skuja, L., Kühn, B., Franz, B., Svirko, Y., . . . Reviews, P. (2023). Ultrafast laser writing in different types of silica glass. 17(7), 2200978.
- Leith, E. N., & Upatnieks, J. J. (1962). Reconstructed wavefronts and communication theory. 52(10), 1123-1130.
- Lenzner, M., Krüger, J., Sartania, S., Cheng, Z., Spielmann, C., Mourou, G., . . . Krausz, F. J. P. r. l. (1998). Femtosecond optical breakdown in dielectrics. 80(18), 4076.
- Li, C., Liao, C., Wang, J., Li, Z., Wang, Y., He, J., . . . Wang, Y. J. O. L. (2018). Femtosecond laser microprinting of a polymer fiber Bragg grating for high-sensitivity temperature measurements. *43*(14), 3409-3412.
- Li, J., Cao, C., Qiu, Y., Kuang, C., & Liu, X. J. A. M. T. (2023). Optical waveguides fabricated via femtosecond direct laser writing: processes, materials, and devices. 8(18), 2300620.
- Li, L., Gattass, R. R., Gershgoren, E., Hwang, H., & Fourkas, J. T. J. S. (2009). Achieving  $\lambda/20$  resolution by one-color initiation and deactivation of polymerization. *324*(5929), 910-913.
- Li, L., Kong, W., & Chen, F. J. A. P. (2022). Femtosecond laser-inscribed optical waveguides in dielectric crystals: a concise review and recent advances. 4(2), 024002-024002.
- Lindenmann, N., Balthasar, G., Hillerkuss, D., Schmogrow, R., Jordan, M., Leuthold, J., . . . Koos, C. J. O. e. (2012). Photonic wire bonding: a novel concept for chipscale interconnects. *20*(16), 17667-17677.
- Lindenmann, N., Kaiser, I., Balthasar, G., Bonk, R., Hillerkuss, D., Freude, W., . . . Koos, C. (2011). Photonic waveguide bonds—a novel concept for chip-to-chip interconnects. National Fiber Optic Engineers Conference,
- Lipateva, T. O., Lipatiev, A. S., Karateev, I. V., Okhrimchuk, A. G., Fedotov, S. S., Lotarev, S. V., . . . Compounds. (2023). Direct laser writing in YAG single crystal: Evolution from amorphization to nanograting formation and phase transformation. *942*, 169081.
- Lipatiev, A. S., Lipateva, T. O., Lotarev, S. V., Okhrimchuk, A. G., Larkin, A. S., Presnyakov, M. Y., . . . Design. (2017). Direct laser writing of LaBGeO5 crystal-in-glass waveguide enabling frequency conversion. *17*(9), 4670-4675.
- Little, D. J., Ams, M., Dekker, P., Marshall, G. D., Dawes, J. M., & Withford, M. J. J. O. e. (2008). Femtosecond laser modification of fused silica: the effect of writing polarization on Si-O ring structure. *16*(24), 20029-20037.
- Liu, D., Li, Y., An, R., Dou, Y., Yang, H., & Gong, Q. J. A. P. A. (2006). Influence of focusing depth on the microfabrication of waveguides inside silica glass by femtosecond laser direct writing. *84*, 257-260.

- Liu, H., Cheng, C., Romero, C., de Aldana, J. R. V., & Chen, F. J. O. e. (2015). Graphene-based Y-branch laser in femtosecond laser written Nd: YAG waveguides. 23(8), 9730-9735.
- Liu, J., Zhang, Z., Flueraru, C., Liu, X., Chang, S., & Grover, C. P. J. I. J. o. s. t. i. q. e. (2004). Waveguide shaping and writing in fused silica using a femtosecond laser. *10*(1), 169-173.
- Liu, Q., Zhan, Y., Zhang, S., Feng, S., Wang, X., Sun, W., . . . Zhang, Y. J. O. E. (2020). "Optical tentacle" of suspended polymer micro-rings on a multicore fiber facet for vapor sensing. 28(8), 11730-11741.
- Liu, Y., Shimizu, M., Zhu, B., Dai, Y., Qian, B., Qiu, J., . . . Hirao, K. J. O. L. (2009). Micromodification of element distribution in glass using femtosecond laser irradiation. *34*(2), 136-138.
- Liu, Y., Zhu, B., Wang, L., Qiu, J., Dai, Y., & Ma, H. J. A. P. L. (2008). Femtosecond laser induced coordination transformation and migration of ions in sodium borate glasses. *92*(12), 121113.
- Lounis-Mokrani, Z., Fromm, M., Barillon, R., Chambaudet, A., & Allab, M. (2003). Characterization of chemical and optical modifications induced by proton beams in CR-39 detectors. *Radiation Measurements*, *36*(1-6), 615-620. <a href="https://doi.org/10.1016/s1350-4487(03)00211-7">https://doi.org/10.1016/s1350-4487(03)00211-7</a>
- Macias-Montero, M., Munoz, F., Sotillo, B., Del Hoyo, J., Ariza, R., Fernandez, P., . . . Solis, J. (2021). Femtosecond laser induced thermophoretic writing of waveguides in silicate glass. *Sci Rep*, *11*(1), 8390. https://doi.org/10.1038/s41598-021-87765-z
- Mainik, P., Spiegel, C. A., & Blasco, E. J. A. M. (2024). Recent advances in multiphoton 3D laser printing: active materials and applications. *36*(11), 2310100.
- Mansour, S., Wageh, S., Alotaibi, M. F., Abdo, M., & Sadeq, M. J. C. I. (2021). Impact of bismuth oxide on the structure, optical features and ligand field parameters of borosilicate glasses doped with nickel oxide. *47*(15), 21443-21449.
- Marcinkevičius, A., Mizeikis, V., Juodkazis, S., Matsuo, S., & Misawa, H. J. A. P. A. (2003). Effect of refractive index-mismatch on laser microfabrication in silica glass. *76*, 257-260.
- Marcuse, D. J. B. s. t. j. (1977). Loss analysis of single-mode fiber splices. 56(5), 703-718.
- Marinins, A., Knudde, N., & Popov, S. J. I. P. T. L. (2016). Air-suspended SU-8 strip waveguides with high refractive index contrast. 28(17), 1862-1865.
- Marshall, G. D., Ams, M., & Withford, M. J. J. O. L. (2006). Direct laser written waveguide-Bragg gratings in bulk fused silica. *31*(18), 2690-2691.

- Maruo, S., & Fourkas, J. T. (2008). Recent progress in multiphoton microfabrication. *J Laser Photonics Reviews*, 2(1-2), 100-111.
- Maruo, S., Fourkas, J. T. J. L., & Reviews, P. (2008). Recent progress in multiphoton microfabrication. 2(1-2), 100-111.
- Mary, K. A., Unnikrishnan, N., & Philip, R. J. R. A. (2015). Cubic to amorphous transformation of Se in silica with improved ultrafast optical nonlinearity. *5*(18), 14034-14041.
- McMillen, B., Zhang, B., Chen, K. P., Benayas, A., & Jaque, D. J. O. l. (2012). Ultrafast laser fabrication of low-loss waveguides in chalcogenide glass with 0.65 dB/cm loss. *37*(9), 1418-1420.
- Migal, E., Mareev, E., Smetanina, E., Duchateau, G., & Potemkin, F. (2019). Role of deposited energy density and impact ionization in the process of femtosecond laser-matter interaction in solids: Scaling from visible to mid-IR wavelength. Nonlinear Optics and Applications XI,
- Minoshima, K., Kowalevicz, A. M., Hartl, I., Ippen, E. P., & Fujimoto, J. G. J. O. L. (2001). Photonic device fabrication in glass by use of nonlinear materials processing with a femtosecond laser oscillator. *26*(19), 1516-1518.
- Mittholiya, K., Anshad, P., Mallik, A., Bhardwaj, S., Hegde, A., Bhatnagar, A., . . . Dharmadhikari, A. J. J. o. O. (2017). Inscription of waveguides and power splitters in borosilicate glass using ultrashort laser pulses. *46*(3), 304-310.
- Miyamoto, I., Cvecek, K., & Schmidt, M. J. O. E. (2011). Evaluation of nonlinear absorptivity in internal modification of bulk glass by ultrashort laser pulses. *19*(11), 10714-10727.
- Mocker, H. W., & Collins, R. J. J. A. P. L. (1965). Mode competition and self-locking effects in aq-switched ruby laser. 7(10), 270-273.
- Moghaddam, S. A., & Jamshidi, G. K. (2010). Nonlinear optical response and optical properties modification in crown B270 glass sample with fs laser pulses.
- Mohammed, K., Azawe, M. J. N. I., Materials, M. i. P. R. S. B. B. I. w., & Atoms. (2013). Measurement of thermal and optical properties of CR-39 solid-state nuclear detector by photothermal deflection. *308*, 54-61.
- Mueller, P., Thiel, M., & Wegener, M. J. O. l. (2014). 3D direct laser writing using a 405 nm diode laser. 39(24), 6847-6850.
- Müller, J. B. J. K. I. o. T. (2015). Exploring the mechanisms of 3D direct laser writing by multi-photon polymerization.

- Mulvaney, W. P., & Beck, C. W. J. T. J. o. u. (1968). The laser beam in urology. 99(1), 112-115.
- Nasu, Y., Kohtoku, M., & Hibino, Y. J. O. l. (2005). Low-loss waveguides written with a femtosecond laser for flexible interconnection in a planar light-wave circuit. 30(7), 723-725.
- Nesic, A., Blaicher, M., Hoose, T., Hofmann, A., Lauermann, M., Kutuvantavida, Y., . . . Koos, C. J. O. E. (2019). Photonic-integrated circuits with non-planar topologies realized by 3D-printed waveguide overpasses. *27*(12), 17402-17425.
- Ng, K., Chong, W., Lim, C., & Ahmad, H. J. O. (2022). Single-mode SU-8 waveguide fabricated using ultrafast direct laser writing. *270*, 170068.
- Nguyen, D. T. T., Tong, Q. C., Ledoux-Rak, I., & Lai, N. D. J. J. o. A. P. (2016). One-step fabrication of submicrostructures by low one-photon absorption direct laser writing technique with local thermal effect. *119*(1), 013101.
- Nguyen, M.-H., Chang, C.-J., Lee, M.-C., & Tseng, F.-G. J. O. E. (2011). SU8 3D prisms with ultra small inclined angle for low-insertion-loss fiber/waveguide interconnection. *19*(20), 18956-18964.
- Nidhi, Gupta, R., Sharma, T., Aggarwal, S., & Kumar, S. (2009). Effect of thermal annealing on optical properties of CR-39 polymeric track detector. *Indian Journal of Physics*, 83(7), 921-926. https://doi.org/10.1007/s12648-009-0049-4
- Nolte, S., Szameit, A., & Tünnermann, A. (2009). Femtosecond laser direct writing of waveguide lattices. Conference on Lasers and Electro-Optics,
- Ohdaira, K., Fujiwara, T., Endo, Y., Nishizaki, S., & Matsumura, H. J. J. j. o. a. p. (2008). Formation of several-micrometer-thick polycrystalline silicon films on soda lime glass by flash lamp annealing. *47*(11R), 8239.
- Ohlinger, K., Lin, Y., Poole, Z., & Chen, K. P. (2011). Undistorted 3D microstructures in SU8 formed through two-photon polymerization. *J AIP Advances*, 1(3), 032163.
- Okhrimchuk, A., Mezentsev, V., Schmitz, H., Dubov, M., & Bennion, I. J. L. p. (2009). Cascaded nonlinear absorption of femtosecond laser pulses in dielectrics. *19*, 1415-1422.
- Okhrimchuk, A., Shestakov, A., Khrushchev, I., & Mitchell, J. J. O. l. (2005). Depressed cladding, buried waveguide laser formed in a YAG: Nd 3+ crystal by femtosecond laser writing. *30*(17), 2248-2250.
- Parthenopoulos, D. A., & Rentzepis, P. M. J. S. (1989). Three-dimensional optical storage memory. *245*(4920), 843-845.

- Patel, C. J. S. A. (1968). High-power carbon dioxide lasers. 219(2), 22-33.
- Pereira, A., Delaporte, P., Sentis, M., Marine, W., Thomann, A. L., & Boulmer-Leborgne, C. J. J. o. a. p. (2005). Optical and morphological investigation of backward-deposited layer induced by laser ablation of steel in ambient air. 98(6).
- Pillai, M. M., Ajesh, S., & Tayalia, P. J. M. (2023). Two-photon polymerization based reusable master template to fabricate polymer microneedles for drug delivery. *10*, 102025.
- Piruska, A., Bhagat, A., Zhou, K., Peterson, E., Papautsky, I., & Seliskar, C. (2006). Characterization of SU-8 optical multimode waveguides for integrated optics and sensing on microchip devices. Microfluidics, BioMEMS, and Medical Microsystems IV,
- Prokop, C., Kleeßen, P., Irmler, N., Mitchell, A., & Karnutsch, C. (2015). Airsuspended polymer rib waveguides. Integrated Optics: Devices, Materials, and Technologies XIX,
- Prokop, C., Schoenhardt, S., Laegel, B., Wolff, S., Mitchell, A., & Karnutsch, C. J. J. o. L. T. (2016). Air-suspended SU-8 polymer waveguide grating couplers. *34*(17), 3966-3971.
- Psaila, N., Thomson, R., Bookey, H., Kar, A., Chiodo, N., Osellame, R., . . . Shen, S. J. O. E. (2006). Femtosecond laser inscription of optical waveguides in Bismuth ion doped glass. *14*(22), 10452-10459.
- Rafique, M. S., Bashir, S., Ajami, A., & Husinsky, W. (2010). Nonlinear absorption properties correlated with the surface and structural changes of ultra short pulse laser irradiated CR-39. *Applied Physics A*, 100(4), 1183-1189. https://doi.org/10.1007/s00339-010-5741-x
- Ramirez, J. C., Schianti, J. N., Almeida, M. G., Pavani, A., Panepucci, R. R., Hernandez-Figueroa, H. E., & Gabrielli, L. H. (2017). Low-loss modified SU-8 waveguides by direct laser writing at 405 nm. *Optical Materials Express*, 7(7). <a href="https://doi.org/10.1364/ome.7.002651">https://doi.org/10.1364/ome.7.002651</a>
- Ravi-Kumar, S., Lies, B., Lyu, H., & Qin, H. (2019). Laser Ablation of Polymers: A Review. *Procedia Manufacturing*, *34*, 316-327. https://doi.org/10.1016/j.promfg.2019.06.155
- Sagheer, R., Rafique, M. S., Saleemi, F., Arif, S., Naab, F., Toader, O., . . . Hussain, I. (2016). Modification in surface properties of poly-allyl-diglycol-carbonate (CR-39) implanted by Au+ ions at different fluences. *Materials Science-Poland*, 34(2), 468-478. <a href="https://doi.org/10.1515/msp-2016-0067">https://doi.org/10.1515/msp-2016-0067</a>

- Sakakura, M., Kurita, T., Yoshimura, K., Fukuda, N., Shimotsuma, Y., & Miura, K. J. A. P. B. (2015). Control of Si-rich region inside a sodalime glass by parallel femtosecond laser focusing at multiple spots. *119*, 485-492.
- Sakellari, I., Kabouraki, E., Gray, D., Purlys, V., Fotakis, C., Pikulin, A., . . . Farsari, M. J. A. n. (2012). Diffusion-assisted high-resolution direct femtosecond laser writing. *6*(3), 2302-2311.
- Sarker, S., Colton, A., Wen, Z., Xu, X., Erdi, M., Jones, A., . . . Janowski, M. J. A. m. t. (2023). 3D-Printed Microinjection Needle Arrays via a Hybrid DLP-Direct Laser Writing Strategy. 8(5), 2201641.
- Schaffer, C. B., Brodeur, A., García, J. F., & Mazur, E. J. O. l. (2001). Micromachining bulk glass by use of femtosecond laser pulses with nanojoule energy. *26*(2), 93-95.
- Schaffer, C. B., Brodeur, A., Mazur, E. J. M. S., & Technology. (2001). Laser-induced breakdown and damage in bulk transparent materials induced by tightly focused femtosecond laser pulses. *12*(11), 1784.
- Schröder, M., Bülters, M., Von Kopylow, C., & Bergmann, R. J. J. o. t. E. O. S.-R. p. (2012). Novel concept for three-dimensional polymer waveguides for optical onchip interconnects. 7.
- Schumann, M., Bückmann, T., Gruhler, N., Wegener, M., & Pernice, W. (2014a). Hybrid 2D–3D optical devices for integrated optics by direct laser writing. *Light: Science & Applications*, *3*(6), e175-e175. https://doi.org/10.1038/lsa.2014.56
- Schumann, M., Bückmann, T., Gruhler, N., Wegener, M., & Pernice, W. (2014b). Hybrid 2D–3D optical devices for integrated optics by direct laser writing. *J Light: Science Applications*
- 3(6), e175-e175.
- Schumann, M., Bückmann, T., Gruhler, N., Wegener, M., Pernice, W. J. L. S., & Applications. (2014). Hybrid 2D–3D optical devices for integrated optics by direct laser writing. *3*(6), e175-e175.
- Selimis, A., Mironov, V., & Farsari, M. J. M. E. (2015). Direct laser writing: Principles and materials for scaffold 3D printing. *132*, 83-89.
- Shah, L., Arai, A. Y., Eaton, S. M., & Herman, P. R. J. O. e. (2005). Waveguide writing in fused silica with a femtosecond fiber laser at 522 nm and 1 MHz repetition rate. *13*(6), 1999-2006.
- Shehata, A., Ali, M., Schuch, R., Mohamed, T. J. O., & Technology, L. (2019). Experimental investigations of nonlinear optical properties of soda-lime glasses and theoretical study of self-compression of fs laser pulses. *116*, 276-283.

- Shekhawat, N., Aggarwal, S., Sharma, A., Sharma, S. K., Deshpande, S. K., & Nair, K. G. M. (2011). Surface disordering and its correlations with properties in argon implanted CR-39 polymer. *Journal of Applied Physics*, *109*(8). <a href="https://doi.org/10.1063/1.3573480">https://doi.org/10.1063/1.3573480</a>
- Shimotsuma, Y., Kazansky, P. G., Qiu, J., & Hirao, K. J. P. r. l. (2003). Self-organized nanogratings in glass irradiated by ultrashort light pulses. *91*(24), 247405.
- Simanovskii, D., Schwettman, H., Lee, H., & Welch, A. J. P. r. l. (2003). Midinfrared optical breakdown in transparent dielectrics. *91*(10), 107601.
- Smith, W. (1981). Absolute two-photon absorption coefficient at 355 nm in UV glasses. Conference on Lasers and Electro-Optics,
- Smolík, J., Knotek, P., Schwarz, J., Černošková, E., Janíček, P., Melánová, K., . . . Staněk, J. J. A. S. S. (2022). 3D micro-structuring by CW direct laser writing on PbO-Bi2O3-Ga2O3 glass. 589, 152993.
- Song, D., Husari, A., Kotz-Helmer, F., Tomakidi, P., Rapp, B. E., & Rühe, J. J. S. (2024). Two-Photon Direct Laser Writing of 3D Scaffolds through C, H-Insertion Crosslinking in a One-Component Material System. *20*(17), 2306682.
- Spectra-Physics. (2002). Mode-Locked Ti:Sapphire Laser User's Manual.
- Stuart, B., Feit, M., Herman, S., Rubenchik, A., Shore, B., & Perry, M. J. P. r. B. (1996). Nanosecond-to-femtosecond laser-induced breakdown in dielectrics. *53*(4), 1749.
- Stuart, B., Feit, M., Rubenchik, A., Shore, B., & Perry, M. J. P. r. l. (1995). Laser-induced damage in dielectrics with nanosecond to subpicosecond pulses. 74(12), 2248.
- Sudrie, L., Couairon, A., Franco, M., Lamouroux, B., Prade, B., Tzortzakis, S., & Mysyrowicz, A. J. P. R. L. (2002). Femtosecond laser-induced damage and filamentary propagation in fused silica. 89(18), 186601.
- Sugioka, K., Xu, J., Wu, D., Hanada, Y., Wang, Z., Cheng, Y., & Midorikawa, K. J. L. o. a. C. (2014). Femtosecond laser 3D micromachining: a powerful tool for the fabrication of microfluidic, optofluidic, and electrofluidic devices based on glass. *14*(18), 3447-3458.
- Sun, H.-B., & Kawata, S. J. J. o. l. t. (2003). Two-photon laser precision microfabrication and its applications to micro-nano devices and systems. 21(3), 624.
- Sun, Q., Jiang, H., Liu, Y., Zhou, Y., Yang, H., Gong, Q. J. J. o. O. A. P., & Optics, A. (2005). Effect of spherical aberration on the propagation of a tightly focused femtosecond laser pulse inside fused silica. 7(11), 655.

- Suriano, R., Kuznetsov, A., Eaton, S. M., Kiyan, R., Cerullo, G., Osellame, R., . . . Turri, S. (2011). Femtosecond laser ablation of polymeric substrates for the fabrication of microfluidic channels. *Applied Surface Science*, 257(14), 6243-6250. <a href="https://doi.org/10.1016/j.apsusc.2011.02.053">https://doi.org/10.1016/j.apsusc.2011.02.053</a>
- Tan, D., Sharafudeen, K. N., Yue, Y., & Qiu, J. J. P. i. M. S. (2016). Femtosecond laser induced phenomena in transparent solid materials: Fundamentals and applications. *76*, 154-228.
- Tan, D., Wang, Z., Xu, B., & Qiu, J. J. A. P. (2021). Photonic circuits written by femtosecond laser in glass: improved fabrication and recent progress in photonic devices. 3(2), 024002-024002.
- Teh, K. S. J. F. o. M. E. (2017). Additive direct-write microfabrication for MEMS: A review. 12, 490-509.
- Teh, W., Dürig, U., Salis, G., Harbers, R., Drechsler, U., Mahrt, R., . . . Güntherodt, H.-J. (2004). SU-8 for real three-dimensional subdiffraction-limit two-photon microfabrication. *J Applied Physics Letters*, 84(20), 4095-4097.
- Thiel, M., Fischer, J., Von Freymann, G., & Wegener, M. J. A. P. L. (2010). Direct laser writing of three-dimensional submicron structures using a continuous-wave laser at 532 nm. 97(22), 221102.
- Thomson, R. R., Psaila, N. D., Beecher, S. J., & Kar, A. K. J. O. e. (2010). Ultrafast laser inscription of a high-gain Er-doped bismuthate glass waveguide amplifier. *18*(12), 13212-13219.
- Tong, L., Gattass, R. R., Maxwell, I., Ashcom, J. B., & Mazur, E. J. O. c. (2006). Optical loss measurements in femtosecond laser written waveguides in glass. 259(2), 626-630.
- Tong, Q. C., Nguyen, D. T. T., Do, M. T., Luong, M. H., Journet, B., Ledoux-Rak, I., & Lai, N. D. J. A. P. L. (2016). Direct laser writing of polymeric nanostructures via optically induced local thermal effect. *108*(18), 183104.
- Trautmann, A., Roth, G.-L., Nujiqi, B., Walther, T., Hellmann, R. J. M., & Nanoengineering. (2019). Towards a versatile point-of-care system combining femtosecond laser generated microfluidic channels and direct laser written microneedle arrays. 5(1), 6.
- Traynor, N. B. J., McLauchlin, C., Dodge, K., McGarrah, J. E., Padalino, S. J., McCluskey, M., . . . McLean, J. G. (2018). CR-39 (PADC) Reflection and Transmission of Light in the Ultraviolet-Near-Infrared (UV-NIR) Range. *Appl Spectrosc*, 72(4), 591-597. https://doi.org/10.1177/0003702817745071
- Tsutsumi, N., Hirota, J., Kinashi, K., & Sakai, W. (2017). Direct laser writing for micro-optical devices using a negative photoresist. *J Optics express*, 25(25), 31539-31551.

- Tsutsumi, N., Sakamoto, N., Nakamura, R., Kinashi, K., & Sakai, W. (2017). Influence of baking conditions on 3D microstructures by direct laser writing in negative photoresist SU-8 via two-photon polymerization. *J Journal of Laser Applications*, 29(4), 042010.
- Turner, M. D., Schröder-Turk, G. E., Gu, M. J. L. T. i. B. B., & Applications. (2014). Biomimetic photonic materials by direct laser writing. 67-82.
- Wang, H., Zhang, W., Ladika, D., Yu, H., Gailevičius, D., Wang, H., . . . Mori, T. J. A. F. M. (2023). Two-photon polymerization lithography for optics and photonics: fundamentals, materials, technologies, and applications. *33*(39), 2214211.
- Wang, Z., Hong, M., Lu, Y., Wu, D., Lan, B., & Chong, T. J. J. o. a. p. (2003). Femtosecond laser ablation of polytetrafluoroethylene (Teflon) in ambient air. 93(10), 6375-6380.
- White, G. J. J. o. P. D. A. P. (1973). Thermal expansion of reference materials: copper, silica and silicon. 6(17), 2070.
- White, W., Henesian, M., & Weber, M. J. J. B. (1985). Photothermal-lensing measurements of two-photon absorption and two-photon-induced color centers in borosilicate glasses at 532 nm. 2(9), 1402-1408.
- Will, M., Nolte, S., Chichkov, B. N., & Tünnermann, A. J. A. O. (2002). Optical properties of waveguides fabricated in fused silica by femtosecond laser pulses. *41*(21), 4360-4364.
- Williams, H. E., Luo, Z., & Kuebler, S. M. J. O. e. (2012). Effect of refractive index mismatch on multi-photon direct laser writing. *20*(22), 25030-25040.
- Wlodarczyk, K. L., Carter, R. M., Jahanbakhsh, A., Lopes, A. A., Mackenzie, M. D., Maier, R. R. J., . . . Maroto-Valer, M. M. (2018). Rapid Laser Manufacturing of Microfluidic Devices from Glass Substrates. *Micromachines (Basel)*, 9(8). <a href="https://doi.org/10.3390/mi9080409">https://doi.org/10.3390/mi9080409</a>
- Wu, B., Zhang, B., Liu, W., Lu, Q., Wang, L., Chen, F. J. O., & Technology, L. (2022). Recoverable and rewritable waveguide beam splitters fabricated by tailored femtosecond laser writing of lithium tantalate crystal. *145*, 107500.
- Wu, J., Zhang, Y., Li, L., Ren, Y., Lu, Q., Wang, L., & Chen, F. J. R. i. P. (2021). Raman spectra study on modifications of BK7 glass induced by 1030-nm and 515-nm femtosecond laser. *21*, 103814.
- Wu, Z., Liang, Y., Li, C., Han, X., Gu, Y., Hu, J., & Zhao, M. (2016). Design and fabrication of polymer-based 1× 4 Y-branch splitters. *J Optik*, 127(23), 11427-11432.

- Xiong, Y., Wang, S., Chen, Z., Sun, X., Liu, H., Jia, Y., . . . Technology, L. (2023). Femtosecond laser direct writing of compact Tm: YLF waveguide lasers. *167*, 109786.
- Xu, X., Ma, L., & He, Z. (2018a). 3D polymer directional coupler for on-board optical interconnects at 1550 nm. *J Optics express*, 26(13), 16344-16351.
- Xu, X., Ma, L., & He, Z. J. O. E. (2018b). 3D polymer directional coupler for on-board optical interconnects at 1550 nm. 26(13), 16344-16351.
- Yadav, A. K., Gautam, C., Gautam, A., & Mishra, V. K. J. P. T. (2013). Structural and crystallization behavior of (Ba, Sr) TiO3 borosilicate glasses. 86(10), 1000-1016.
- Yang, L., Yang, B., Sheng, Z., Wang, J., Dai, D., & He, S. (2008). Compact 2× 2 tapered multimode interference couplers based on SU-8 polymer rectangular waveguides. *J Applied Physics Letters*, 93(20), 418.
- Yang, T., Lin, H., & Jia, B. J. C. O. L. (2020). Ultrafast direct laser writing of 2D materials for multifunctional photonics devices. *18*(2), 023601.
- Yu, H., Zhang, Q., Chen, X., Luan, H., & Gu, M. J. A. P. (2022). Three-dimensional direct laser writing of biomimetic neuron interfaces in the era of artificial intelligence: principles, materials, and applications. *4*(3), 034002-034002.
- Yules, R. B., Laub, D. R., Honey, R., Vassiliadis, A., & Crowley, L. J. A. o. S. (1967). The effect of Q-switched ruby laser radiation on dermal tattoo pigment in man. 95(2), 179-180.
- Zaki, M. F., Ghaly, W. A., & El-Bahkiry, H. S. (2015). Photoluminescence, optical band gap and surface wettability of some polymeric track detectors modified by electron beam. *Surface and Coatings Technology*, 275, 363-368. <a href="https://doi.org/10.1016/j.surfcoat.2015.04.041">https://doi.org/10.1016/j.surfcoat.2015.04.041</a>
- Zhang, B., Wang, L., Chen, F. J. L., & Reviews, P. (2020). Recent advances in femtosecond laser processing of LiNbO3 crystals for photonic applications. *14*(8), 1900407.
- Zhang, H., Eaton, S. M., Li, J., & Herman, P. R. J. O. l. (2006). Femtosecond laser direct writing of multiwavelength Bragg grating waveguides in glass. *31*(23), 3495-3497.
- Zheltikov, A. J. P. R. A. (2016). Keldysh parameter, photoionization adiabaticity, and the tunneling time. *94*(4), 043412.
- Zhou, X., Hou, Y., & Lin, J. J. A. A. (2015). A review on the processing accuracy of two-photon polymerization. *5*(3), 030701.